GRACE-based investigation of large-scale land-atmosphere interactions

By

Ajiao Chen

Thesis
Submitted to Flinders University
for the degree of

Doctor of Philosophy

National Centre for Groundwater Research and Training, College of Science and Engineering, Flinders University, Adelaide, South Australia

January 2022

TABLE OF CONTENTS

ABSTRACT

Land-atmosphere interactions encompass complex surface processes that exchange energy and matter between land and the atmosphere, which play important roles in modulating variations in climate. Prediction on future climate change calls for more precise prediction models. Improving the representation of physical processes of land-atmosphere interactions and the availability of key variables for characterizing those processes could help reduce uncertainties in the prediction models, and consequently make contribution to extreme weather forecasting and natural disasters prevention.

Terrestrial water storage (TWS, includes surface water, soil moisture, groundwater, snow, and ice) constitutes a significant memory component within the climate system. However, in Australia, the driest inhabitant continent, there is still a lack of investigation on the long-term TWS variation pattern. In addition, soil moisture as the most variable component of TWS has strong interactions with vegetation and near-surface temperature, but investigations on those interactions have been impeded by the scarcity of soil moisture observations.

The long-term wetting/drying pattern in Australia was investigated in this thesis by applying the Gravity Recovery and Climate Experiment (GRACE) satellite derived TWS anomaly and extended datasets. A seesaw pattern of TWS variation between eastern and western Australia was revealed: eastern Australia gaining water, while western Australia is losing water, and vice versa. This phenomenon is resulted from a combination of effects from large-scale climate mode and dynamic vegetation and soil moisture interactions. It highlighted the bidirectional effects between surface vegetation and land water conditions, but such knowledge of Australia remained poorly understood. Results of this thesis for the first time indicated that non-linear interactions between vegetation and TWS occurred in 58% of the area of Australia. Those new findings partly improved our understanding of physical processes in Australia's land-atmosphere interactions.

On the other hand, this thesis proposes the first use of wavelet decomposed GRACE TWS as a proxy of soil moisture to investigate its relationship with air temperature anomaly/hot extremes at the global scale. Compared to raw TWS, decomposed TWS showed improved skill in explaining temperature variability. It is because that the decomposed components could reflect different roles of moisture at different soil depths in the soil moisture-temperature coupling. The wavelet decomposed TWS also performed better than other commonly used soil moisture proxies (i.e.,

precipitation relevant index, products derived from land surface model and microwave remote sensing technology). Besides, by using the decomposed TWS to represent local moisture deficit, it played a more important role in influencing hot extreme occurrences in regions with a total area 1.6 times as large as the area strongly influenced by global temperature change during the study period 1985–2015. The results suggested that local land management is essential for combating hot extreme expansion in regions with strong land-atmosphere coupling, and global measures for reducing emissions are required in the face of increasing greenhouse gas forcing.

In summary, this thesis improved the knowledge of land-atmosphere interactions at continental and global scales through further investigation on TWS variation pattern and its relationships with vegetation and temperature. This thesis also suggested a useful soil moisture proxy, i.e., the wavelet decomposed GRACE TWS, that can be applied to examine other processes in land-atmosphere interactions and to evaluate the performance of land surface models.

DECLARATION

I certify that this thesis does not incorporate without acknowledgment any material previously submitted for a degree or diploma in any university; and that to the best of my knowledge and belief it does not contain any material previously published or written by another person except where due reference is made in the text.

Signed..... Ajiao Chen

Date..... 19/9/2021

ACKNOWLEDGEMENTS

I really appreciate Flinders University and China Scholarship Council (CSC) for providing me a fully funded PhD position to work on this thesis. I am very glad that I was born in China and grew up in such a good era which provided me the opportunity to study abroad. I remember that the first day I arrived at the airport of Adelaide, I realized that it was the start of a challenging journey in a totally new environment. But then the beautiful scenery in Adeliade and friendly people I met here greatly relieved my anxiety. I love this city and appreciate it for providing me so many good memories.

I feel so lucky to have the opportunity to work with my supervisors Prof. Huade Guan and Prof. Okke Batelaan, they are excellent in scientific research and patient in educating students. In the first half year of my PhD study, I was very confused about my research direction and often felt difficult to follow the topics discussed in our regular group meetings due to my poor knowledge background and English communication skill. Then with the help of my supervisors, the preliminary research topics of my PhD study have been built, and my research capacity and English have been improved gradually. Without their guidance, support, and efforts, the thesis would not be possible.

Being overseas for a couple of years, not only myself, but it was also a challenge for my families. I appreciate my parents for their understanding. During these years, every time I was in trouble in study or life, my husband Yi Cai gave me the most support and encouragement. Let's take responsibility and share joy together in the coming days. I am also grateful to our group members and other friends, e.g., Na Liu, Wenting Shi, Rose Deng, Yifei Zhou, Zidong Luo etc. We work, cook, play badminton, and travel together, I will never forget the beautiful memories.

LIST OF FIGURES

LIST OF TABLES

LIST OF FIGURES IN APPENDIX

1 INTRODUCTION

1.1 Basics of land-atmosphere interactions Introduction

Land surface and the atmosphere are coupled through a multitude of physical, chemical, and biological interactions and feedbacks that determine the fluxes of energy and mass (e.g., water and carbon dioxide (CO_2)) between the two systems (Oki, 1999). The land surface is heated by net radiation during the daytime, and a small part of the energy is absorbed by the ground while the majority is transferred back to the atmosphere as sensible (via conduction and convection) and latent heat (associated with evapotranspiration) (Betts and Ball, 1996; Jimenez et al., 2014). These processes depend on land surface characteristics, such as reflectivity, emissivity, surface roughness, soil type, vegetation cover, and amount and depth of roots, which are affected by land cover change resulted from natural processes or human activities (e.g., afforestation, deforestation, and urbanization) (Anderson et al., 2011). The moisture exchange between land surface and the atmosphere forms an important part of the water cycle on Earth. The water cycle connects the Earth's oceans, land, and atmosphere. Water molecules, leave from the Earth's surface through evapotranspiration (ET) to the atmosphere and back through precipitation, some infiltrate below the surface contributing to soil moisture and groundwater. Land cover changes play an important role in influencing the surface water budget, for example, ET is closely related to changes in vegetation cover; and urbanization can affect the precipitation formation process and surface water runoff (Daniels et al., 2016; Zhong et al., 2017). CO_2 exchange between land and the atmosphere is driven by plant photosynthesis and ecosystem respiration. Atmospheric CO_2 converts into organic compounds by plant photosynthesis providing source for plant growth, and at the same time carbon uptake by terrestrial ecosystems play an essential role in atmospheric CO_2 budget.

As shown in Figure 1.1 the land energy and water balances are coupled through evapotranspiration, they are also linked with the terrestrial carbon cycle. Plants play very important roles in those linkages, because carbon assimilation and evapotranspiration are tightly coupled via leaf stomata (Seneviratne and Stöckli, 2008; Lemordant et al., 2016).

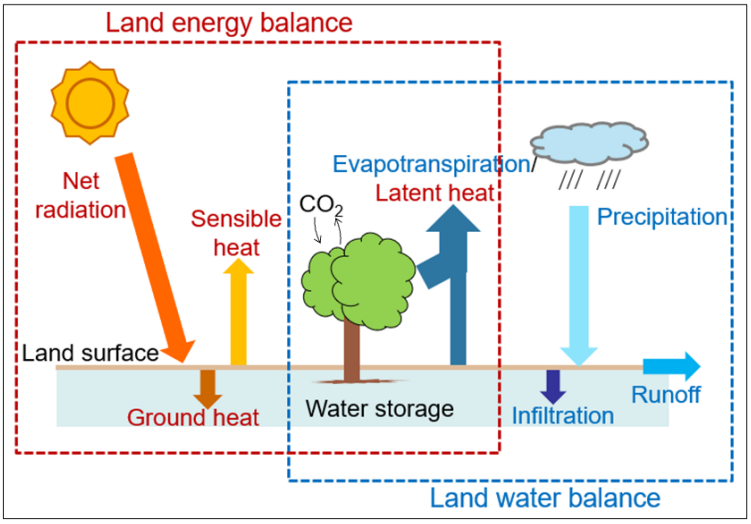

Figure 1.1 Schematic of land-atmosphere energy, water, and CO_2 exchanges

1.2 Recent advances in land-atmosphere interactions research

Incorporating physical processes of land-atmosphere interactions into climate projection models can advance climate predictability on several time and spatial scales (IPCC, 2019), and consequently make contribution to future climate change adaption and mitigation. In the context of climate warming, increasingly frequent extreme climate events are of important concern globally (e. g., Karoly, 2009; Perkins and Alexander, 2012; Coumou and Rahmstorf, 2012). Natural disasters such as droughts, floods, and heatwaves can pose serious threats to environmental and human health, which have been suggested to be intensified by anthropogenic greenhouse gas emissions. Therefore, improving the knowledge of land-atmosphere interactions and their responses to climate change could provide useful information for future sustainable land management (Santanello et al., 2018; Baker et al., 2021).

On the one hand, many physical processes of land-atmosphere interactions are increasingly being recognized, especially the relationships between soil moisture versus precipitation and temperature (e.g., Koster et al., 2004, Seneviratne et al., 2006; Berg et al., 2014), and vegetation responses and feedbacks to climate change. For example, Alexander, (2011) revealed the mechanism that soil moisture strongly influences the surface energy budget and partitioning between latent and sensible heat fluxes (i.e., low soil moisture availability reduces evaporative cooling and increases atmospheric heating from sensible heat flux), and then the effects of antecedent moisture deficit on hot extremes have been investigated at both global and regional scales (e. g., Fischer et al., 2007; Perkins et al., 2015; Herold et al, 2016; Vogel et al., 2017);

vegetation as a typical carbon sink and the major conduit for water to return to the atmosphere from land, its important role in regulating land water balance and influencing the land-atmosphere interactions have been reported (Donohue et al., 2009; Gerten et al., 2004; Heimann and Reichstein, 2008). With improved understanding for those physical processes, representations of vegetation dynamics, stomatal functioning, plant hydraulics and many other processes have been incrementally added into land surface models (LSMs) (e.g., Joetzjer et al., 2018; Lawrence et al., 2019; Kennedy et al., 2019).

On the other hand, improved observations and model outputs of key variables made considerable contribution to characterizing and quantifying land-atmosphere interactions. Data from models of the Coupled Model Intercomparison Project (e.g., CMIP phase 6 (Eyring et al., 2016)) for historical and future climate change experiments were used to examine changes in variables, fluxes, and metrics relevant to land-atmosphere interactions. By using the model outputs, a much broader evaluation became possible than past studies of land-atmosphere interactions (Dirmeyer et al., 2013). In addition, advancements in the spatial and temporal coverage and accuracy of satellite remote sensing-based estimates of terrestrial and atmospheric variables have been seen in the recent two decades (e.g., Owe et al., 2008; Ferguson and Wood, 2011; Susskind et al., 2011; Balsamo et al., 2018). Remote sensing observations are particularly useful in examining land-atmosphere interactions, and such observational evidence can be used to evaluate the performance of LSMs (Balsamo et al., 2018). Research advances in land-atmosphere interactions were also profit from the use of another newly available observation, i.e., the FLUXNET measurements (Seneviratne et al., 2010). FLUXNET is a global network of eddy covariance towers, which generates measurements on the exchanges of energy, water vapor, and carbon dioxide between terrestrial ecosystems and the atmosphere (Suni et al., 2015). Combining the FLUXNET measurements and the broad areal coverage of satellite observations and model outputs improved the availability of key variables (e.g., temperature, vegetation, albedo etc.) for characterizing the physical processes of land-atmosphere interactions for various ecosystems across a range of bioclimate zones (Jung et al., 2011; Fernandez-Prieto et al., 2013; Dirmeyer et al., 2018).

1.3 Challenges in representing and predicting land-atmosphere interactions

It is undoubted that land-atmosphere interactions provide promising perspectives for future research, however, the multivariate and multiscale coupled processes remain incompletely understood (Fisher and Koven, 2020; Jimenez et al., 2021). Thus, identifying variation patterns of

hydroclimatological variables and exploring the corresponding mechanisms are required to improve such knowledge. In addition, the lack of suitable data of key variables of large-scale, such as soil moisture and evapotranspiration, for robustly characterizing model performance, is also a challenge (Seneviratne et al., 2010; Wulfmeyer et al., 2016).

Australia is identified as a hot spot of land-atmosphere coupling (Mueller and Seneviratne, 2012). It is the driest inhabitant continent and frequently affected by natural disasters, such as bushfires, cyclones, droughts, and floods. Those natural disasters cause recurring threats to water supply, agriculture, and the environment in Australia. Existing studies mainly focused on the causes of extreme wet or dry events in specific periods and their impacts on agriculture and ecosystems in this region (e.g., Kiem and Verdon-Kidd, 2010; Nicholls, 2011; Van Dijk et al., 2013). However, characterization and understanding long-term wetting/drying pattern are still lacking in Australia. On the other hand, wet and dry conditions are commonly acknowledged to influence vegetation growth as plant growth is dependent on water availability. For example, Yang et al. (2014) and Andrew et al. (2017a) examined the impact of terrestrial water storage on vegetation. However, vegetation changes also strongly influence terrestrial water condition by regulating evapotranspiration (Wei et al., 2018) and altering the terrestrial water cycle (Zeng et al., 2018). Ecosystems in Australia have the capacity to persist through extremely dry periods and respond favourably during a subsequent wet period (Cleverly et al., 2016). Therefore, it is valuable to investigate the interactions between vegetation and terrestrial water condition in Australia, which is remained poorly understood. As vegetation and terrestrial water condition play important roles in modifying the surface energy and fluxes of moisture and carbon (Pongratz et al., 2006; Seneviratne et al., 2010; Humphrey et al., 2021), filling those knowledge gaps could improve our understanding for the physical processes of land-atmosphere interaction in Australia.

The scarcity of soil moisture observations impedes the investigations on large-scale soil moisture-climate interactions (Seneviratne et al., 2010). Ground measurements including gravimetric measurements and in-situ measurements are cost-intensive and lack large spatial coverage (Robock et al., 2000; Robinson et al., 2008). Global coverage is possible in land surface modelling with observation-based forcing and remote sensing measurements. However, model derived products, such as the Global Land Data Assimilation System dataset (GLDAS, Rodell et al., 2004) and the Global Soil Wetness Project 2 dataset (GSWP-2, Dirmeyer et al., 2006), are dependent on quality of forcing data. Remote sensing measurements, such as the Soil Moisture and Oceanic Salinity (SMOS, Kerr et al., 2016), and the Soil Moisture Active and Passive (SMAP, Entekhabi et al.,

2010), only provide direct sensing of soil moisture in the top 5 cm of the soil column. Several applications require knowledge of root zone soil moisture in deeper soil column, which is not directly measured by those microwave remote sensing technologies. The availability of a more useful soil moisture proxy would help to improve the quantification of its interaction with climate variables and could be applied to evaluate the performance of land surface models.

1.4 GRACE provides new opportunities for examining large-scale land-atmosphere interactions

The twin satellites of the Gravity Recovery and Climate Experiment (GRACE), launched in March 2002, were aimed to capture changes of terrestrial and ocean water/ice mass by tracking changes of the Earth's gravity. The mission was initially planned for operation for a 5-year period. It has been so successful as to have collected more than 15 years of data by its decommissioning in June 2017. The Terrestrial Water Storage (TWS) is a mathematical function of the Earth's gravity field, after atmospheric and oceanic effects are accounted for, it represents the sum of soil moisture, groundwater, surface water, snow, and ice (Watkins et al., 2015; Wiese et al., 2016). GRACE TWS can be used as an indicator for the regional terrestrial water conditions. Efforts have been made to reconstruct TWS data beyond the GRACE mission period (e.g., Humphrey et al., 2017; Humphrey and Gudmundsson, 2019). These extended TWS data provide opportunities to make up the lack of investigation on long-term spatio-temporal patterns of wetting and drying on large scale, and to relate the TWS variation pattern to other hydroclimatological variables.

Given that GRACE TWS represents the changes in total water storage including that of soil moisture, Andrew et al. (2017b) suggested a discrete wavelet decomposition method to separate the total water storage into different components. It has been demonstrated that the decomposed TWS has an improved capacity in capturing the soil moisture and vegetation relationship (Andrew et al., 2017a). It is because that those decomposed TWS components of different temporal scales can reflect temporal dynamics of moisture at different depths. This is based on the understanding that moisture at various soil depths has different response times to the climate system. It is possible that moisture storage with response timescales of several months could impact energy balance partitioning at the land surface and consequently influence near-surface temperature. Thus, the decomposed TWS has potential for examining land-atmosphere interactions such as the coupling between soil moisture and air temperature.

1.5 Objectives

The overarching aim of this thesis is to improve our knowledge of physical processes of large-scale land-atmosphere interactions by investigating the variation patterns of hydroclimatological variables and their connections, and to find out useful soil moisture proxy that can be applied for examining its relationship with atmospheric variables. The corresponding results are expected to advance future climate predictability and to provide useful information for future sustainable land management to improve climate change adaption and mitigation. Specifically, the questions this thesis aims to address are:

(1) Is there a predictable large-scale wetting/drying pattern in Australia? Such a pattern, if there is, would be useful for forest, agriculture, and water resources management. Recent studies have revealed some spatial coherent variation patterns (e.g., Xie et al., 2016; Xie et al., 2019), however, how these patterns vary with time is not known. This thesis aims to examine the long-term spatio-temporal variation pattern of TWS over Australia.

(2) In what areas strong interactions exist between TWS and vegetation in Australia? Such knowledge is required in understanding and simulating terrestrial water and carbon budgets in response to climate change. Previous studies have already investigated the impact of terrestrial water storage on vegetation in this continent (e.g., Yang et al., 2014; Andrew et al., 2017a), however, the role of vegetation in influencing terrestrial water condition remains poorly understood. This thesis aims to investigate the interactions between TWS and vegetation over Australia.

(3) Is GRACE TWS a useful proxy for soil moisture? If yes, it would be expected to make contribution in improving the quantification of soil moisture-climate interactions and reducing uncertainties of climate projection models. The wavelet decomposed GRACE TWS has been successfully applied to reveal the moisture dependence of vegetation cover at different temporal resolutions recently (Andrew et al., 2017a). It implies the potential of the decomposed TWS as a soil moisture proxy to be used for investigating land-atmosphere interactions. This thesis aims to examine the applicability of the decomposed TWS in investigating global soil moisture-air temperature coupling.

(4) Which factor, global temperature change or regional land-atmosphere coupling, is more important in influencing hot extremes? Such knowledge could provide useful information for the development of adaptation strategies for increasing hot extremes. Effects of global warming and

local land-atmosphere coupling on hot extremes have been separately investigated in previous studies (e.g., Rahmstorf and Coumou, 2011; Herold et al., 2016; Perkins-Kirkpatrick and Gibson, 2017), but their relative contribution have not been compared yet. This thesis aims to quantify the relative importance of global temperature change and local soil moisture deficit in influencing hot extremes.

1.6 Thesis structure

The structure of this thesis is shown as follow:

Chapter Number	Chapter Title	Main Content
1	Introduction	Background, research gaps, objectives, and main structure of this thesis
2	Seesaw terrestrial wetting and drying between eastern and western Australia	Investigating the long-term wetting/drying variation pattern of Australia and its association with other land surface processes and atmospheric variables.
3	Non-linear interactions between vegetation and terrestrial water storage in Australia	Investigating the non-linear interactions between vegetation and terrestrial water storage in Australia.
4	Global soil moisture-air temperature coupling based on GRACE-derived terrestrial water storage	Evaluating the applicability of wavelet decomposed GRACE TWS in investigate global soil moisture-temperature coupling by comparing with other commonly used soil moisture proxies.
5	Spatially differentiated effects of local moisture deficit on hot extremes in comparison to global temperature change	Comparing the relative importance of global temperature change and local land-atmosphere coupling in influencing the occurrence of hot extreme at the global scale.
6	Conclusions	Conclusions and future research interests
Appendix	Further analyses expanded on the TWS seesaw phenomenon found in Chapter 2.	An initial analysis on the 2009 Black Saturday bushfire occurred in Victoria, Australia

The connections of the four main chapters are demonstrated in Figure 1.2. Firstly, Chapter 2 reveals the variation pattern of TWS, a key variable in land-atmosphere interactions, at a continental scale. The study area Australia is a water-limited region, where surface vegetation condition is deeply dependent on land water condition, and on the contrary, surface vegetation condition can also modify land water condition. Therefore, Chapter 3 investigates the interactions between TWS and vegetation over Australia. Land surface processes are usually closely associated with atmospheric variables (e.g., temperature, precipitation, wind), for example, soil moisture regulates near surface temperature through influencing evapotranspiration. Then, Chapter 4 applies

the wavelet decomposed TWS as a soil moisture proxy to examine the soil moisture-air temperature coupling at the global scale. Finally, Chapter 5 compares the relative contribution of local land-atmosphere interaction and global temperature change in influencing hot extremes. Such results would contribute to developing practical advice to mitigating negative impacts of hot extremes on the environment and society.

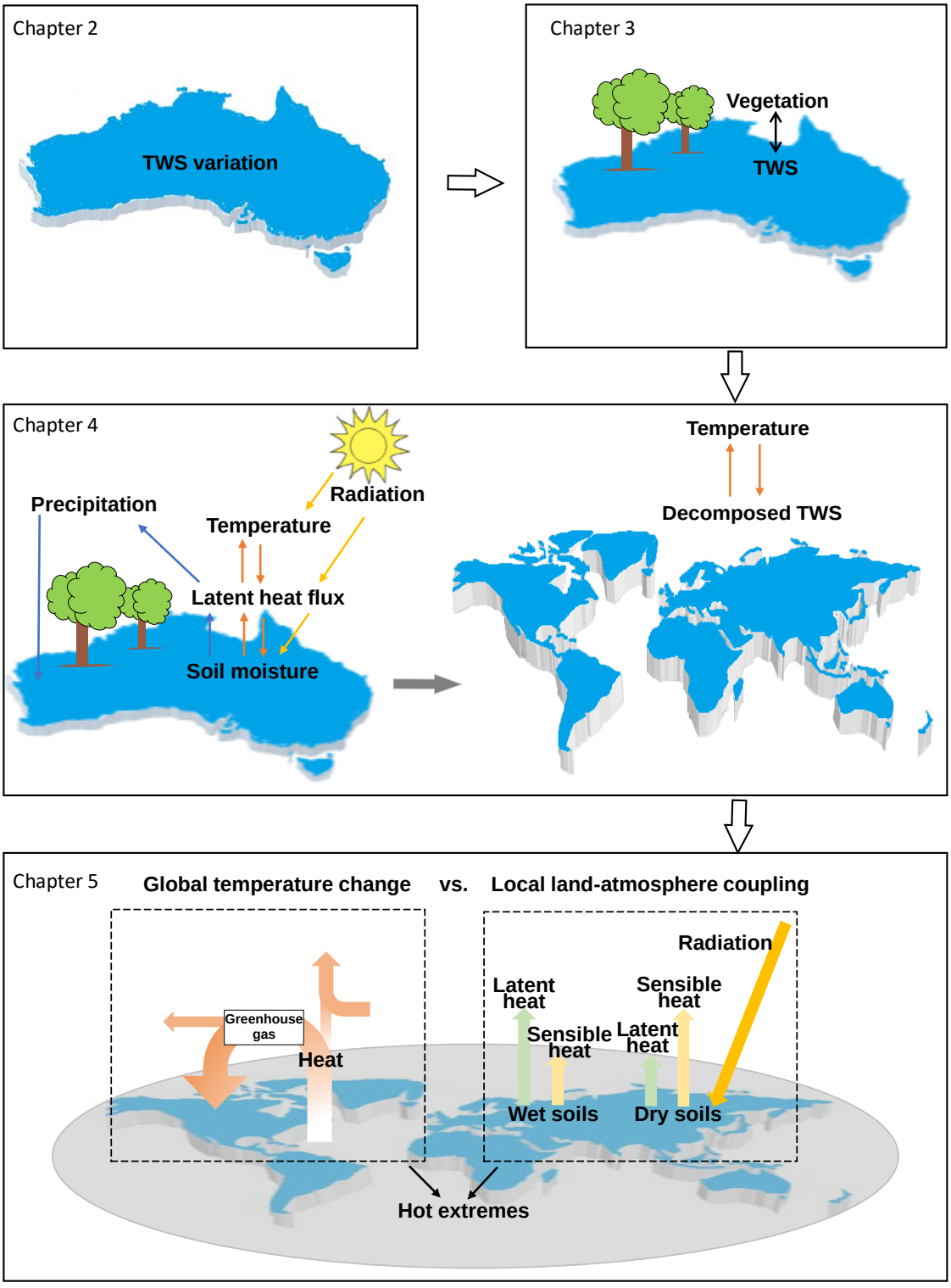

Figure 1.2 Connections of four main chapters of this thesis. Chapter 2 investigates the long-term TWS variation pattern of Australia, and Chapter 3 investigates the interactions between TWS and vegetation in Australia. Then, Chapter 4 uses wavelet decomposed TWS to examine the coupling between soil moisture and air temperature at a global scale, and Chapter 5 compares the relative importance of global temperature change and local land-atmosphere coupling in influencing the occurrence of hot extremes.

1.7 Publications

[1] Ajiao Chen, Huade Guan, Okke Batelaan. Seesaw terrestrial wetting and drying between eastern and western Australia. Earth's Future, 9, e2020EF001893. https://doi. Org/10.1029/2020EF001893

[2] Ajiao Chen, Huade Guan, Okke Batelaan. Nonlinear interactions between vegetation and terrestrial water storage in Australia. (Prepared for submission to Journal of Hydrology)

[3] Ajiao Chen, Huade Guan, Okke Batelaan, Xinping Zhang, Xinguang He. Global soil moisture-air temperature coupling based on GRACE-derived terrestrial water storage. Journal of Geophysical Research: Atmospheres. 2019, 124. https://doi.org/10.1029/2019JD030324

[4] Ajiao Chen, Huade Guan, Okke Batelaan. Spatially differentiated effects of local moisture deficit on hot extremes in comparison to global temperature change. (Submitted for review in Journal of Hydrology)

1.8 References

Alan K. Betts and John H. Ball. 1996. The land surface-atmosphere interaction: A review based on observational and global modelling perspectives. Journal of Geophysical Research, 101(D3), 7209–7225.

Alexander, L. 2011. Climate science: Extreme heat rooted in dry soils. Nature Geoscience., 4 (1), 12–13.

Anderson, R.G., Canadell, J.G., Randerson, J.T., Jackson, R.B., Hungate, B.A., Baldocchi, D.D., Ban-Weiss, G.A., Bonan, G.B., Caldeira, K., Cao, L., Diffenbaugh, N.S., Gurney, K.R., Kueppers, L.M., Law, B.E., Luyssaert, S. and O'Halloran, T.L. 2011. Biophysical considerations in forestry for climate protection. Frontiers in Ecology and the Environment., 9, 174–182.

Andrew, R., Guan, H., Batelaan, O. 2017a. Large-scale vegetation responses to terrestrial moisture storage changes. Hydrology and Earth System Science., 21, 4469–4478.

Andrew, R. A., Guan, H., Batelaan, O. 2017b. Estimation of GRACE water storage components by temporal decomposition. Journal of Hydrology., 552, 341–350.

Baker, J. C. A., Castilho de Souza, D., Kubota, P. Y., Buermann, W., Coelho, C. A. S., Andrews, M. B., Gloor, M., Garcia-Carreras, L., Figueroa, S. N., & Spracklen, D. V. 2021. An Assessment of Land-Atmosphere Interactions over South America Using Satellites, Reanalysis, and Two Global Climate Models, Journal of Hydrometeorology, 22(4), 905–922.

Balsamo, G., Agusti-Panareda, A., Albergel, C., Arduini, G., Beljaars, A., Bidlot, J., Blyth, E., et al. 2018. Satellite and In Situ Observations for Advancing Global Earth Surface Modelling: A Review. Remote Sensing. 10, 2038.

Berg, A., Lintner, B. R., Findell, K. L., Malyshev, S., Loikith, P. C., Gentine, P. 2014. Impact of Soil Moisture-Atmosphere Interactions on Surface Temperature Distribution, Journal of Climate, 27(21), 7976–7993.

Cleverly, J., Eamus, D., Luo, Q., Restrepo-Coupe, N., Kljun, N., Ma, X., Ewenz, C., Li, L., Yu, Q.H., Alfredo, A. 2016. The importance of interacting climate modes on Australia's contribution to global carbon cycle extremes. Scientific Report. 6, 23113.

Coumou, D. and Rahmstorf, S. 2012. A decade of weather extremes. Nature Climate Change., 2 (7), 491–496.

Daniels, E.E., G. Lenderink, R.W.A. Hutjes, and A.A.M. Holtslag, 2016. Observed urban effects on precipitation along the Dutch west coast. International Journal of Climatology., 36, 2111–2119.

Dirmeyer, P., Gao, X., Zhao, M., Guo, Z., Oki, T., Hanasaki, N. 2006. GSWP-2: multimodel analysis and implications for our perception of the land surface. Bulletin of the American Meteorological Society., 87,1381–1397.

Dirmeyer, P. A., Jin, Y., Singh, B., Yan, X. 2013. Trends in Land-Atmosphere Interactions from CMIP5 Simulations. Journal of Hydrometeorology, 14 (3), 829–849.

Dirmeyer, P. A., Chen, L., Wu, J., Shin, C.-S., Huang, B., Cash, B. A., et al. 2018. Verification of land-atmosphere coupling in forecast models, reanalyses and land surface models using flux site observations. Journal of Hydrometeorology, 19(2), 351–373.

Donohue, R., McVicar, T., Roderick, M. 2009. Climate-related trends in Australian vegetation cover as inferred from satellite observations, 1981-2006. Global Change Biology., 15, 1025–1039.

Entekhabi, D., Njoku, E.G., O'Neill, P.E., Kellogg, K.H., Crow, W.T., Edelstein, W.N., Entin, J.K., Goodman, S.D., Jackson, T.J., Johnson, J. 2010. The Soil Moisture Active Passive (SMAP) Mission. Proc. IEEE. 98, 704–716.

Ferguson, C. R. and Wood, E. F. 2011. Observed Land–Atmosphere Coupling from Satellite Remote Sensing and Reanalysis, Journal of Hydrometeorology, 12(6), 1221–1254.

Fernández-Prieto, D., Kesselmeier, J., Ellis, M., Marconcini, M., Reissell, A., Suni, T. 2013. Earth observation for land-atmosphere interaction science. Biogeosciences. 10. 261–266.

Fischer, E., Seneviratne, S., Vidale, P., Lüthi, D. and Schär, C. 2007. Soil moisture ‐ atmosphere interactions during the 2003 European summer heatwave. Journal of Climate., 20, 5081–5099.

Fisher, R. A. and Koven, C. D. 2020. Perspectives on the future of land surface models and the challenges of representing complex terrestrial systems. Journal of Advances in Modeling Earth Systems, 12, e2018MS001453.

Gerten, D., Schaphoff, S., Haberlandt, U., Lucht, W., Sitch, S. 2004. Terrestrial vegetation and water balance-hydrological evaluation of a dynamic global vegetation model. Journal of Hydrology., 286, 249–270.

Heimann, M. and Reichstein, M. 2008. Terrestrial ecosystem carbon dynamics and climate feedbacks. Nature., 451, 289–292.

Herold, N., Kala, J. and Alexander, L. V. 2016. The influence of soil moisture deficits on Australian heatwaves. Environmental Research Letters., 11, 064003.

Humphrey, V., Gudmundsson, L., Seneviratne, S. I. 2017. A global reconstruction of climate-driven subdecadal water storage variability. Geophysical Research Letters, 44, 2300–2309.

Humphrey, V. and Gudmundsson, L. 2019. GRACE-REC: a reconstruction of climate-driven water storage changes over the last century. Earth System Science Data, 11(3), 1153–1170.

Humphrey, V., Berg, A., Ciais, P., Gentine, P., Jung, M., Reichstein, M., Seneviratne, S. I. and Frankenberg, C. 2021. Soil moisture-atmosphere feedback dominates land carbon uptake variability. Nature., 592, 65–69.

IPCC, 2019. Climate Change and Land: an IPCC special report on climate change, desertification, land degradation, sustainable land management, food security, and greenhouse gas fluxes in terrestrial ecosystems [P.R. Shukla, J. Skea, E. Calvo Buendia, V. Masson-Delmotte, H.-O. Pörtner, D. C. Roberts, P. Zhai, R. Slade, S. Connors, R. van Diemen, M. Ferrat, E. Haughey, S.

Luz, S. Neogi, M. Pathak, J. Petzold, J. Portugal Pereira, P. Vyas, E. Huntley, K. Kissick, M. Belkacemi, J. Malley, (eds.)]. In press.

Jimenez, P. A., de Arellano, J. V.-G., Navarro, J., Gonzalez-Rouco, J. F, 2014. Understanding land-atmosphere interactions across a range of spatial and temporal scales. Bulletin of the American Meteorological Society. 95, ES14–ES17.

Joetzjer, E., Maignan, F., Chave, J., Goll, D., Poulter, B., Barichivich, J., et al, 2018. Effect of the importance of tree demography and flexible root water uptake for modelling the carbon and water cycles of Amazonia. Biogeosciences Discussions, 1–33.

Jung, M., Reichstein, M., Margolis, H.A., Cescatti, A., Richardson, A.D., Arain, M.A., Arneth, A. et al. 2011. Global patterns of land-atmosphere fluxes of carbon dioxide, latent heat, and sensible heat derived from eddy covariance, satellite, and meteorological observations. Journal of Geophysical Research. Biogeosciences. 116, G00J07.

Karoly, D. 2009. The recent bushfires and extreme heatwave in southeast Australia. Bulletin of the Australian Meteorological and Oceanographic Society., 22, 10–13.

Kennedy, D., Swenson, S., Oleson, K. W., Lawrence, D. M., Fisher, R., Lola da Costa, A. C., Gentine, P, 2019. Implementing plant hydraulics in the Community Land Model, Version 5. Journal of Advances in Modeling Earth Systems, 11, 485–513.

Kerr, Y.H., Al-Yaari, A., Rodriguez-Fernandez, N., Parrens, M., Molero, B., Leroux, D., Bircher, S., Mahmoodi, A., Mialon, A., Richaume, P. 2016. Overview of SMOS performance in terms of global soil moisture monitoring after six years in operation. Remote Sensing of Environment. 180, 40–63.

Kiem, A. and Verdon-Kidd, D. 2010. Towards understanding hydroclimatic change in Victoria, Australia-preliminary insights into the “big dry”. Hydrology and Earth System Science., 14, 433–445.

Koster, R.D., Dirmeyer, P.A., Guo, Z.C., Bonan, G., Chan, E., Cox, P., Gordon, C.T., Kanae, S., Kowalczyk, E., Lawrence, D., Liu, P., Lu, C.H., Malyshev, S., McAvaney, B., Mitchell, K., Mocko, D., Oki, T., Oleson, K., Pitman, A., Sud, Y.C., Taylor, C.M., Verseghy, D., Vasic, R., Xue, Y.K., Yamada, T. 2004. Regions of strong coupling between soil moisture and precipitation. Science., 305, 1138–1140.

Lawrence, D. M., Fisher, R. A., Koven, C. D., Oleson, K. W., Swenson, S. C., Bonan, G., et al, 2019. The Community Land Model Version 5: Description of new features, benchmarking, and impact of forcing uncertainty. Journal of Advances in Modeling Earth Systems, 11, 4245–4287.

Lemordant, L., Gentine, P., Stéfanon, M., Drobinski, P., and Fatichi, S. (2016), Modification of land-atmosphere interactions by CO2 effects: Implications for summer dryness and heat wave amplitude, Geophysical Research Letters., 43, 10,240–10,248.

Nicholls, N. 2011. What caused the eastern Australia heavy rains and floods of 2010/11? Bulletin of the Australian Meteorological and Oceanographic Society., 24, 33–34.

Oki, T., 1999. The global water cycle. In: Browning K, Gurney R (eds) Global energy and water cycles. Cambridge University Press, Cambridge/New York, pp 10–27.

Owe, M., de Jeu R., Holmes T. 2008: Multisensor historical climatology of satellite-derived global land surface moisture. Journal of Geophysical Research. 113.

Perkins, S. and Alexander, L. 2012. On the measurement of heat waves. Journal of climate., 26, 4500–4515.

Perkins, S., Argüeso, D., White, C. 2015. Relationships between climate variability, soil moisture, and Australian heatwaves. Journal of geophysical research-Atmospheres., 120, 8144–814.

Perkins-Kirkpatrick, S. E. and Gibson, P.B. 2017. Changes in regional heatwave characteristics as a function of increasing global temperature. Scientific Report, 7, 12256 (2017).

Pongratz, J., Bounoua, L., DeFries, R., Morton, D., Anderson, L., Mauser, W., Klink, C. 2006. The Impact of Land Cover Change on Surface Energy and Water Balance in Mato Grosso, Brazil. Earth Interactions., 10(19). 1–17.

Rahmstorf, S. and Coumou, D. 2011. Increase of extreme events in a warming world. Proceedings of the National Academy of Sciences of the United States of America. 108(44), 17905–17909.

Robinson, D., Campbell, C., Hopmans, J., Hornbuckle, B., Jones, S., Knight, R., Ogden, F., Selker, J., Wendroth, O. 2008. Soil moisture measurements for ecological and hydrological watershed scale observatories: a review. Vadose Zone Journal., 7, 358–389.

Robock, A., Vinnikov, K., Srinivasan, G., Entin, J., Hollinger, S., Speranskaya, N., Liu, S., Namkhai, A. 2000. The global soil moisture data bank. Bulletin of the Australian Meteorological and Oceanographic Society., 81 (6), 1281–1299.

Rodell, M., Houser, P., Jambor, U., Gottschalck, J., Mitchell, K., Meng, C., Arsenault, K., Cosgrove, B., Radakovich, J., Bosilovich, M., Entin, J.,Walker, J., Lohmann, D., Toll, D. 2004. The global land data assimilation system. Bulletin of the Australian Meteorological and Oceanographic Society., 85 (3),381–394.

Santanello, J., Jr., Dirmeyer, P., Ferguson, C., Findell, K., Tawfik, A., Berg, A., Ek, M., Gentine, P., Guillod, B., van Heerwaarden, C., Roundy, J., Wulfmeyer, V. 2018. Land-Atmosphere Interactions: The LoCo Perspective, Bulletin of the American Meteorological Society., 99(6), 1253–1272.

Seneviratne, S.I., Lüthi, D., Litschi, M., Schär, C., 2006. Land-atmosphere coupling and climate change in Europe. Nature 443, 205–209.

Seneviratne S., Stöckli R. 2008. The Role of Land-Atmosphere Interactions for Climate Variability in Europe. In: Brönnimann S., Luterbacher J., Ewen T., Diaz H., Stolarski R., Neu U. (eds) Climate Variability and Extremes during the Past 100 Years. Advances in Global Change Research, vol 33. Springer, Dordrecht.

Seneviratne, S., Corti, T., Davin, E.., Hirschi, M., Jaeger, E.., Lehner, I., Orlowsky, B. Teuling, A. 2010. Investigating soil moisture-climate interactions in a changing climate: A review. Earth Science Review., 99, 125–161.

Suni, T., Guenther, A., Hansson, H.C., Kulmala, M., Andreae, M.O., Arneth, A., Artaxo, P. et al., 2015. The significance of land-atmosphere interactions in the Earth system-iLEAPS achievements and perspectives. Anthropocene, 12, 69–84,

Susskind, J.,Blaisdell J. M., Iredell L., Keita F. 2011. Improved temperature sounding and quality control methodology using AIRS/AMSU data: The AIRS Science Team Version 5 retrieval algorithm. IEEE Transactions on Geoscience and Remote Sensing. 49, 883–907.

Van Dijk, A.., Beck, H., Crosbie, R., Jeu, R., Liu, Y., Podger, G., Timbal, B. Viney, N. 2013. The Millennium Drought in southeast Australia (2001-2009): Natural and human causes and implications for water resources, ecosystems, economy, and society. Water Resources Research., 49.

Vogel, M., Orth, R., Cheruy, F., Hagemann, S., Lorenz, R., Hurk, B., Seneviratne, S. I. 2017. Regional amplification of projected changes in extreme temperatures strongly controlled by soil moisture – temperature feedbacks. Geophysical Research Letters., 44, 1511–1519.

Watkins, M., Wiese, D., Yuan, D., Boening, C. Landerer, F. 2015. Improved methods for observing Earth's time variable mass distribution with GRACE using spherical cap mascons. Journal of Geophysical Research-Solid Earth., 120, 2648–2671.

Wei, X., Li, Q., Zhang, M., Giles-Hansen, K., Liu, W., Fan, H., Wang, Y., Zhou, G., Piao, S., Liu, S. 2018. Vegetation cover-another dominant factor in determining global water resources in forested regions. Global Change Biology., 24, 786–795.

Wiese, D., Landerer, F. Watkins, M. 2016. Quantifying and reducing leakage errors in the JPL RL05M GRACE mascon solution. Water Resources Research., 52, 7490–7502.

Wulfmeyer, V., and D. Turner, 2016. Land-Atmosphere Feedback Experiment (LAFE) science plan. Rep. DOE/SC-ARM-16-038, 34 pp., www.arm.gov/publications/programdocs/doe-sc-arm-16-038.pdf.

Xie, Z., Huete, A., Restrepo-Coupe, N., Ma, X., Devadas, R., Caprarelli, G. 2016. Spatial partitioning and temporal evolution of Australia's total water storage under extreme hydroclimatic impacts. Remote Sensing of Environment, 183, 43–52.

Xie, Z., Huete, A., Cleverly, J., Phinn, S., McDonald-Madden, E., Cao, Y., Qin, F. 2019. Multi-climate mode interactions drive hydrological and vegetation responses to hydroclimatic extremes in Australia. Remote Sensing of Environment, 231, 111270.

Yang, Y., Long, D., Guan, H., Scanlon, B., Simmons, C. Jiang, L., Xu, X. 2014. GRACE satellite observed hydrological controls on interannual and seasonal variability in surface greenness over mainland Australia. Journal of Geophysical Research-Biogeosciences., 119, 2245–2260.

Zeng, Z., Piao, S., Li, L.Z., Wang, T., Ciais, P., Lian, X., Yang, Y., Mao, J., Shi, X., Myneni, R. 2018. Impact of earth greening on the terrestrial water cycle. Journal of Climate., 31, 2633-26.

Zhong, S. Qian, Y., Zhao, C., Leung, R., Wang, H., Yang, B., Fan, J., Yan, H., Yang, X., Liu, D, 2017. Urbanization-induced urban heat island and aerosol effects on climate extremes in the Yangtze River Delta region of China. Atmospheric Chemistry and Physics., 17, 5439–5457.

2 SEESAW TERRESTRIAL WETTING AND DRYING BETWEEN EASTERN AND WESTERN AUSTRALIA

2.1 Introduction

Australia is the driest inhabited continent on Earth and among the areas of the most variable rainfall in the world (Nicholls et al., 1997; Dey et al., 2019). Its hydroclimatic variations play an important role in the global carbon and water cycles (Ahlström et al., 2015; Xie et al., 2016), occurrence of natural hazards (Johnson et al., 2016; Kiem et al., 2016), and agricultural productivity (Ma et al., 2015). Droughts occurring in Australia during 2000–2009 were reported to have reduced global terrestrial net primary production (Zhao and Running, 2010). Poulter et al. (2014) indicated that the global land carbon sink anomaly triggered by the 2010–2011 La Niña event was largely due to an enhanced ecosystem productivity across the Southern Hemisphere, particularly in Australia. Frequent droughts cause agricultural losses (Heberger, 2012; Van Dijk et al., 2013), contribute to bushfires (Sharples et al., 2016) and exacerbate heatwaves (Herold et al., 2016; Perkins-Kirkpatrick et al., 2016), and consequently impact the economy and society significantly (Van Dijk et al., 2013). This continent is also prone to floods, which lead to serious casualties and economic losses (Johnson et al., 2016). Hence, furthering our understanding and monitoring of wet and dry conditions in Australia is urgently needed for water, agriculture, and disaster risk management.

Previous studies mainly focused on the causes of droughts or floods in discrete periods and their impacts on ecosystems and society (Kiem and Verdon-Kidd, 2010; Nicholls, 2011; Van Dijk et al., 2013; Johnson et al., 2016; Kiem et al., 2016). Hydroclimatic extremes in Australia are usually attributed to the combined effect of large-scale climate modes such as El Niño Southern Oscillation (ENSO), Indian Ocean Dipole (IOD), and Inter-decadal Pacific Oscillation (IPO) (e.g., Ummenhofer et al., 2009; Verdon-Kidd and Kiem, 2009a, 2009b, 2014; King et al., 2020). The indices of these climate oscillation systems are reported to have strong correlation with rainfall/streamflow in Australia (Kiem et al., 2003; Franks, 2004; Power et al., 2006; Cai et al., 2011). El Niño (La Niña) tends to increase the possibility of dry (wet) conditions across many parts of Australia (Nicholls, 1992; Power et al., 2006; Risbey et al., 2009). For example, an abnormal wet period in 2010–2011 was reportedly driven by one of the strongest La Niña events in the past nine decades (Nicholls, 2011; Trenberth, 2012; Evans and Boyer-Souchet, 2012; Christidis et al., 2013; King et al., 2013). Xie et al. (2016) recently investigated the wet and dry evolution across continental Australia based on Gravity Recovery and Climate Experiment (GRACE) terrestrial water storage (TWS) data set (2002–2014).

They revealed three geographic zones with distinct TWS responses and attributed them to different large-scale teleconnections. If such regional differentiated TWS responses hold over a long period, it would provide society useful information for climate-adaptive water resource planning and management. In this study, we aim to reveal long-term spatio-temporal patterns of TWS in Australia, and to examine how these patterns are associated with climate variability and land surface processes.

2.2 Methodology

2.2.1 TWS data

Three TWS datasets are used in this study. The first is the original GRACE TWS data set (RL06M.MSCNv01) (Watkins et al., 2015; Wiese et al., 2016) from 2003 to 2016 provided by the NASA Jet Propulsion Laboratory (JPL), which are available from https://grace.jpl.nasa.gov/. Seventeen months of missing TWS data (June 2003, January 2011, June 2011, May 2012, October 2012, March 2013, August 2013, September 2013, February 2014, July 2014, December 2014, June 2015, October 2015, November 2015, April 2016, September 2016, and October 2016) are filled by linear interpolation using the months either side (Long et al., 2015; Andrew et al., 2017). In order to investigate the wetting and drying cycles over a long period, two reconstructed GRACE TWS datasets for 1985–2015 (Humphrey et al., 2017; http://rossa-prod-ap21.ethz.ch/delivery/DeliveryManagerServlet?dps_pid=IE5766472) and for 1901–2014 (Humphrey and Gudmundsson, 2019; https://doi.org/10.6084/m9.figshare.7670849) are also applied. The TWS data set of 1901–2014 was reconstructed from statistical data-driven models, calibrated with observations, which performs well in comparison with state-of-the-art hydrological models (Humphrey and Gudmundsson, 2019; Padrón et al., 2020). The seasonality of TWS has been removed by subtracting monthly averages, resulting in what is referred to as TWS anomaly in this study. All TWS datasets are of 0.5° × 0.5° spatial resolution.

2.2.2 Vegetation index

Global Inventory Monitoring and Modeling System (GIMMS) Normalized Difference Vegetation Index (NDVI) data set (Tucker et al., 2005; Pinzon and Tucker, 2014) is available from July 1981 to December 2015, which was downloaded from https://climatedataguide.ucar.edu/climate-data/ndvi-normalized-difference-vegetation-index-3rd-generation-nasagfsc-gimms. Moderate Resolution Imaging Spectroradiometer (MODIS) NDVI data set (Didan et al., 2015) is available from March 2000, which was downloaded from

https://neo.sci.gsfc.nasa.gov/view.php?datasetId=MOD_NDVI_M. MODIS NDVI data are of 0.5° × 0.5° spatial resolution, and the GIMMS NDVI data were remapped from 1/12° × 1/12° to 0.5° × 0.5° in this study.

2.2.3 Model-derived evapotranspiration, soil Moisture, and precipitation data

GLDAS_NOAH025_M evapotranspiration data (Rodell et al., 2004; Beaudoing and Rodell, 2015) are of 0.25°×0.25° spatial resolution, which were downloaded from https://disc.gsfc.nasa.gov/datasets/GLDAS_NOAH025_M_2.0/summary?keywords=GLDAS. Soil moisture and precipitation data provided by the Australian Water Availability Project (AWAP, http://www.csiro.au/awap) (Raupach et al., 2009; Raupach et al., 2018) are of 0.05°×0.05° spatial resolution.

2.2.4 Ocean-atmosphere indices

Two ocean-atmosphere climate indices, the Southern Oscillation Index (SOI) (Ropelewski and Jones, 1987; Allan et al., 1991; Können et al., 1998) available from https://www.esrl.noaa.gov/psd/gcos_wgsp/Timeseries/SOI/ and the Indian Ocean Dipole Mode Index (DMI) (Saji, 2003) available from https://www.esrl.noaa.gov/psd/gcos_wgsp/Timeseries/DMI/ are applied in this study to examine the role of ENSO and IOD in Australia's hydroclimatic variations (Verdon-Kidd and Kiem, 2009a, 2009b; Kiem and Verdon-Kidd, 2010; Van Dijk et al., 2013;).

2.2.5 Empirical orthogonal functions (EOFs)

The EOFs decompose a space-time field into spatial patterns and associated temporal signals. For a continuous space-time field $X(t, s)$, t and s denote respectively time and spatial position, the decomposition is described as in the study of Hannachi et al. (2007):

$$X(t,s) = \sum_{k=1}^{K} c_k(t) u_k(s) \quad (2\text{-}1)$$

where K is the number of modes included in the field, using an optimal set of basic functions of space $u_k(s)$ and expansion functions of time $c_k(t)$. For the space-time field of TWS over Australia, the EOFs method finds a set of orthogonal spatial patterns (EOF_k) along with a set of associated uncorrelated time series or principal components (PC_k) (i.e., PC1 corresponds to EOF1 and so on). This method also provides the explained variance, which indicates how much variability of TWS is explained by each decomposed mode (EOF_k/PC_k).

2.2.6 Significance test

The significance of a linear trend is tested by the modified Mann-Kendall (M-K) test (Hamed and Ramachandra Rao, 1998). Analysis of covariance is applied to test the significance of difference between two time series. The effective sample size (Bretherton et al., 1999) considering the autocorrelation of datasets is applied in statistical significance testing for the correlation coefficient between two time series. The 0.05 significance level is adopted in this study.

2.3 Results and Discussion

2.3.1 Main spatial patterns of TWS variation in Australia

The space-time fields of monthly Australia TWS anomaly from three datasets (14-year original JPL GRACE TWS and reconstructed GRACE TWS of 31 and 114 years) have been decomposed by empirical orthogonal functions (EOFs). We focus on the first two modes since they explain more than 50% of the total variance. The three datasets exhibit similar spatial patterns (Figure 2.1). Almost all grid cells (more than 90%) show consistent phase in terms of spatial pattern EOF1 (Figures 2.1 (a), (c), and (e)) indicating that the wet and dry alternation has consistency over the whole continent, although the north and east parts have higher variability. This EOF mode explains more than 30% of the total TWS variability in Australia. The spatial pattern EOF2 clearly delineates two zones, eastern and western Australia, with opposite behaviour (Figures 2.1 (b), (d), and (f)). This mode is defined as an east-west opposite pattern, which explains around 20% of the total variation of the TWS anomaly in Australia. The dashed line in Figure 2. 1 is drawn based on the average results from the three datasets of different year ranges. This line is coincident with the boundary of the western plateaus and central plains of the Australian continent.

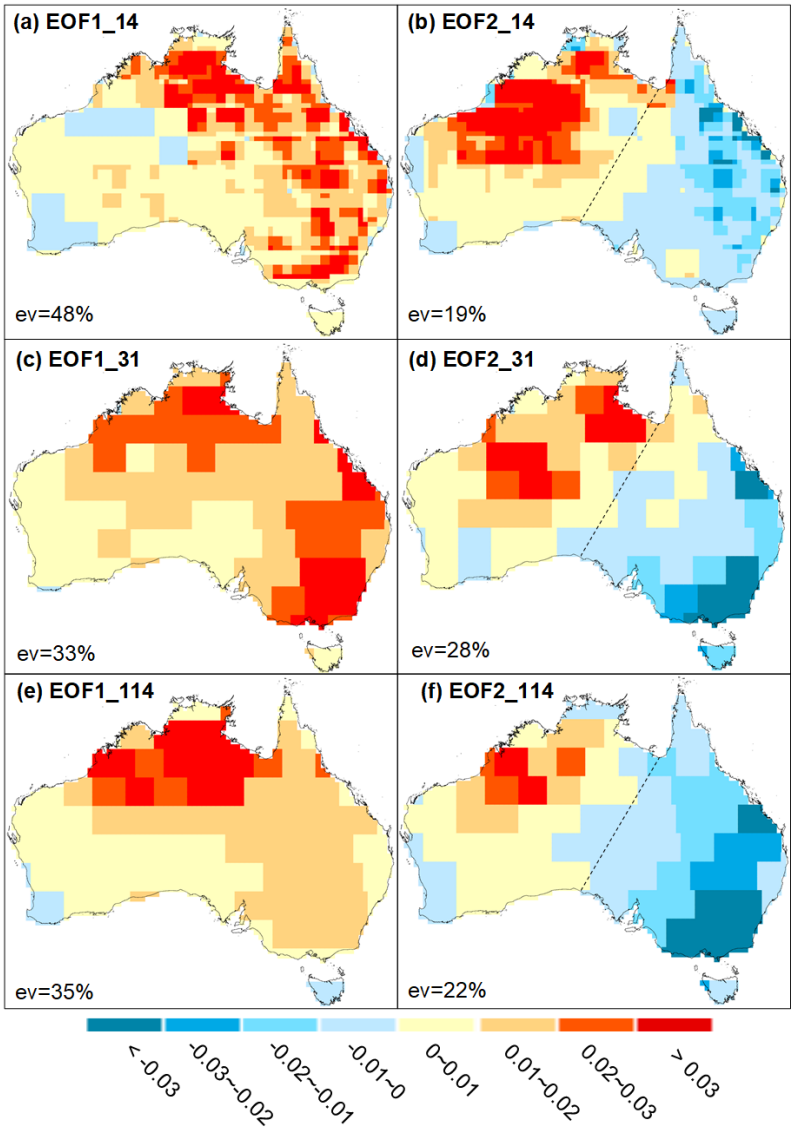

Figure 2.1 Spatial pattern of the first two modes (EOF1 & EOF2) of Australia TWS variation. (a and b) 14-year original JPL GRACE TWS (2003–2016), (c and d) 31-year reconstructed GRACE TWS (1985–2015), (e and f) 114-year reconstructed GRACE TWS (1901–2014). Acronym "ev" stands for explained variance. An east-west opposite (EOF2) pattern is observed in all three datasets.

2.3.2 Four consecutive seesaw wetting and drying phases between eastern and western Australia in the past five decades

The temporal signal of the first decomposed mode (PC1) reflects the wet (positive PC1) and dry (negative PC1) conditions in terms of average TWS anomaly over the whole continent. The continent-wide wetting and drying are closely related to large-scale ocean-atmosphere dynamics. As shown in Figure 2.2, continent-wide wetting episodes represented by positive phases of PC1 generally correspond to positive phases of SOI (La Niña episodes). We use pairs of dashed lines to mark the La Niña induced continent-wide wetting episodes, which are bounded by the time points

when average TWS anomaly in Australia starts to increase, triggered by strong La Niña, and when it returns to equilibrium. Nine La Niña induced continent-wide wetting episodes are identified during 1901–2014 (W1: December 1903–January 1905, W2: March 1910–February 1911, W3: November 1916–November 1918, W4: December 1949–November 1951, W5: February 1956–December 1957, W6: July 1973–March 1980, W7: April 1989–September 1989, W8: August 1998–June 2002, W9: April 2010–January 2013, see Figure 2.2 (a)). As this 114-year reconstructed GRACE TWS data set is the mean of 100 ensemble members, uncertainty in PC1 is quantified by ±1 standard deviation of 100 PC1 time series derived from the ensemble members (Figure 2.2 (a)).

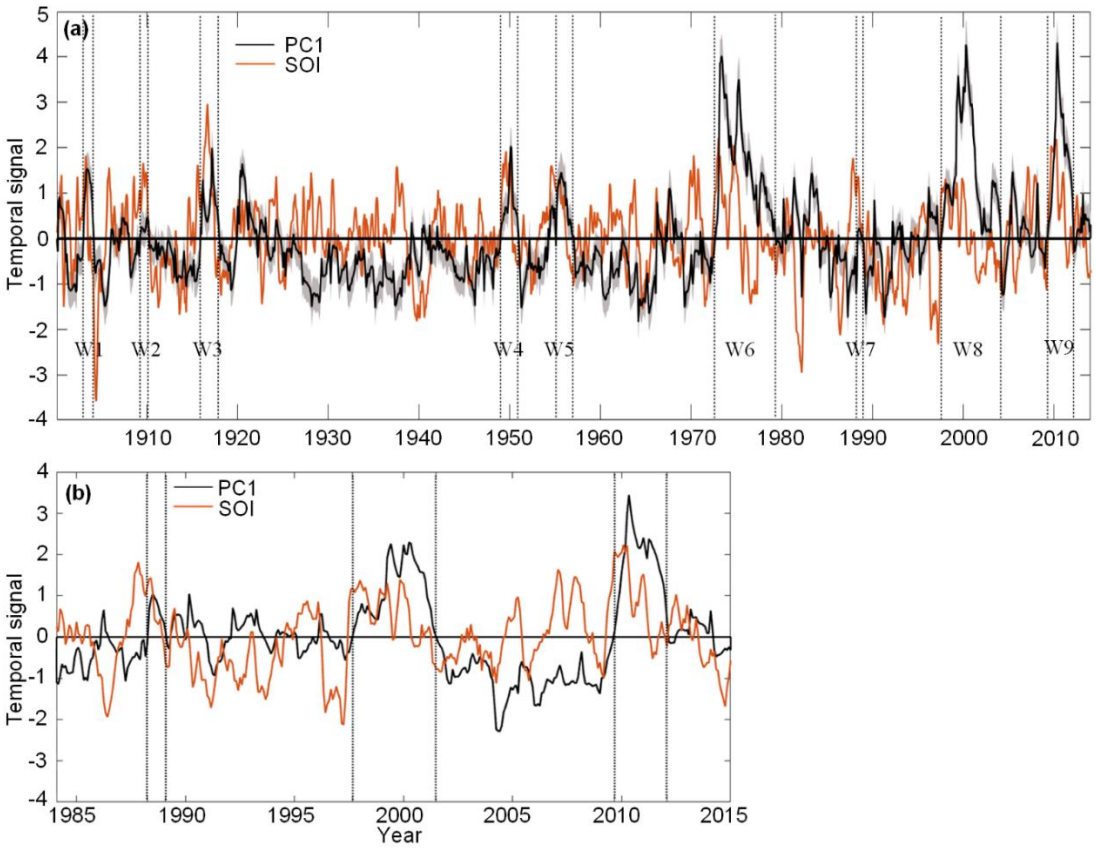

Figure 2.2 La Niña induced continent-wide wetting episodes identified based on standardized SOI and the temporal signal of the first mode (PC1) of Australia TWS variation. (a) PC1 versus SOI during 1901–2014 ($r = 0.18$, $p < 0.05$). The black curve indicates mean PC1 derived from 100 PC1 members and the shaded areas represent ±1 standard deviation of 100 PC1 time series derived from the ensemble members. A 3-month moving average was applied to SOI for readability (orange curve). The periods marked by a pair of dashed lines (W1–W9) denote the La Niña (positive SOI) induced continent-wide wetting episodes (positive PC1). (b) PC1 versus SOI during 1985–2015 ($r = 0.23$, $p < 0.05$). The three marked La Niña induced continent-wide wetting episodes respectively correspond to W7, W8, and W9 shown in (a).

As the eastern and western parts of Australia have opposite phases in EOF2 (Figures 2.1 (b), (d), and (f)), they are supposed to behave oppositely in terms of TWS variation. The periods in-between the La Niña induced continent-wide wetting episodes, show piece-wise linear trends of the regional average TWS anomaly in the eastern and western parts of Australia (Figure 2.3 (a)). Four consecutive opposite TWS trends between eastern and western Australia are observed during the past five decades (1958–2010). In those four consecutive interval periods, changes of regional average TWS anomaly between the two parts are significantly different at 0.05 significance level (tested by analysis of covariance). This phenomenon is identified as seesaw wetting and drying between these two geographical parts of Australia. The seesaw is characterized by eastern Australia gaining (losing) water, while the west is losing (gaining) water. It appears that a seesaw is reset by a continent-wide wetting episode, leading to a previous gaining (losing)-water side starts to lose (gain) water. Another seesaw phenomenon is observed during the 1910s. These five seesaw periods last for 11 ± 5 years. Uncertainty in regional average TWS time series is represented by the shaded area in Figure 2.3 (a). Uncertainty of the consecutive opposite trends in the last four interval periods is quantified in Figure 2.3 (b), the average linear trends of the east and west part derived from 100 ensemble members are significantly different at 0.05 significance level.

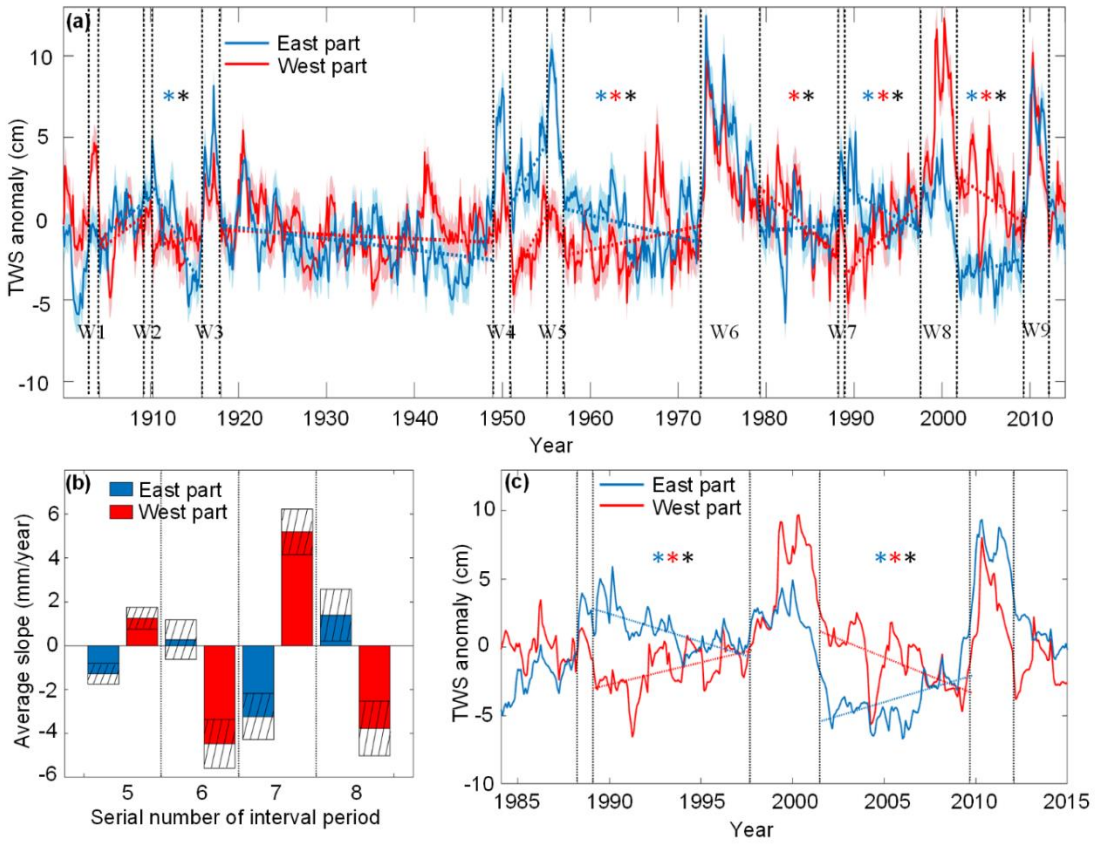

Figure 2.3 TWS seesaw between eastern and western Australia. (a) Regional average TWS anomaly of eastern and western Australia during 1901–2014 (the boundary of eastern and western parts is shown in Figure 2. 1). Blue (red) asterisk (*) indicates the trend of eastern (western) Australia is significant at 0.05 significance level, and the black asterisk indicates the changes of regional average TWS anomaly between eastern and western Australia are significantly different; (b) slopes of regional average TWS anomaly derived from 100 ensemble members in the last four interval periods (5–8). Hatched bars indicate uncertainty (±1 standard deviation) in trends. (c) Same as (a) but based on TWS data of 1985–2015.

The input data for reconstructing the 31- and 114-year TWS include precipitation and temperature information. Data of those two climate variables are of low quality for most of the 114-year time series. Therefore, we repeated above analysis with the 31-year reconstructed TWS data (1985–2015) for comparison. Three La Niña induced continent-wide wetting episodes (April 1989–January 1990, August 1998–June 2002, and August 2010–February 2013) are marked in Figure 2.2 (b), which respectively correspond to W7–W9 shown in Figure 2.2 (a), although minor differences exist. The regional average TWS anomaly of the eastern and western parts of Australia from 1985 to 2015 are plotted in Figure 2.3 (c). Two pairs of opposite trends (all are significant at 0.05

significance level) are observed in the interval periods which correspond to the last two seesaws shown in Figure 2.3 (a), respectively.

No seesaw phenomenon is observed if the interval between two La Niña induced continent-wide wetting episodes is too short (1905–1910) or too long (1918–1949). The length of a continent-wide wetting episode (reflected in the PC1 response, Figure 2.2) and its occurrence frequency are associated with the intensity and duration of the La Niña events, as well as the conjunction effects from other oscillations (e.g., IPO and IOD). From 1918 to 1949, only one moderate La Niña occurred (1938–1939), but it did not induce continent-wide wetting (Figure 2.2 (a)). This was likely because a positive IPO phase dominated during 1922–1944 (Salinger et al., 2001), which suppressed both the occurrence and magnitude of a La Niña event (Gershunov and Barnett, 1998; Power et al., 1999; Folland et al., 2002; Kiem et al., 2003; Franks, 2004; Kiem and Franks, 2004; Guan et al., 2005; Cai and van Rensch, 2012; King et al., 2013). The wetting episode W7 was short (10 months), which was likely relevant to the positive IPO phase (1978–1998) (Salinger et al., 2001). Different from the situation in the previous positive IPO (1922–1944), the La Niña in W7 was strong enough to lead to a continent-wide wetting and reset the seesaw between eastern and western Australia. Here, the La Niña coincident with a negative IOD (Figure 2.4) could explain this situation. Negative IOD usually enhances the La Niña effect, it can also lead to a wetter than normal condition in western and southern Australia (Risbey et al., 2009; Cai et al., 2014).

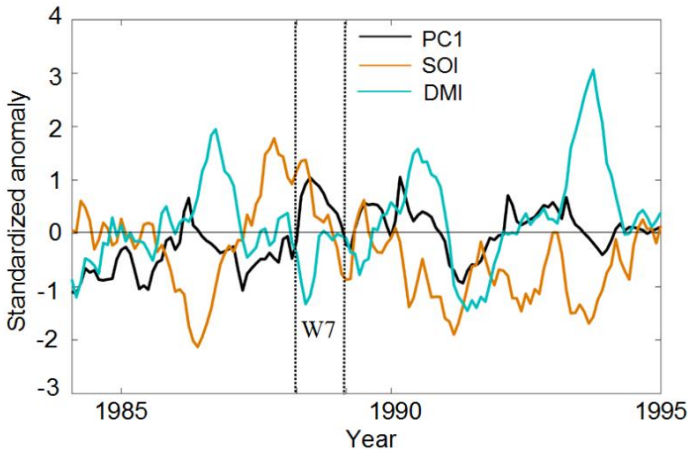

Figure 2.4 Monthly time series of GRACE TWS PC1, SOI and DMI from 1985 to 1995.

2.3.3 Independent evidence for TWS seesaw between eastern and western Australia

A soil moisture data set for 1901–2014 (provided by AWAP) also shows a seesaw pattern (Figure 2.5) consistent with that of TWS shown in Figure 2.3 (a). The agreement between the results

based on two independent data sources supports the validity of the TWS seesaw between the two parts of Australia, because changes in soil moisture are typically the largest component of TWS variation (Rodell and Famiglietti, 2001).

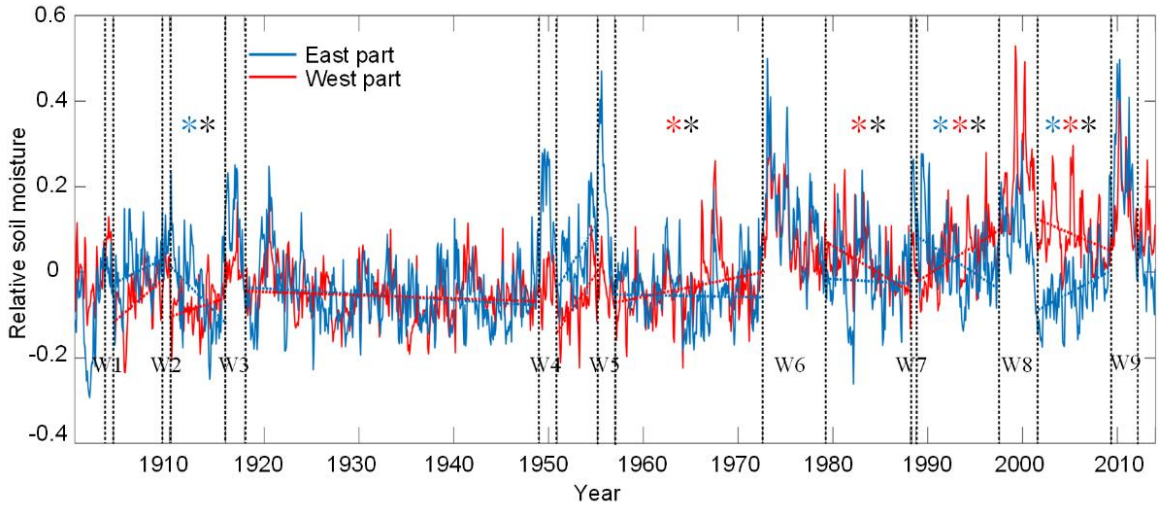

Figure 2.5 Regional average soil moisture of eastern and western Australia during 1901–2014, which shows a similar seesaw pattern to TWS (changes of regional average soil moisture between eastern and western Australia are significantly different in five interval periods: Mar 1911–Oct 1916, Jan 1958–Jun 1973, Apr 1980–Mar 1989, Oct 1989–Jul 1998 and Aug 2002–Mar 2010.

In addition, as ecosystems are mostly water limited in Australia, changes of TWS should have led to and be reflected in vegetation responses. GIMMS NDVI data set provides an opportunity to verify the most recent two TWS seesaw phenomena (February 1990–July 1998 and July 2002–July 2010, following the intervals identified based on 31-year reconstructed TWS data). Linear NDVI trends during those two seesaws at each grid cell are shown in Figures 2.6 (a) and (b) respectively. A marked east-west difference in NDVI trends is observed for both periods. During February 1990–July 1998, NDVI anomaly increases in the western region and decreases in the eastern region of Australia (Figure 2.6 (a)), which is consistent with TWS wetting in the west and drying in the east (Figure 2.3 (c)). During July 2002–July 2010, NDVI anomaly (Figure 2.6 (b)) also shows consistent trends with TWS (Figure 2.3 (c)). Similar to Figure 2.3 (c), we plot the regional average NDVI anomaly of eastern and western Australia from 1985 to 2015 in Figure 2.6 (c). During the interval between W7 and W8, the regional average NDVI anomaly significantly increases in the west and slightly decreases in the east. During the interval between W8 and W9, average NDVI anomaly significantly increases in the east and slightly decreases in the west. Changes of regional average NDVI anomaly between the two parts are significantly different in both interval periods (Figure 2.6 (c)). These NDVI

seesaws, consistent with those of TWS ones, between the western and eastern parts of Australia, provide strong support for the seesaw pattern of TWS variation in Australia.

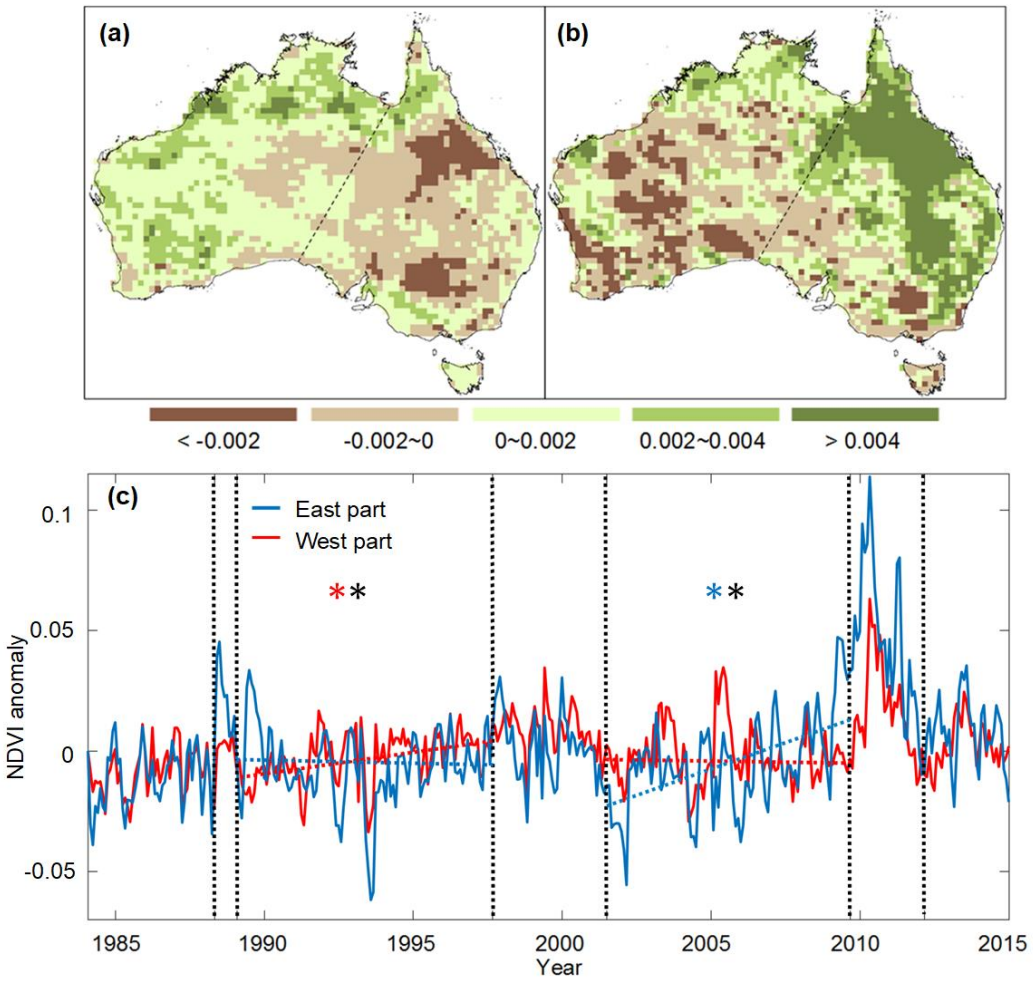

Figure 2.6 Seesaw phenomenon of NDVI during 1985–2015. (a and b) Linear trends (per month) of NDVI during two interval periods (February 1990–July 1998 and July 2002–July 2010); (c) same as Figure 2.3 (c) but for NDVI anomaly.

2.3.4 Possible mechanism of the Australia TWS seesaw phenomenon

For the four consecutive TWS seesaws between eastern and western Australia, the seesaw state seems to be reset by a continent-wide wetting episode. In other words, if a region was gaining water before the wetting episode, it would be losing water after that. Since TWS is mainly recharged by precipitation, we attempted to explain the seesaw phenomenon of TWS by looking into precipitation patterns. The regional average precipitation (provided by AWAP) in the eastern and western parts of Australia during 1901–2014 is plotted in Figure 2.7 (a). Opposite trends between two parts are shown for the last three intervals. After the regional average precipitation time series being smoothed, those three pairs of opposite trends are significantly different in each interval

(Figure 2.7 (b)). It appears that precipitation alone cannot explain the TWS seesaw because in the second (between W2 and W3) and fifth (between W5 and W6) interval periods the seesaw phenomenon is only observed in TWS but not in precipitation.

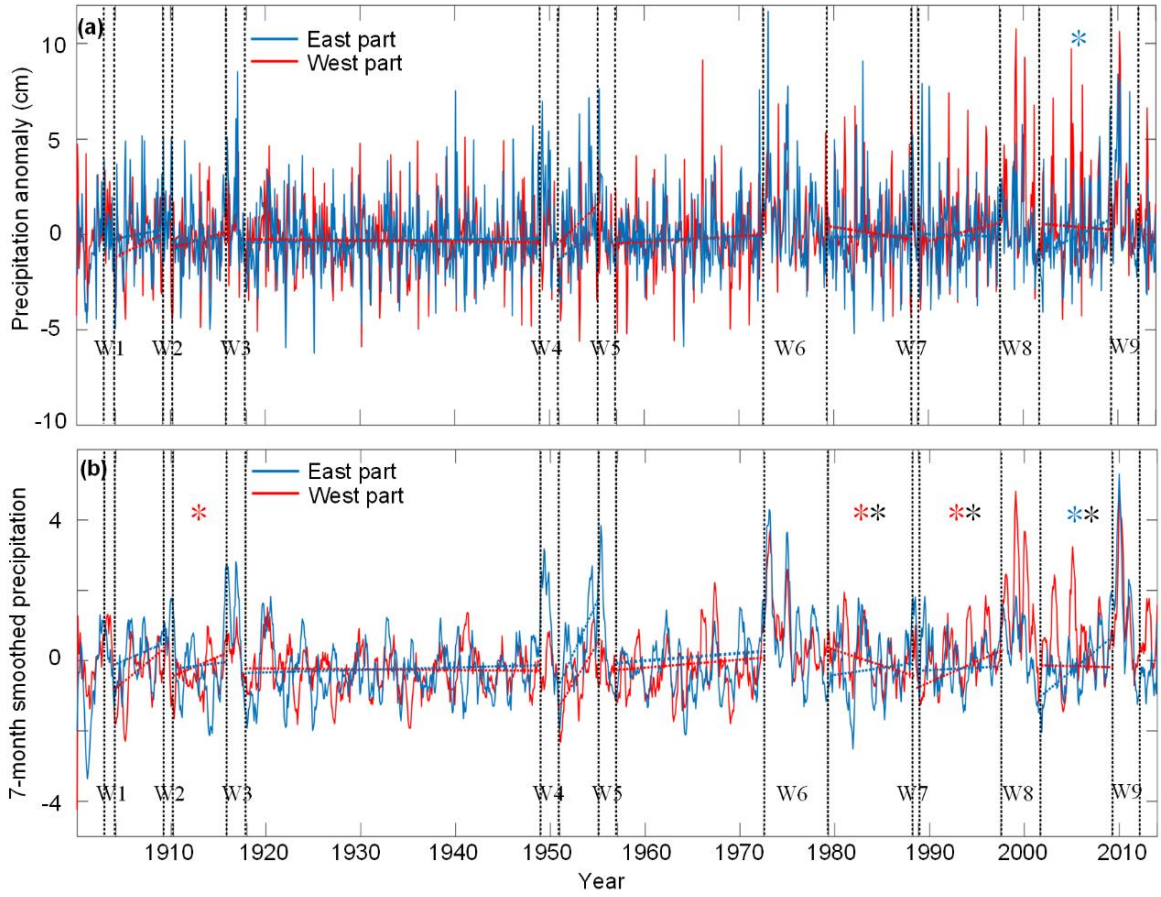

Figure 2.7 (a) Regional average precipitation of eastern and western Australia during 1901–2014, opposite trends are observed in the last three interval periods, but no significant difference of changes in regional average precipitation anomaly between eastern and western Australia is observed in any interval period. (b) same as (a) but for 7-month smoothed precipitation, opposite trends in the last three intervals are significantly different.

Here, we provide one possible mechanism related to dynamic woody vegetation and soil moisture interactions, which appears to explain the seesaw resetting pattern (Figure 2.8). For a region with an increasing TWS (the lower blue arrow in Figure 2.8) during a seesaw period, vegetation cover tends to be well developed prior to a wetting episode. Such an improved vegetation cover makes the region to have a larger than normal storm water retention capacity for big wetting events, for example, by root enhanced infiltration and organic matter facilitated soil hydrophilicity (Lange et al., 2009; Guan et al., 2010; Wang et al., 2013). Following the wetting

episode, this increasing vegetation cover tends to demand more root water uptake, which gradually depletes soil moisture, and thus TWS (the upper blue arrow in Figure 2.8). This process reverses the previous positive TWS trend to a negative one.

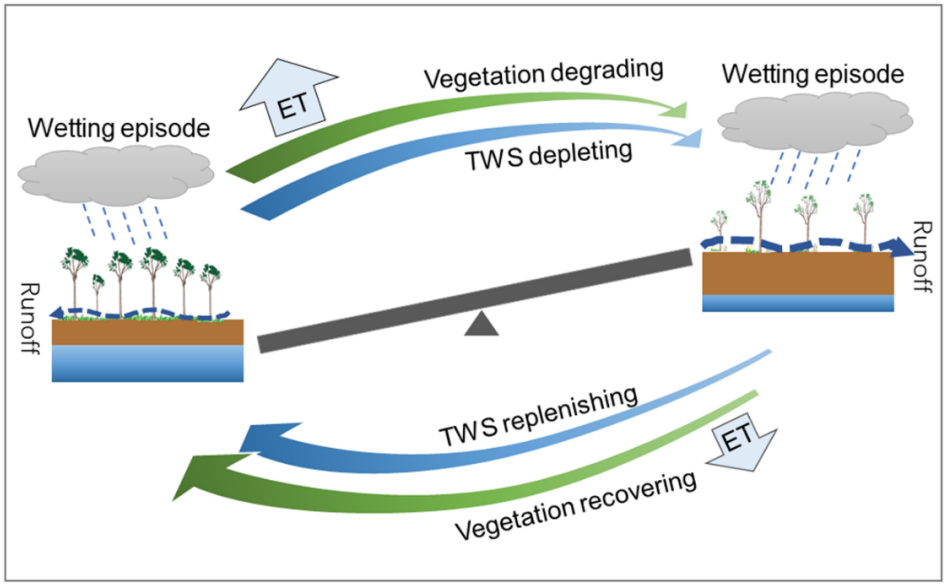

Figure 3.8 A schematic showing possible terrestrial water storage and vegetation interactions, leading to TWS seesaw and its resetting by big wetting episodes.

In contrast, for a region with a decreasing TWS (the upper blue arrow in Figure 2.8) during a seesaw period, vegetation cover will reduce. Such a surface tends to favour runoff generation and soil erosion, leading to a lower storm water retention (Dunjó et al., 2004; Kothyari et al., 2004; Mohammad and Adam, 2010). Since Australia is prone to wildfires, the storm water retention can be further weakened by fire-induced hydrophobic soils (Mataix-Solera et al., 2011). After the wetting episode, the previously reduced vegetation cover demands less soil moisture, leading to a gradual increase of TWS (the lower blue arrow in Figure 2.8) during the interval period.

The above two situations explain the seesaw resetting pattern in which a positive (negative) seesaw stage is reset to a negative (positive) one after a short wetting episode. This mechanism highlights the important role of vegetation and soil moisture interactions in the observed TWS seesaws. The possibility of this vegetation mediation for the seesaw phenomenon is further supported by comparing spatial patterns of linear trends of relevant variables. The spatial pattern of TWS trends (Figures 2.9 (a) and (b)) matches better with that of NDVI (Figures 2.6 (a) and (b)) than that of precipitation (Figures 2.9 (c) and (d)), suggesting that the vegetation mediation effect is very likely the primary influence on the TWS seesaw phenomenon. The mechanism of vegetation

recovering (degrading) illustrated in Figure 2.8 can be enhanced by in-phase trends of precipitation. For example, in the last three interval periods precipitation shows opposite trends between the eastern and western parts of Australia, which are consistent with those of TWS.

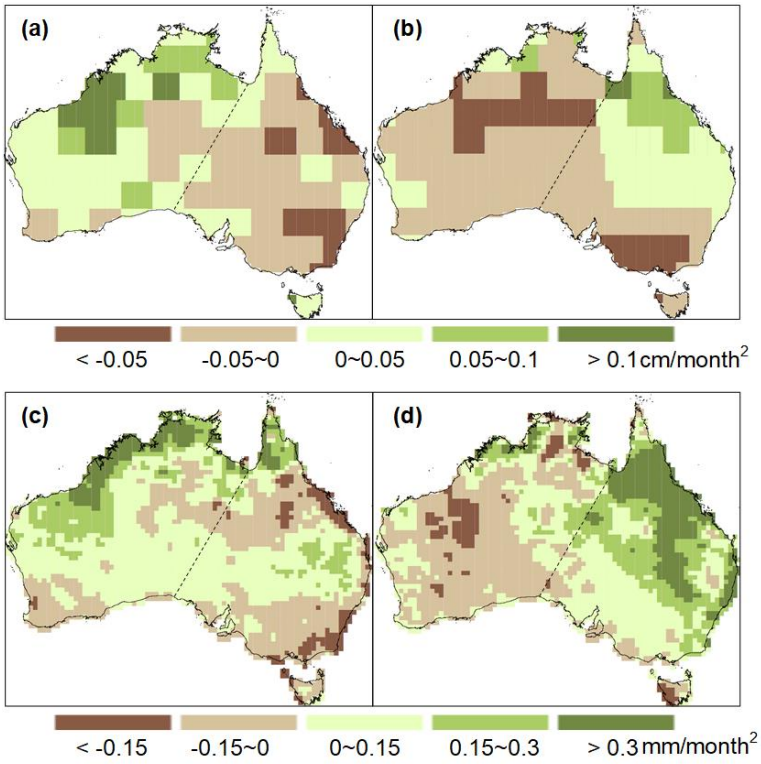

Figure 2.9 Same as Figure 2.6 (a–b) but for TWS (a–b) and precipitation (c–d) respectively.

By comparing the 12-month average NDVI anomaly immediately before (Figures 2.10 (a–c) and 12-month average TWS anomaly immediately after (Figures 2.10 (d–f) the three La Niña induced continent-wide wetting episodes shown in Figure 2.2 (b), we can see that the half of the continent (either east or west) with increased vegetation cover (positive NDVI anomaly) prior to a La Niña triggered wetting episode, retains larger than normal storm water (positive TWS anomaly) after the episode. After a wetting episode, the part dominated by positive NDVI and TWS anomalies experiences a decreasing evapotranspiration (ET) (Figures 2.10 (g) and (h)), reflecting a gradually decreasing vegetation cover resulting from a depleting TWS. These processes are consistent with the trends of NDVI and TWS during the corresponding interval period. In addition, vegetation in the region with positive (negative) NDVI anomaly prior to the last La Niña induced continent-wide wetting shows a decreasing (increasing) trend during March 2013–December 2018 (Figure 2.11). Such results support the mechanism of the TWS seesaw phenomenon for Australia, which we explained in Figure 2.8.

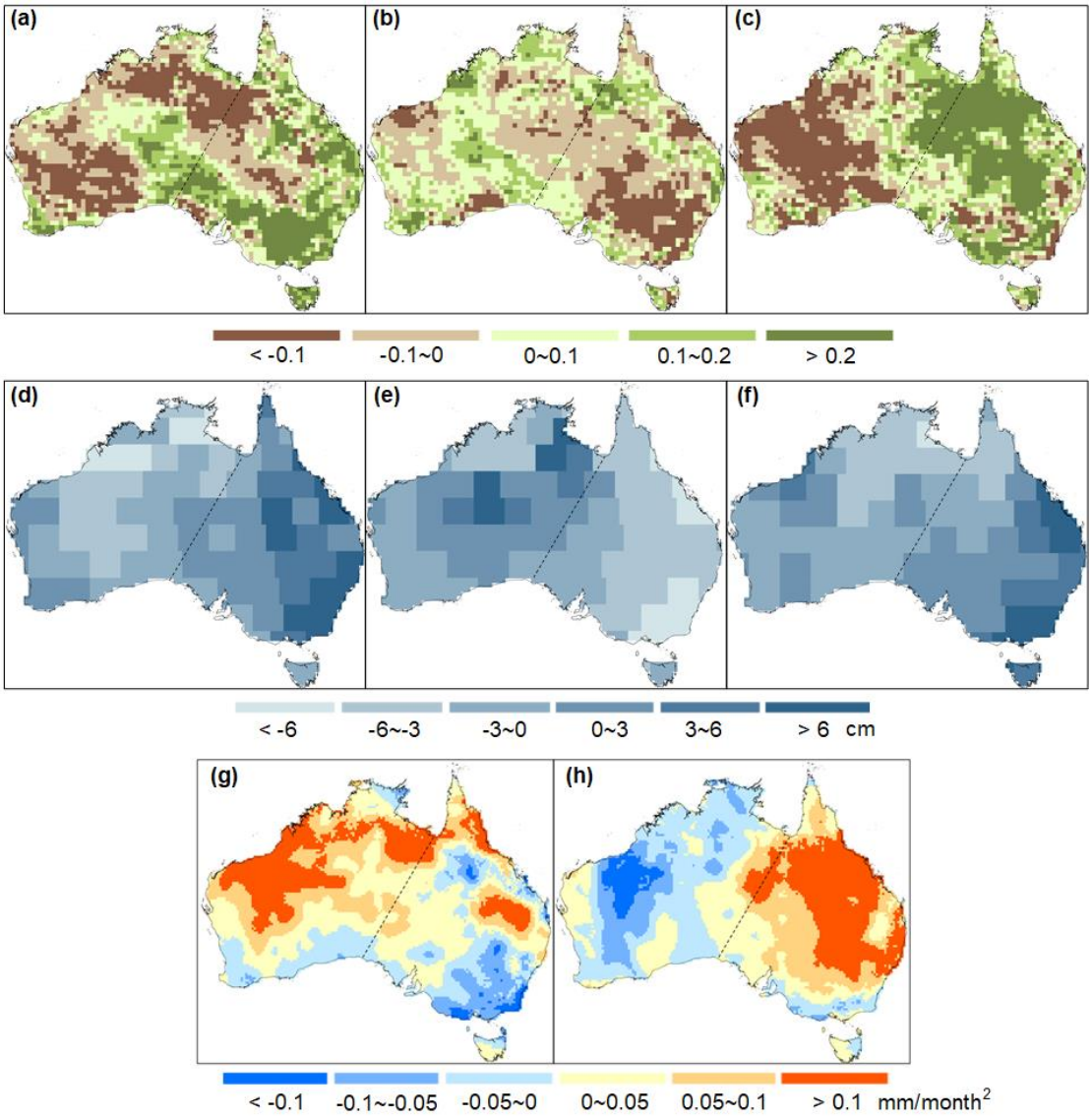

Figure 2.10 Evidence for the possible mechanism of the TWS seesaw phenomenon. Average 12-month NDVI anomaly (a–c) immediately before and average 12-month TWS anomaly (d–f) immediately after the three continent-wide wetting episodes: April 1989–January 1990, August 1998–June 2002, and August 2010–February 2013; (g and h) linear trends of evapotranspiration (ET) during two interval periods: February 1990–July 1998 and July 2002–July 2010.

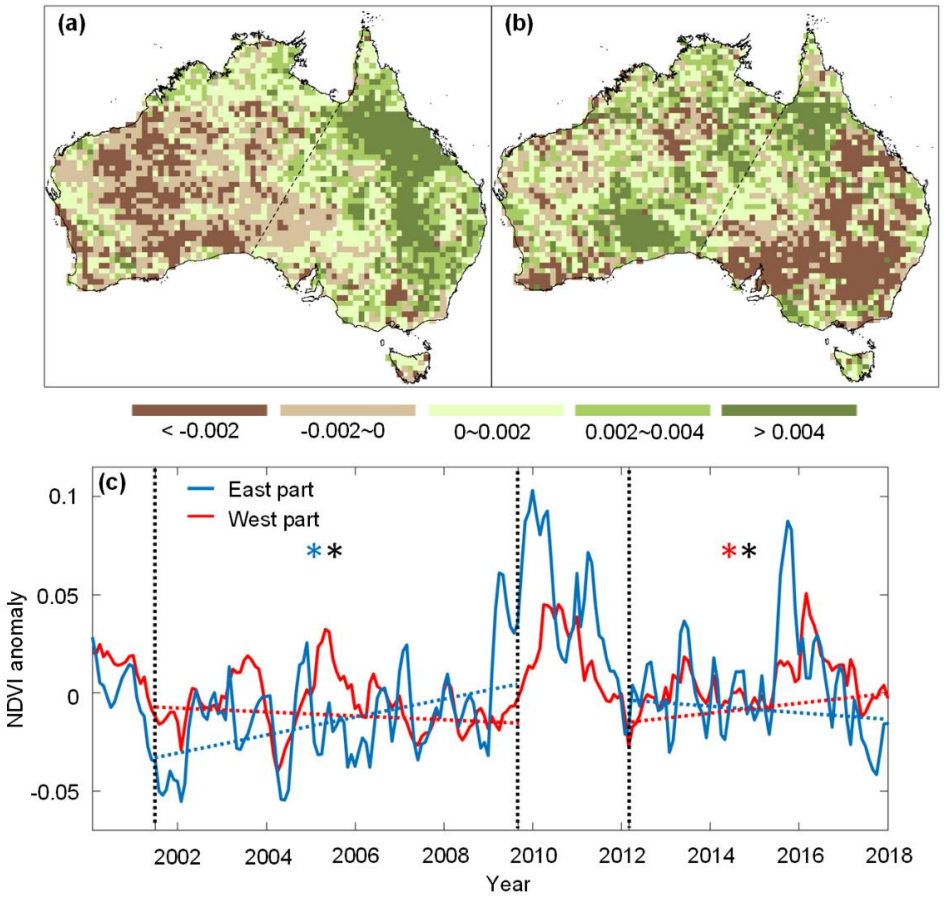

Figure 2.11 (a–b) Linear trends (per month) of MODIS NDVI during Jul 2002–Jul 2010 and Mar 2013–Dec 2018; (c) regional average NDVI anomaly of eastern and western Australia during 2001–2018. Results from GIMMS (Figure 2.6) and MODIS NDVI datasets are consistent during the overlapped interval Jul 2002–Jul 2010. Opposite linear trends between the two parts are also observed during Mar 2013–Dec 2018. Changes of regional average MODIS NDVI anomaly between eastern and western Australia are significantly different in both interval periods.

Based on this understanding, we suppose that vegetation dynamic, in response to continent-wide wetting, plays an important role in the TWS seesaw in Australia. However, the interval period should be long enough for woody vegetation to recover in one part while to degrade in the other part of Australia, so that TWS seesaw between the two parts could be reset by a La Niña induced continent-wide wetting.

2.3.5 Soil-vegetation-atmosphere transfer of the seesaw phenomenon

The soil-plant-atmosphere continuum (SPAC) describes the water transfer from soil, root, stem, and leaf to the atmosphere. As the results shown above that the seesaw phenomenon are observed in TWS and NDVI, the seesaw pattern is expected to be transferred through the SPAC from

soil and plant to the atmosphere. Here, the analysis performed on NDVI as shown in Figure 2.6 is also applied on land surface temperature (Ts), vapor pressure deficit (VPD), and global primary productivity (GPP). Maps of the linear trend of those three variables at each grid cell are shown in Figure 2.12, and their regional averages are plotted in Figure 2.13. Seesaw patterns are observed in all the three variables as expected. Such results may help to reduce uncertainties in current projections of future terrestrial carbon fluxes.

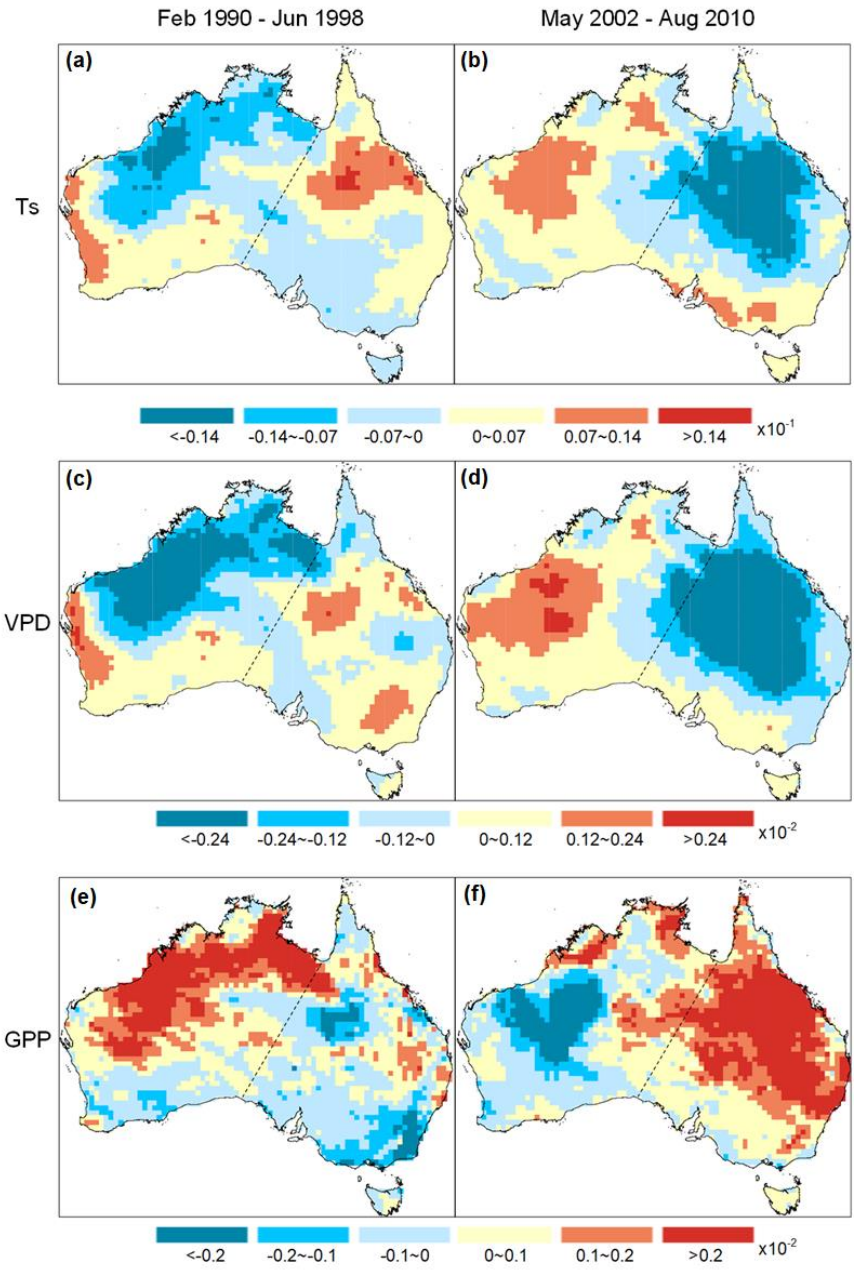

Figure 2.12 Spatial patterns for linear trends of (a–b) land surface temperature (Ts), (c–d) vapor pressure deficit (VPD), and (e–f) global primary productivity (GPP) during Feb 1990–Jun 1998 (the first column) and May 2002–Aug 2010 (the second column), respectively.

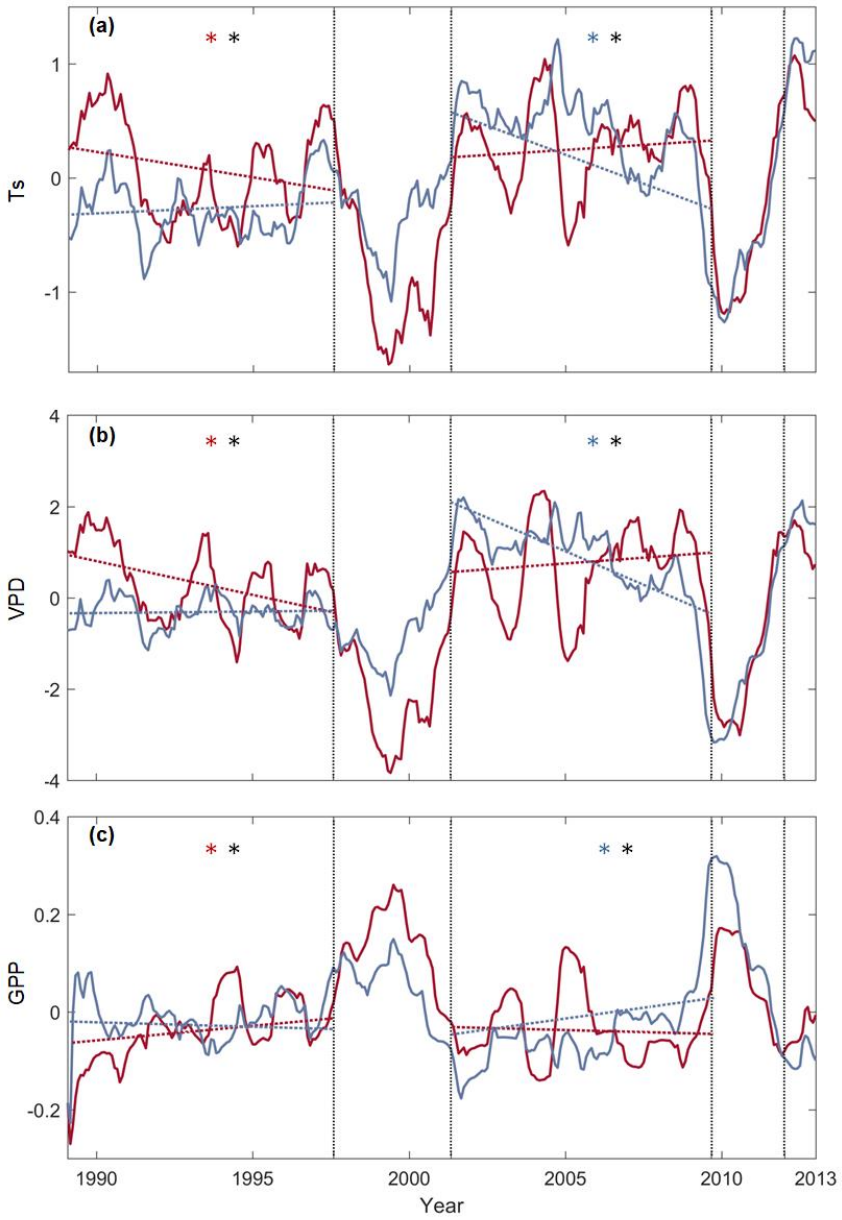

Figure 2.13 Plots of regional average (a) Ts, (b) VPD, and (c) GPP for the two intervals. Blue (red) asterisk (*) indicates the trend of eastern (western) Australia is significant at 0.05 significance level, and the black asterisk indicates the changes of regional average TWS anomaly between eastern and western Australia are significantly different.

2.4 Conclusions

This study, based on three TWS datasets (14-year original JPL GRACE TWS and 31- and 114-year reconstructed GRACE TWS), elucidates a new spatio-temporal pattern of wetting-drying over Australia. Four consecutive seesaw wetting and drying phases between eastern and western Australia are observed in the past five decades, which is characterized by eastern Australia gaining water while the western part is losing water, and vice versa. Strong La Niña induced continent-wide

wetting, resets this pattern, leaving each seesaw to last for 11 ± 5 years. The TWS seesaw phenomenon is substantiated by a similar pattern in NDVI between eastern and western Australia during February 1990–July 1998 and July 2002–July 2010. This continental scale TWS seesaw pattern seems to be resulting from woody vegetation response to climate variability and its feedback on hydrological processes. In addition, similar pattern is also observed in Ts, VPD and GPP, which implies the transfer of the seesaw pattern from soil and plant to the atmosphere through the soil-plant-atmosphere continuum.

The results of this study contribute to a better understanding of drying and wetting phases and hence can stimulate an adaptive forest, water, and disaster risk management in the wake of a strong La Niña induced continent-wide wetting in Australia. Our finding suggests that at the end of a seesaw drying phase, poor vegetation cover limits the landscape water retention capacity. Hence, during a drying phase a reasonable management response might be to increase storm water harvesting capacity. At the beginning of a seesaw drying phase, previously increased vegetation cover (resulting from a previous seesaw wetting) depletes root zone moisture, leading to landscape degradation in the subsequent years. Reducing vegetation cover right after the wetting episode might reduce the risk of heatwaves and bushfires in the later dry stage.

2.5 References

Ahlström, A., Raupach, M. R., Schurgers, G., Smith, B., Arneth, A., Jung, M., et al. 2015. The dominant role of semi-arid ecosystems in the trend and variability of the land CO_2 sink. Science, 348, 895–899.

Allan, R. J., Nicholls, N., Jones, P. D., Butterworth, I. J. 1991. A further extension of the Tahiti-Darwin SOI, early ENSO events and Darwin pressure. Journal of Climate, 4, 743–749.

Andrew, R., Guan, H., Batelaan, O. 2017. Estimation of GRACE water storage components by temporal decomposition. Journal of Hydrology, 552, 341–350.

Beaudoing, H. and Rodell, M., NASA/GSFC/HSL. 2015. GLDAS Noah Land Surface Model L4 monthly 0.25 × 0.25 degree, V2.0, Greenbelt, Maryland, USA, Goddard Earth Sciences Data and Information Services Centre (GES DISC).

Bretherton, C. S., Widmann, M., Dymnikov, V. P., Wallace, J. M., Bladé, I. 1999. The effective number of spatial degrees of freedom of a time-varying field. Journal of Climate, 12(7), 1990–2009.

Cai, W., Purich, A., Cowan, T., van Rensch, P., Weller, E. 2014. Did climate change-induced rainfall trends contribute to the Australian millennium drought? Journal of Climate, 27, 3145–3168.

Cai, W., and van Rensch, P. 2012. The 2011 southeast Queensland extreme summer rainfall: A confirmation of a negative Pacific Decadal Oscillation phase? Geophysical Research Letters, 39, L08702.

Cai, W. van Rensch, P., Cowan, T., Hendon, H. H. 2011. Teleconnection pathways of ENSO and the IOD and the mechanisms for impacts on Australian rainfall. Journal of Climate, 24, 3910–3923.

Christidis, N., Stott, P. A., Karoly, D. J., Ciavarella, A. 2013. An attribution study of the heavy rainfall over Eastern Australia in March 2012. Bulletin of the American Meteorological Society, 94(9), S58–S61.

Dey, R., Lewis, S. C., Arblaster, J. M. Abram, N. J. 2019. A review of past and projected changes in Australia's rainfall. WIREs Climate Change, 10, e577.

Didan, K., Barreto Munoz, A., Solano, R., Huete, A. 2015. MODIS vegetation index users guide.

Dunjó, G., Pardini, G., Gispert, M. 2004. The role of land use-land cover on runoff generation and sediment yield at a microplot scale, in a small Mediterranean catchment. Journal of Arid Environments, 57(2), 239–256.

Evans, J. P. and Boyer-Souchet, I. 2012. Local sea surface temperatures add to extreme precipitation in northeast Australia during La Niña. Geophysical Research Letters, 39, L10803.

Folland, C. K., Renwick, J. A., Salinger, M. J., Mullan, A. B. 2002. Relative influences of the Interdecadal Pacific Oscillation and ENSO on the South Pacific Convergence Zone. Geophysical Research Letters, 29(13), 1643.

Franks, S. W. 2004. Multi-decadal climate variability, New South Wales, Australia. Water Science and Technology, 49(7), 133–140.

Gershunov, A. and Barnett, T. P. 1998. Interdecadal modulation of ENSO teleconnections. Bulletin of the American Meteorological Society, 79, 2715–2725.

Guan, H., Simunek, J., Newman, B. D., Wilson, J. L. 2010. Modelling investigation of water partitioning at a semiarid ponderosa pine hillslope. Hydrological Processes, 24, 1095–1105.

Guan, H., Vivoni, E. R., Wilson, J. L. 2005. Effects of atmospheric teleconnections on seasonal precipitation in mountainous regions of the southwestern U.S. A case study in northern New Mexico. Geophysical Research Letters, 32, L23701.

Hamed, K.H. and Ramachandra Rao, A. 1998. A modified Mann-Kendall trend test for autocorrelated data. Journal of Hydrology, 204, 182–196.

Hannachi, A., Jolliffe, I. T., Stephenson, D. B. 2007. Empirical orthogonal functions and related techniques in atmospheric science: A review. International Journal of Climatology, 27(9), 1119–1152.

Heberger, M. 2012. Australia's Millennium Drought: Impacts and responses. In P. H. Gleick (Ed.), The World’s Water (pp. 97–125). Island Press.

Herold, N., Kala, J., Alexander, L. V. 2016. The influence of soil moisture deficits on Australian heatwaves. Environmental Research Letters, 11, 064003.

Humphrey, V. and Gudmundsson, L. 2019. GRACE-REC: a reconstruction of climate-driven water storage changes over the last century. Earth System Science Data, 11(3), 1153–1170.

Humphrey, V., Gudmundsson, L., Seneviratne, S. I. 2017. A global reconstruction of climate-driven subdecadal water storage variability. Geophysical Research Letters, 44, 2300–2309.

Johnson, F., White, C. J., van Dijk, A., Ekstrom, M., Evans, J. P., Jakob, D., et al. 2016. Natural hazards in Australia: floods. Climatic Change, 139, 21–35.

Kiem, A.S. and Franks, S.W. 2004. Multi-decadal variability of drought risk, eastern Australia. Hydrological Processes, 18(11), 2039–2050.

Kiem, A. S., Franks, S. W., Kuczera, G. 2003. Multi-decadal variability of flood risk. Geophysical Research Letters, 30(2), 1035.

Kiem, A. S., Johnson, F., Westra, S., Van Dijk, A., Evans, J. P., O'Donnell, A., et al. 2016. Natural hazards in Australia: droughts. Climatic Change, 139, 37–54.

Kiem, A.S. and Verdon-Kidd, D.C. 2010. Towards understanding hydroclimatic change in Victoria, Australia - preliminary insights into the "Big Dry". Hydrology and Earth System Sciences, 14, 433–445.

King, A. D., Alexander, L. V., Donat, M. G. 2013. Asymmetry in the response of eastern Australia extreme rainfall to low-frequency Pacific variability. Geophysical Research Letters, 40(10), 2271–2277.

King, A. D., Lewis, S. C., Perkins, S. E., Alexander, L. V., Donat, M. G., Karoly, D. J., Black, M. T. 2013. Limited evidence of anthropogenic influence on the 2011-12 Extreme Rainfall over Southeast Australia. Bulletin of the American Meteorological Society, 94(9): S55–S58.

King, A. D., Pitman, A. J., Henley, B. J., Ukkola, A. M., Brown, J. R. 2020. The role of climate variability in Australian drought. Nature Climate Change, 10, 177–179.

Können, G. P., Jones, P. D., Kaltofen, M. H., Allan, R. J. 1998. Pre-1866 extensions of the Southern Oscillation Index using early Indonesian and Tahitian meteorological readings. Journal of Climate, 11, 2325–2339.

Kothyari, B. P., Verma, P. K., Joshi, B. K., Kothyari, U. C. 2004. Rainfall-runoff-soil and nutrient loss relationships for plot size areas of bhetagad watershed in Central Himalaya, India. Journal of Hydrology, 293(1-4), 137–150.

Lange, B., Lüescher, P., Germann, P. F. 2009. Significance of tree roots for preferential infiltration in stagnic soils. Hydrology and Earth System Sciences, 13, 1809–1821.

Long, D., Yang, Y., Wada, Y., Hong, Y., Liang, W., Chen, Y., et al. 2015. Deriving scaling factors using a global hydrological model to restore GRACE total water storage changes for China's Yangtze River Basin. Remote Sensing of Environment, 168, 177–193.

Ma, X., Huete, A., Moran, S., Ponce-Campos, G., Eamus, D. 2015. Abrupt shifts in phenology and vegetation productivity under climate extremes. Journal of Geophysical Research: Biogeosciences, 120, 2036–2052.

Mataix-Solera, J., Cerdà, A., Arcenegui, V., Jordán, A., Zavala, L. M. 2011. Fire effects on soil aggregation: A review. Earth-Science Reviews, 109(1-2), 44–60.

Mohammad, A.G. and Adam, M.A. 2010. The impact of vegetative cover type on runoff and soil erosion under different land uses. Catena, 81(2), 97–103.

Nicholls, N. 1992. Historical El Niño/Southern oscillation variability in the Australian region. In H. F. Diaz, & V. Markgraf (Eds.), El Nino, historical and paleoclimatic aspects of the southern oscillation (pp. 151–174). Cambridge Academic Press.

Nicholls, N. 2011. What caused the eastern Australia heavy rains and floods of 2010/11? Bulletin of the Australian Meteorological and Oceanographic Society, 24, 33–34.

Nicholls, N., Drosdowsky, W., Lavery, B. 1997. Australian rainfall variability and change. Weather, 52, 66–72.

Padrón, R. S., Gudmundsson, L., Decharme, B., Ducharne, A., Lawrence, D. M., Mao, J., et al. 2020. Observed changes in dry-season water availability attributed to human-induced climate change. Nature Geoscience, 13, 477–481.

Perkins-Kirkpatrick, S. E., White, C. J., Alexander, L. V., Argüeso, D., Boschat, G., Cowan, T., et al. 2016. Natural hazards in Australia: Heatwaves. Climatic Change, 139, 101–114.

Pinzon, J. and Tucker, C. 2014. A Non-Stationary 1981-2012 AVHRR NDVI3g Time Series. Remote Sensing, 6, 6929–6960.

Poulter, B., Frank, D., Ciais, P., Myneni, R. B., Andela, N., Bi, J., et al. 2014. Contribution of semi-arid ecosystems to interannual variability of the global carbon cycle. Nature, 509, 600–603.

Power, S., Casey, T., Folland, C., Colman, A., Mehta, V. 1999. Inter-decadal modulation of the impact of ENSO on Australia. Climate Dynamics, 15, 319–324.

Power, S., Haylock, M., Colman, R., Wang, X. 2006. The predictability of interdecadal changes in ENSO activity and ENSO teleconnections. Journal of Climate, 19, 4755–4771.

Raupach, M. R., Briggs, P. R., Haverd, V., King, E. A., Paget, M. Trudinger, C. M. 2009. Australian Water Availability Project (AWAP): CSIRO Marine and Atmospheric Research Component: Final Report for Phase 3. CAWCR Technical Report No. 013. p. 67.

Raupach, M. R., Briggs, P. R., Haverd, V., King, E. A., Paget, M., Trudinger, C. M. 2018. Australian Water Availability Project, Data Release 26m. CSIRO Oceans and Atmosphere.

Risbey, J. S., Pook, M. J., McIntosh, P. C., Wheeler, M. C., Hendon, H. H. 2009. On the remote drivers of rainfall variability in Australia. Monthly Weather Review, 137, 3233–3253.

Rodell, M. and Famiglietti, J. S. 2001. An analysis of terrestrial water storage variations in Illinois with implications for the Gravity Recovery and Climate Experiment (GRACE). Water Resources Research, 37(5), 1327–1339.

Rodell, M., Houser, P. R., Jambor, U., Gottschalck, J., Mitchell, K., Meng, C.-J., et al. 2004. The global land data assimilation system. Bulletin of the American Meteorological Society, 85, 381–394.

Ropelewski, C. F. and Jones, P. D. 1987. An extension of the Tahiti-Darwin Southern Oscillation Index. Monthly Weather Review, 115, 2161–2165.

Saji, N. and Yamagata, T. 2003. Possible impacts of Indian Ocean Dipole mode events on global climate. Climate Research, 25(2), 151–169.

Salinger, M. J., Renwick, J. A., Mullan, A. B. 2001. Interdecadal Pacific Oscillation and South Pacific climate. International Journal of Climatology, 21, 1705–1721.

Sharples, J. J., Cary, G. J., Fox-Hughes, P., Mooney, S., Evans, J. P., Fletcher, M.-S., et al. 2016. Natural hazards in Australia: Extreme bushfire. Climatic Change, 139, 85–99.

Trenberth, K. E. 2012. Framing the way to relate climate extremes to climate change. Climatic Change, 115, 283–290.

Tucker, C. J., Pinzon, J. E., Brown, M. E., Slayback, D. A., Pak, E. W., Mahoney, R., et al. 2005. An extended AVHRR 8-km NDVI dataset compatible with MODIS and SPOT vegetation NDVI data. International Journal of Remote Sensing, 26, 4485–4498.

Ummenhofer, C. C., England, M. H., McIntosh, P. C., Meyers, G. A., Pook, M. J., Risbey, J. S., et al. 2009. What causes southeast Australia's worst droughts? Geophysical Research Letters, 36, L04706.

Van Dijk, A. I. J. M., Beck, H. E., Crosbie, R. S., de Jeu, R. A. M., Liu, Y. Y., Podger, G. M., et al. 2013. The Millennium Drought in southeast Australia (2001-2009): Natural and human causes and implications for water resources, ecosystems, economy, and society. Water Resources Research, 49, 1040–1057.

Verdon-Kidd, D. C. and Kiem, A. S. 2009a. Nature and causes of protracted droughts in southeast Australia: Comparison between the Federation, WWII, and Big Dry droughts. Geophysical Research Letters, 36, L22707.

Verdon-Kidd, D. C. and Kiem, A. S. 2009b. On the relationship between large-scale climate modes and regional synoptic patterns that drive Victorian rainfall. Hydrology and Earth System Sciences, 13(4), 467–479.

Verdon-Kidd, D. C. and Kiem, A. S. 2014. Synchronicity of historical dry spells in the Southern Hemisphere. Hydrology and Earth System Sciences, 18, 2257–2264.

Wang, C., Zhao, C., Xu, Z., Wang, Y., Peng, H. 2013. Effect of vegetation on soil water retention and storage in a semi-arid alpine forest catchment. Journal of Arid Land, 5, 207–219.

Watkins, M. M., Wiese, D. N., Yuan, D.-N., Boening, C., Landerer, F. W. 2015. Improved methods for observing Earth's time variable mass distribution with GRACE using spherical cap mascons. Journal of Geophysical Research: Solid Earth, 120, 2648–2671.

Wiese, D. N., Landerer, F. W., Watkins, M. M. 2016. Quantifying and reducing leakage errors in the JPL RL05M GRACE mascon solution. Water Resources Research, 52, 7490–7502.

Xie, Z., Huete, A., Restrepo-Coupe, N., Ma, X., Devadas, R., Caprarelli, G. 2016. Spatial partitioning and temporal evolution of Australia's total water storage under extreme hydroclimatic impacts. Remote Sensing of Environment, 183, 43–52.

Zhao, M. and Running, S. W. 2010. Drought-induced reduction in global terrestrial net primary production from 2000 through 2009. Science, 329, 940–943.

3 NON-LINEAR INTERACTIONS BETWEEN VEGETATION AND TERRESTRIAL WATER STORAGE IN AUSTRALIA

3.1 Introduction

Radiation, temperature, and water availability are important drivers for surface vegetation conditions. At the global scale, vegetation growth is limited by radiation in rainforests and temperature at high northern latitudes (Nemani et al., 2003). Over approximately half of the earth's vegetated surface, vegetation growth is driven by the availability of water (Nemani et al., 2003; Seddon et al., 2016). Australia is a water-limited region, where the ecosystems play an important role in contributing to the global carbon and water cycles (Poulter et al., 2014; Ahlström et al., 2015; Cleverly et al., 2016). Previous studies have investigated how vegetation responds to land water conditions in Australia (Yang et al., 2014; Andrew et al., 2017; Xie et al., 2019). However, vegetation can also strongly influence terrestrial water storage by regulating evapotranspiration and altering the terrestrial water cycle (Wei et al., 2018; Zeng et al., 2018). Therefore, the two-way relationship between surface vegetation and land water conditions in Australia remains to be understood.

Vegetation takes up water from the root zone, and soil moisture is replenished by precipitation. Thus, precipitation and soil water content data are commonly used to indicate the water condition on which vegetation relies. However, a lack of continuous soil moisture observations in both time and space is a major impediment for large-scale investigation of vegetation and soil water relationships (Seneviratne et al. 2010). In-situ measurements of soil moisture are costly and lack broad spatial coverage (Robock et al., 2000; Robinson et al., 2008). Outputs from land surface models, such as the Global Land Data Assimilation System (GLDAS, Rodell et al., 2004) and the Global Soil Wetness Project 2 (GSWP-2, Dirmeyer et al., 2006), are dependent on the quality of forcing data. Remote sensing soil moisture products, such as the Advanced Microwave Scanning Radiometer (AMSR-E), the Soil Moisture and Oceanic Salinity (SMOS), and the Soil Moisture Active and Passive (SMAP), only provide direct sensing of soil moisture of the top 5 cm of the soil column.

The Gravity Recovery and Climate Experiment (GRACE) terrestrial water storage (TWS) have emerged as a useful data source for investigating vegetation-soil moisture relationships. For example, Yang et al. (2014) reported that GRACE TWS can be used for assessing hydrological impacts on surface vegetation conditions in Australia. For the first time, Xie et al. (2019) investigated the

interactions between vegetation greenness and GRACE TWS at the global scale based on a linear relationship, which indicated that significant positive TWS-NDVI relationships appear in approximately 43.17% of global vegetated areas.

Since the interactions between vegetation and climate conditions are most likely non-linear (Foley et al., 1998; Zeng, 2002), Papagiannopoulou et al. (2017) proposed a non-linear Granger causality framework to investigate the climate-vegetation dynamics. The Granger causality test was first proposed by the economist Granger (1969) and has been applied to investigate the vegetation-climate interactions in recent years (e.g., Jiang et al., 2015; Kong et al., 2018; Xie et al., 2019). This method assumes that variable x 'Granger causes' variable y if the past time series of variable x improves predicting the future time series of variable y. Although the Granger causality test does not confirm a direct physical mechanism between two variables, it provides implications of possible causality links from a statistical perspective.

Here we present a study on non-linear interactions between land water conditions represented by the GRACE TWS and surface vegetation conditions indicated by the normalized difference vegetation index (NDVI) in Australia. The objectives of this study are (1) to compare the performance of GRACE TWS and precipitation in investigating the relationship between surface vegetation and land water conditions, (2) to analyse the bidirectional causality relationships between surface vegetation and land water conditions with respect to different vegetation types, and (3) to revisit spatial patterns of water limitation on vegetation in comparison to temperature and radiation in Australia.

3.2 Methodology

3.2.1 Land water condition relevant data

A 31-year (1985–2015) reconstructed GRACE TWS dataset (Humphrey et al., 2017) provided by the Institute for Atmospheric and Climate Science, ETH, available from http://rossa-prod-ap21.ethz.ch/delivery/DeliveryManagerServlet?dps_pid=IE5766472, is used in this study. The 14-year (2003–2016) original GRACE TWS dataset (RL06M.MSCNv01) (Watkins et al., 2015; Wiese et al., 2016) provided by the NASA Jet Propulsion Laboratory (JPL), available from https://grace.jpl.nasa.gov/, is also considered for comparison. Monthly precipitation data provided by the Global Precipitation Climatology Centre (GPCC, Schneider et al., 2015) available from https://www.esrl.noaa.gov/psd/thredds/catalog/Datasets/gpcc/full_v7/catalog.html are used to compare with TWS in examining the relationship between vegetation and land water conditions. As

the effects of land water condition on vegetation may be relevant to plant available water capacity, the 0–1 m plant available water capacity data provided by the Australian Soil Resource Information System (ASRIS) are used in this study. The data are available from https://www.asris.csiro.au/themes/NationalGrids.html.

3.2.2 Vegetation relevant data

We used The Global Inventory Monitoring and Modelling System (GIMMS) Normalized Difference Vegetation Index (NDVI) data (Tucker et al., 2005; Pinzon and Tucker, 2014) for the same time period as the reconstructed GRACE TWS data (1985–2015), which were downloaded from https://climatedataguide.ucar.edu/climate-data/ndvi-normalized-difference-vegetation-index-3rd-generation-nasagfsc-gimms. The Moderate-resolution Imaging Spectroradiometer (MODIS) land cover classification data are used to identify different vegetation types across Australia, which were downloaded from https://neo.sci.gsfc.nasa.gov/view.php?datasetId=MCD12C1_T1. The five types include forest, shrubland, savanna, grassland, and agricultural land (Figure 3.1).

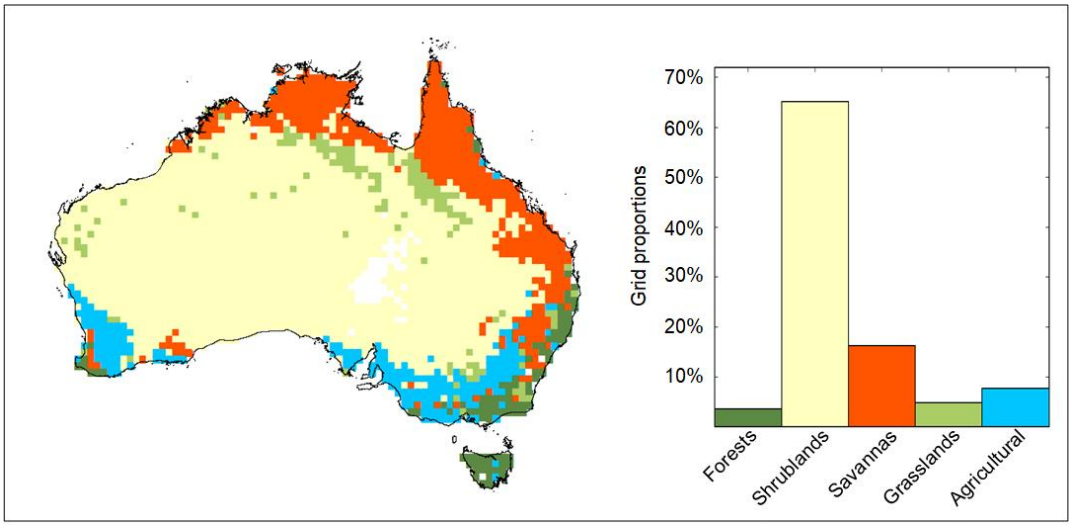

Figure 3.1 Land cover classification (MODIS) over Australia. The white area indicates barren land.

3.2.3 Other climate data

As temperature and radiation are important drivers for surface vegetation conditions, the ERA5 air temperature and net radiation datasets, available from https://cds.climate.copernicus.eu/, are also applied in this study. All the datasets are used at a 0.5° × 0.5° spatial resolution.

3.2.4 Correlation analysis

The Pearson linear correlation is applied to examine relationships between NDVI versus precipitation and TWS. Considering the autocorrelation of datasets, the effective sample size

(Bretherton et al., 1999) is used in the statistical significance testing for the correlation coefficient between two time series. The 0.05 significance level is adopted in this study.

3.2.5 Non-linear Granger causality analysis

The Granger causality method can test possible causal relationships (e.g., forcing and feedback) between variations in the vegetation and climate change (Jiang et al., 2015; Kong et al., 2018). The non-linear Granger causality analysis (Papagiannopoulou et al., 2017) is applied in this study to investigate the interaction between vegetation and land water conditions over Australia. Variable x Granger causes variable y if the autoregressive forecast of y is improved by considering the information about x. A linear vector autoregressive model can be used to derive the predictions required to determine Granger causality, which is represented as:

$$\begin{bmatrix} y_t \\ x_t \end{bmatrix} = \begin{bmatrix} \beta_{01} \\ \beta_{02} \end{bmatrix} + \sum_{p=1}^{P} \begin{bmatrix} \beta_{11p} & \beta_{12p} \\ \beta_{21p} & \beta_{22p} \end{bmatrix} \begin{bmatrix} y_{t-p} \\ x_{t-p} \end{bmatrix} + \begin{bmatrix} \epsilon_1 \\ \epsilon_2 \end{bmatrix}, \quad (3\text{-}1)$$

where β_{ij} are parameters that need to be estimated and ϵ_1 and ϵ_2 are white noise error terms. *p* is the length of the lag-time moving window. If at least one of the parameters β_{12p} at any *p* significantly differs from 0, it can be concluded that time series *x* Granger causes time series *y*. The following two models compare the two situations of including information of both *x* and *y* (Eq. (2)) versus only considering information about *y* (Eq. (3)):

$$y_t = \widehat{y_t} + \epsilon_1 = \beta_{01} + \sum_{p=1}^{p} (\beta_{11p} y_{t-p} + \beta_{12p} x_{t-p}) + \epsilon_1, \quad (3\text{-}2)$$

$$y_t = \widehat{y_t} + \epsilon_1 = \beta_{01} + \sum_{p=1}^{p} \beta_{11p} y_{t-p} + \epsilon_1. \quad (3\text{-}3)$$

Here, we replace the traditional autoregressive models (Eq. (2) and (3)) in the Granger-causality framework with non-linear machine learning models, i.e., the random forest. The Scikit-learn library is used to implement the random forest regression, with the number of trees equal to 100 and the maximum number of predictor variables per node equal to the square root of the total number of predictor variables. In addition, a regularization parameter is included in the fitting process to avoid overfitting in the Granger causality analysis context when the number of considered time series increases. More details can be found in Papagiannopoulou et al., (2017). The authors proposed a performance measure based on the coefficient of determination (R^2) to evaluate the forecast. It is defined as:

$$R^2(y,\hat{y}) = 1 - \frac{RSS}{TSS} = 1 - \frac{\sum_{i=p+1}^{N}(y_i - \hat{y}_i)^2}{\sum_{i=p+1}^{N}(y_i - \bar{y})^2}, \quad (3\text{-}4)$$

where $\bar{y}$ is the mean of *y*, and $\hat{y}$ is the predicted time series of *y* obtained from a given forecasting model. *p* =12 months is adopted in this study as time windows longer than 12 months do not improve the predictions (Papagiannopoulou et al., 2017). The quantification of the Granger causality is represented by R^2, which increases as the performance of the model improves. Positive R^2 means *x* Granger causes *y* and negative R^2 means predictions are less representative of the observations than the mean of the observations.

In addition, due to the existence of trends and seasonality in NDVI, precipitation and TWS time series, parts of them might be non-stationary and unsuitable for direct application of the Granger causality test (Kong et al., 2018). After the trends and seasonality are removed, all the time series are tested for stationarity by the augmented Dickey-Fuller (ADF) unit root test. After the processing, the non-linear Granger causality test is applied.

3.3 Results and Discussion

3.3.1 Linear correlation between NDVI versus precipitation and TWS

Pearson correlations between the concurrent monthly anomalies of NDVI versus precipitation and TWS are shown in Figure 3.2 (a) and Figure 3.2 (b), respectively ('anomaly' means that the seasonality in the time series of a variable has been removed). Significant TWS-NDVI correlation is observed for 86.5% of the grid cells, and most of the correlation coefficients (*r*) are larger than 0.3 (Figure 3.2 (b)). Areas with significant precipitation-NDVI correlation only account for 25.6%, and most of the correlation coefficients are smaller than 0.3 (Figure 3. 2 (a)). NDVI in the current month is expected to be more likely affected by precipitation in previous months because the vegetation in response to water input often occurs with a lag. In addition, individual monthly precipitation only represents water conditions in the current month, while TWS can reflect previous conditions. Therefore, the cumulated precipitation anomaly is applied to compare with the TWS anomaly in the lag correlation analysis on vegetation response to land water conditions (TWS or cumulated precipitation precedes NDVI).

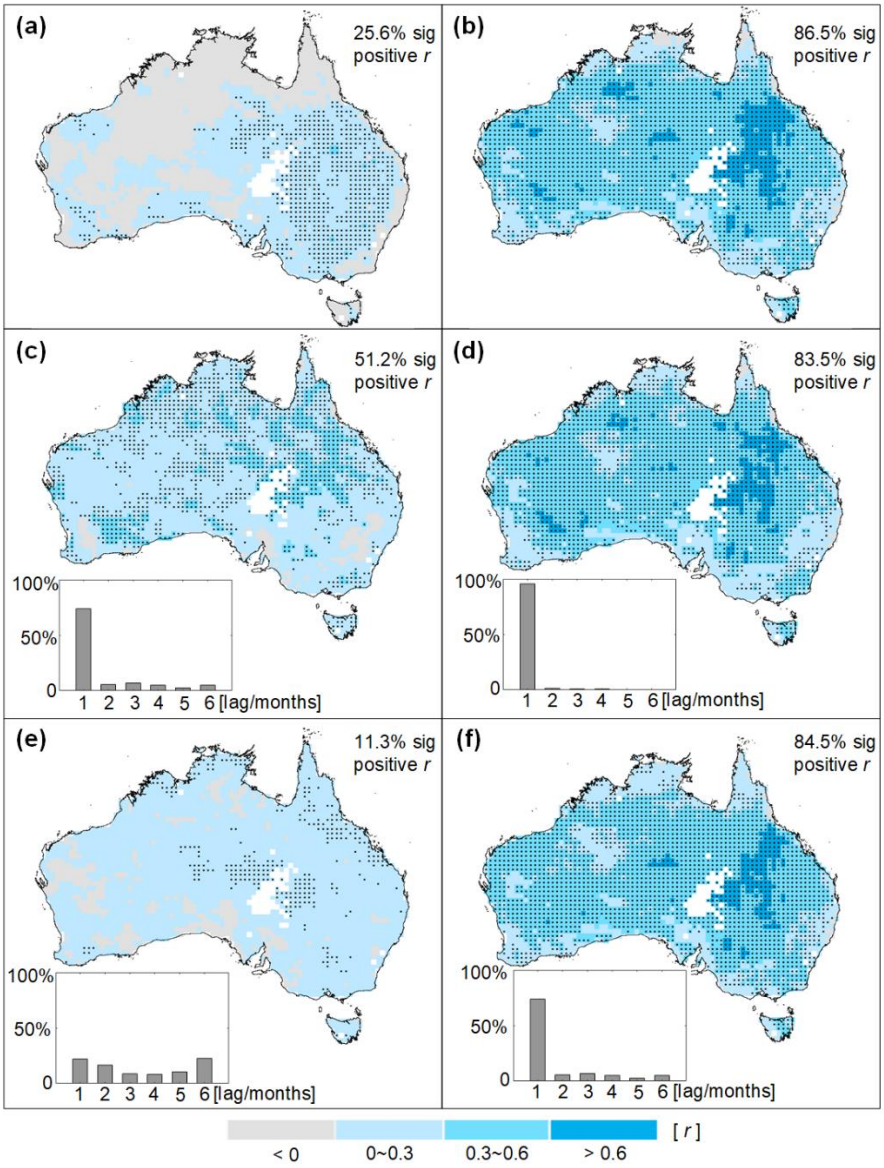

Figure 4.2 Pearson correlations between the concurrent monthly NDVI and precipitation (a) and TWS anomalies (b); lag correlation coefficient map (maximum *r*) between monthly NDVI and (c) cumulated precipitation and (d) TWS anomalies (histograms show the corresponding time lags); lag correlation coefficient map (maximum *r*) with NDVI preceding individual monthly precipitation (e) and TWS anomalies (f). Black dots denote significant levels. The white area indicates barren land. Grey area in the maps means $r < 0$.

The spatial distribution of the maximum positive correlations between NDVI anomaly versus cumulated precipitation anomaly and TWS anomaly and their corresponding time lags (1–6 months) are demonstrated in Figure 3.2 (c) and (d), respectively. Here time lags of 1–6 months are adopted based on previous studies investigating lag correlations between NDVI and precipitation/TWS at continental (Yang et al., 2014) and global scales (Xie et al., 2019). As expected, Figure 3.2 (c) demonstrates that cumulated precipitation shows stronger effects on surface vegetation conditions

than individual monthly precipitation. 51.2% of the grid cells have a significant positive correlation between cumulated precipitation and NDVI. Results of lag correlation analysis on TWS and NDVI (Figure 3.2 (d)) indicate that the percentage of grid cells with significant positive TWS-NDVI correlation (83.5%) is even larger than that of the cumulated precipitation-NDVI relationship. TWS also has a relatively higher correlation (r>0.3) with NDVI over a larger area than that for cumulated precipitation. The optimal time lag of maximum positive TWS-NDVI and cumulated precipitation-NDVI correlations are both dominated by 1 month, and the former has a larger percentage of grid cells with an optimal time lag of 1 month than that of the latter one. However, cumulated precipitation-NDVI correlation accounts for a larger percentage of grid cells with optimal time lags of 2–6 months than for TWS-NDVI correlation. Results in Figures 3.2. (a–d) indicate that TWS performs better than precipitation in examining the effects of terrestrial water conditions on surface vegetation conditions.

The fact that surface vegetation condition depends on water availability, especially in water-limited regions, is well-known (Nemani et al., 2003). How land-greenness affects the global water cycle and regional terrestrial water balance has also been investigated in recent years (e.g., Feng et al., 2016; Koirala et al., 2017; Zeng et al., 2018). For Australia, Chen et al., (2021) revealed a seesaw wetting/drying pattern between the eastern and western parts of the continent, which has been attributed to bidirectional vegetation and root zone moisture interactions. While it is intuitive that soil moisture condition influences surface vegetation condition, it is not as clear how vegetation cover may impact the temporal variability of soil moisture. Hence, Figures 3.2 (e) and (f) compare the spatial distribution of maximum positive NDVI-precipitation and NDVI-TWS relationships and their corresponding time lags (NDVI precedes precipitation/TWS). Only 11.3% of the grid cells show significant positive NDVI-precipitation correlation (Figure 3.2 (e)), while the percentage of grid cells with significant positive NDVI-TWS correlation is much larger, 88.3% (Figure 3.2 (f)). The optimal time lag of maximum positive NDVI-TWS correlation is dominated by 1 month, while NDVI-precipitation correlation shows different time lags.

Results of Figure 3.2 indicate that both unidirectional and bidirectional effects occur between surface vegetation and land water conditions in Australia. Based on linear correlation analysis, TWS performs better than precipitation in representing terrestrial water conditions in interaction with surface vegetation conditions. In a global-scale study on the hotspots of interactions between NDVI and TWS (Xie et al., 2019), land water condition was identified as the unidirectional cause of NDVI for most areas of Australia, but this result was based on a linear relationship. Since the vegetation-

water relationships are most likely non-linear (Foley et al., 1998; Zeng, 2002), we apply in the next section a non-linear Granger causality framework to investigate the unidirectional and bidirectional causality relationships between surface vegetation and water conditions in Australia.

3.3.2 Unidirectional and bidirectional causality relationships between surface vegetation and land water conditions with respect to different vegetation types

Figures 3.3 (a) and (c) respectively show the maps of non-linear Granger cause from precipitation and TWS to NDVI anomalies in Australia. Precipitation and TWS Granger cause the variability in NDVI of respectively 59.0% and 91.9% of the total number of grid cells. It indicates that TWS can better represent the forcing of water conditions on vegetation than precipitation. It may be because only part of the total precipitation is consumed by vegetation, and thus precipitation only provides indirect information on the plant water conditions (Chen et al., 2013; Yang et al., 2014), while the TWS water storage is a more direct indicator of soil moisture available for plant growth and thus associated with vegetation variations to a larger degree.

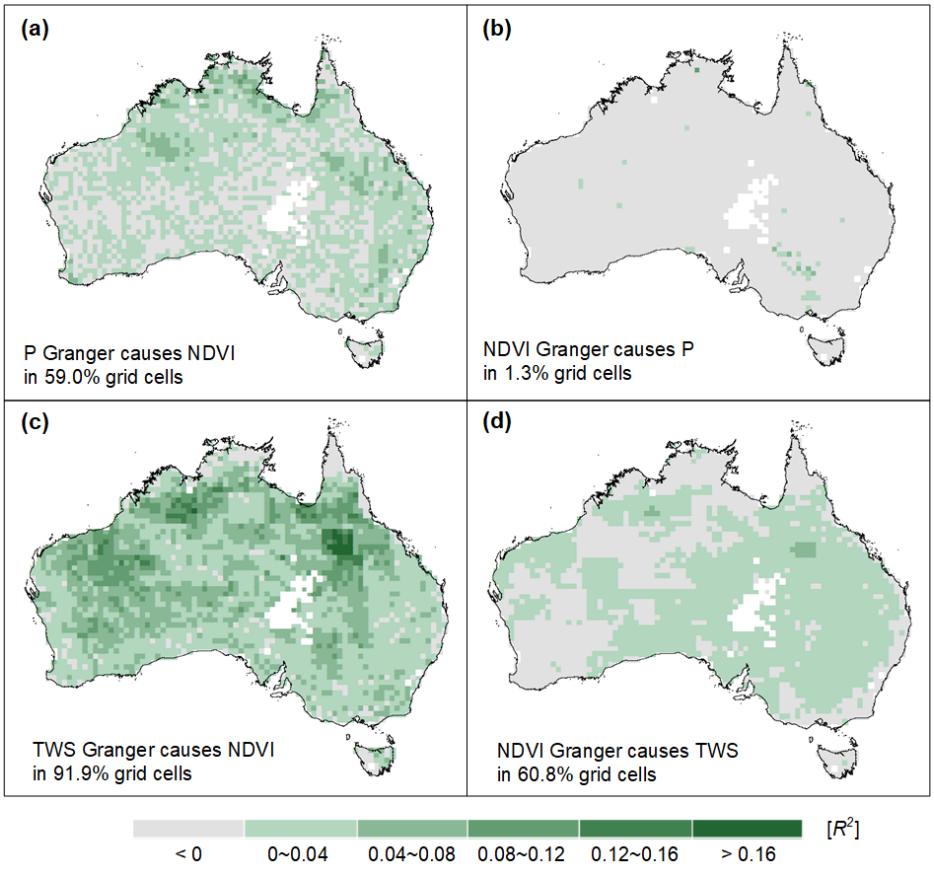

Figure 3.3 Non-linear Granger causality of (a) precipitation on NDVI; (b) NDVI on precipitation; (c) TWS on NDVI; (d) NDVI on TWS for 1985–2015.

In contrast, Figures 3.3 (b) and (d) respectively demonstrate the maps of non-linear Granger cause from NDVI to precipitation and TWS anomalies. Vegetation barely Granger causes precipitation (Figure 3.3 (b)), which is not surprising as it is generally understood that precipitation in Australia is driven by large-scale ocean-atmosphere drivers, such as El Niño Southern Oscillation (ENSO) (Cai et al., 2011). NDVI Granger causes TWS in 60.8% of the grid cells in Australia (Figure 3.3 (d)). Vegetation plays an important role in influencing the permeability and water retention capacity of the soil, e.g., poor vegetation cover tends to favour runoff generation and soil erosion (Mohammad and Adam, 2010). In addition, the Granger cause from TWS to NDVI is mainly observed in eastern Australia; it may be partially explained by the relatively larger plant available water capacity (Figure 3.4).

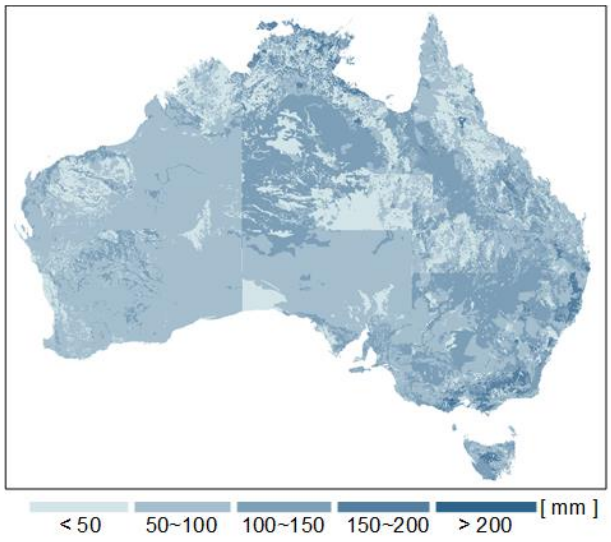

Figure 5.4 0–1m plant water available capacity (mm) in Australia. Data are provided by Australian Soil Resource Information System (ASRIS).

Results of Figure 3.3 indicate that compared to precipitation, TWS is a better indicator of land water condition in examining its non-linear relationship with surface vegetation condition. Therefore, further investigation on the interactions between surface vegetation and land water conditions with respect to different vegetation types is based on TWS rather than precipitation. Besides, as Figures 3.3 (c) and (d) are based on the reconstructed TWS dataset (1985–2015), we also repeated for comparison the non-linear Granger causality analysis for the original GRACE TWS data from 2003 to 2016. The results are shown in Figure 3.5. Based on the 14-year data, TWS Granger causes NDVI in 85.5% of the grid cells, and NDVI Granger causes TWS in 66.0% of the grid cells. The

apparent blocky pattern observed in part of Figures 3.3 (c–d) and Figure 3.5 is very likely an imprint of the original 3°×3° resolution of the GRACE TWS (Watkins et al., 2015). Thus, the TWS signal of the downscaled 0.5°×0.5° grid is dependent on the surrounding grids. The applicability and reliability of the original GRACE TWS data will increase with the accumulation of data and improved GRACE resolution in the future.

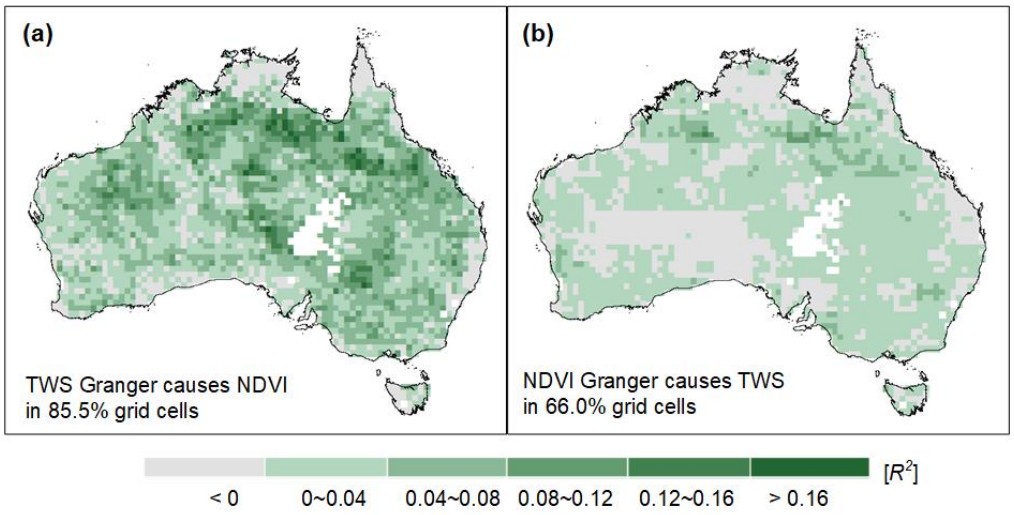

Figure 3.5 Non-linear Granger causality of (a) TWS on NDVI; (b) NDVI on TWS during 2003–2016 based on JPL GRACE TWS data.

The unidirectional effect from TWS on NDVI is observed in 33.5% of the grid cells (Figure 3.6 (a)). The effect of the opposite direction is only observed in 2.5% of the grid cells (Figure 3.6 (b)). This is explained by the fact that in most cases where NDVI Granger causes TWS, TWS Granger causes NDVI too. Bidirectional causality relationships between TWS and NDVI is therefore observed over half (58.4%) of the study area (Figure 3.6 (c)). The proportion of bidirectional causal relationships shown here is larger than that detected by linear Granger causality analysis at a global scale (Xie et al., 2019).

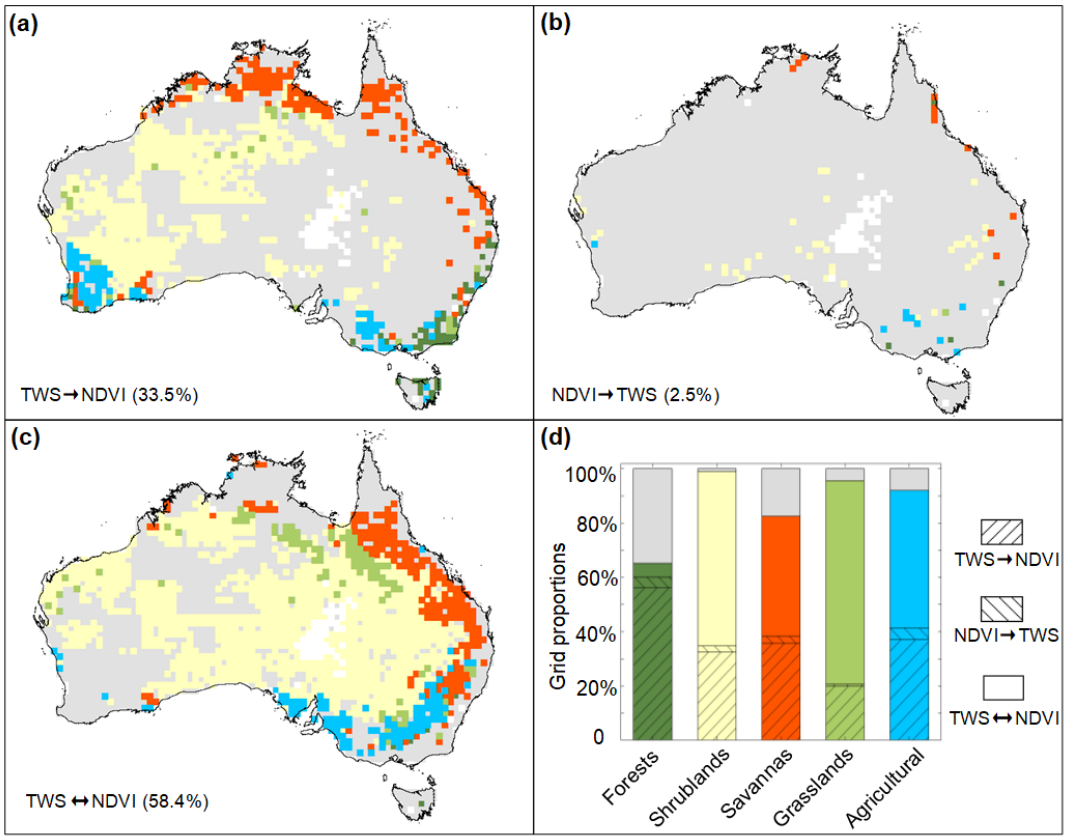

Figure 3.6 Unidirectional and bidirectional causality relationships between TWS and NDVI revealed by the Non-linear Granger causality test: (a) TWS unidirectional effects NDVI; (b) NDVI unidirectional effects TWS; (c) TWS-NDVI interactions, (d) the corresponding grid proportions for different vegetation types.

Figure 3.6 (d) shows the proportions of the unidirectional and bidirectional relationships between TWS and NDVI for different vegetation types. The highest proportion of TWS-NDVI interactions is observed in grasslands, followed by shrublands, agricultural lands and savannas, and lowest in forests. It seems that the interaction is more likely to be detected in regions covered by vegetation with relatively shallower roots. The largest proportion of grid cells without detected TWS-NDVI interaction is observed in the forest class. This apparent result may be because Australia is prone to bushfires, which could disturb the detection of the causal effect from NDVI to TWS.

3.3.3 Comparison of the influence of water, temperature, and radiation on surface vegetation condition in Australia

In addition to water availability, temperature and radiation are also important drivers for surface vegetation conditions, and those factors are commonly used to investigate the effect of climate change on global ecosystems and the corresponding feedbacks. Therefore, we also quantify the impacts of temperature and radiation on vegetation by following the non-linear Granger

causality framework. Figures 3.7 (a–b) show that air temperature and net radiation respectively Granger causes NDVI in 82.8% and 62.4% of the grid cells. By comparing the non-linear Granger causality (R^2) with TWS, air temperature, and net radiation versus NDVI, 61.6% of the grid cells in Australia are dominantly driven by water availability (Figure 3.7 (c)). This confirms that Australia is primarily water limited. However, the water-dominant regions are smaller than that reported by Nemani et al. (2003), who investigated the dominant climate driver for terrestrial net primary production from 1982 to 1999 at the global scale.

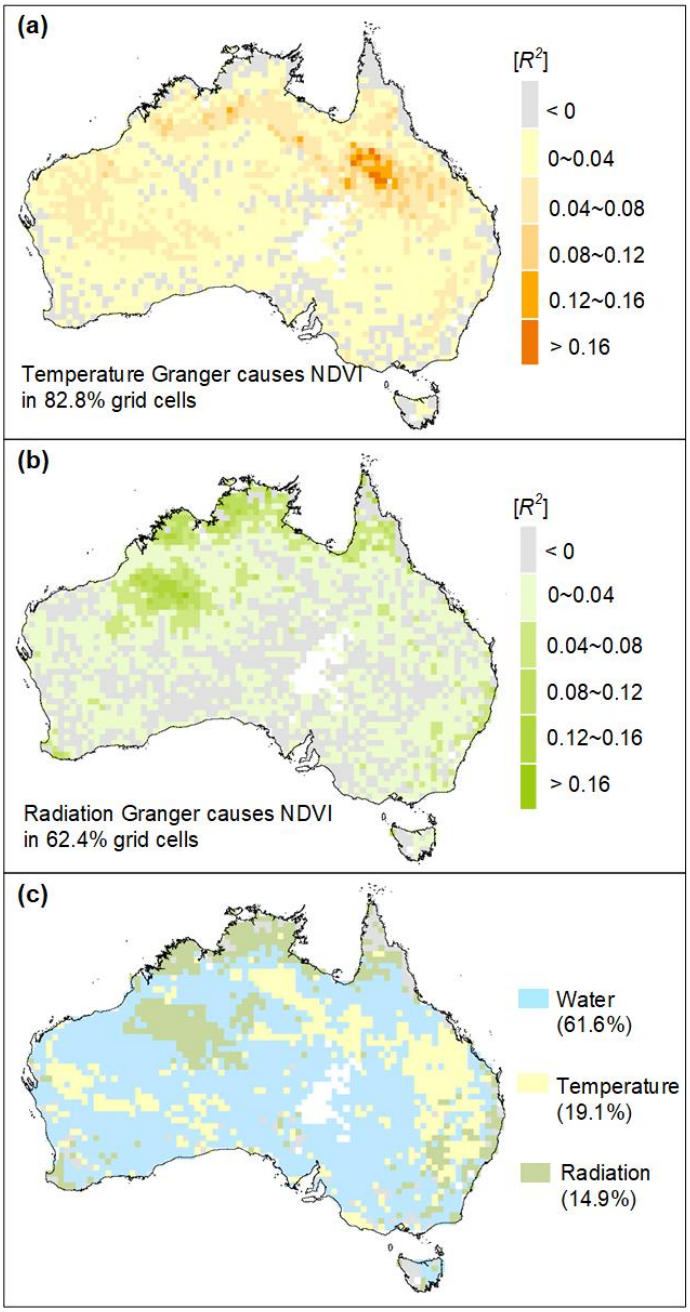

Figure 3.7 Non-linear Granger causality of (a) temperature on NDVI; and (b) net radiation on NDVI. (c) Spatial pattern of the largest non-linear Granger causality among three important climate drivers (water, temperature, radiation) for surface vegetation conditions.

Temperature is identified to be the dominant driver for 19.1% of the grid cells in this study (Figure 3.7 (c)). When temperature is a constraint for plant growth, like at high northern latitudes, the temperature is too low to sustain a normal level of plant physiological activities. In our study, those temperature-dominant regions show extremely high negative temperature-NDVI correlation (Figure 3.8 (a)), which more likely means that vegetation greenness is impeded by high temperature (Qiu et al., 2019; Yang et al., 2019). High temperature can directly limit plant growth by leading to

changes in physiology (Prasad et al., 2017) and metabolic response (Haldimann and Feller, 2004; Bheemanahalli et al., 2019). At the same time, high temperature may, in some situations, increase evapotranspiration, leading to declining soil moisture. Consequently, this will indirectly limit vegetation's photosynthesis and growth rate (Yang et al., 2019). The adverse effects of high temperature on surface vegetation conditions in Australia should be taken seriously as the occurrence of simultaneous drought and heatwaves are more likely to cause serious damages (Mazdiyasni and AghaKouchak 2015).

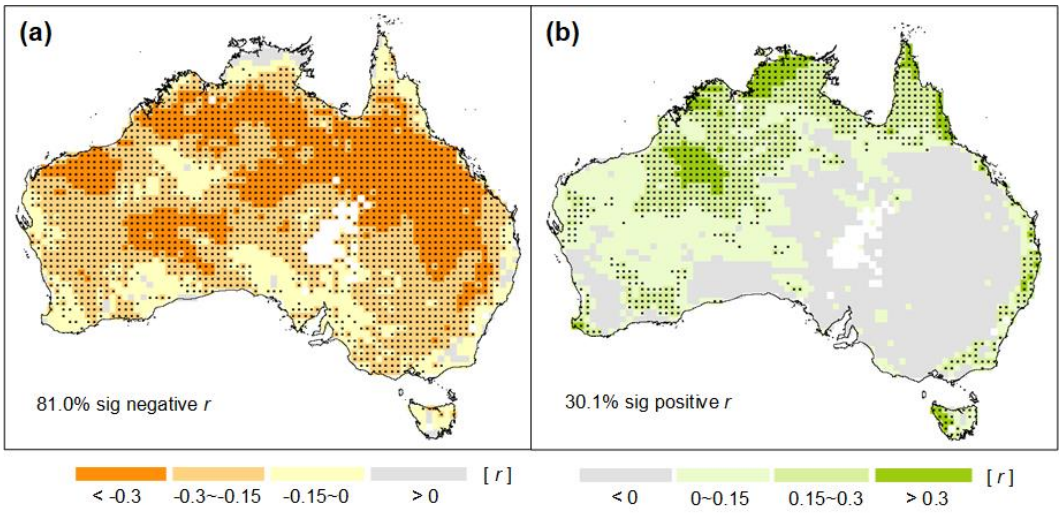

Figure 3.8 Pearson correlation coefficient (*r*) between NDVI and (a) 2 m air temperature and (b) net radiation in Australia during 1985–2015.

Radiation dominates NDVI changes in 14.9% of the grid cells, which are mostly located in the northwestern part of Australia. Here significant positive correlation between net radiation and NDVI are observed (Figure 3.8 (b)). We calculated annual average precipitation/annual average evapotranspiration during 1985-2015 for each grid cell to identify energy-limited and water-limited regions (Figure 3.9) by following McVicar et al., (2012). Radiation-dominant regions shown in Figure 3.7 (c) are included in the energy-limited regions shown in Figure 3.9, the spatial distribution of those radiation-dominant regions is also generally consistent with a more recent study (Seddon et al., 2016) on identifying dominant drivers for vegetation productivity among three climate variables: water, temperature, and cloud cover at the global scale. Although water-dominant regions account for a larger proportion than temperature-dominant and radiation-dominant regions in Australia (Figure 3.7 (c)), water-dominant regions seem to have become smaller in recent years compared to that of last century (see Nemani et al., 2003; McVicar et al., 2012). This change may be related to the warmer climate in recent years. Possible causes are worthy of further exploration in the future.

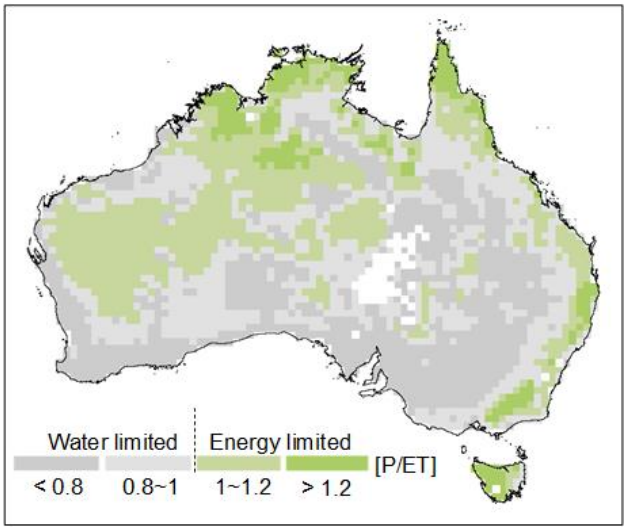

Figure 3.9 Distribution of energy-limited and water-limited areas identified by annual average precipitation (P)/annual average evapotranspiration (ET) during 1985–2015.

3.4 Conclusions

In this study, we aimed to investigate the non-linear relationship between surface vegetation and land water conditions in Australia and to revisit the spatial patterns of water limitation on vegetation in comparison to temperature and radiation. NDVI characterizes surface vegetation conditions, and terrestrial water conditions are reflected by precipitation and TWS. The non-linear Granger causality analysis is applied to identify the unidirectional and bidirectional causality relationships between NDVI versus precipitation and TWS. TWS appears to be a better indicator of terrestrial water condition than precipitation in examining its interactions with NDVI. TWS is found to be a Granger cause of changes in vegetation for 91.9% of the grid cells, while NDVI Granger causes TWS in 60.8% of the grid cells. TWS-NDVI interactions are detected in over half (58.4%) of the continent, which tend to occur more in areas with short-rooted plants. Furthermore, by comparing the Granger causality of three dominant drivers (i.e., TWS, air temperature, and net radiation) for surface vegetation condition, it is confirmed that Australia is mostly water-limited as TWS dominantly drives NDVI changes for 61.6% of the grid cells. Temperature- and radiation- dominant regions, respectively, accounting for 19.1% and 14.9% of the grid cells, which is larger than reported in the past. This possible trend is worthy of further investigation in the future. The interaction established herein between TWS and NDVI help to improve our understanding of the continental terrestrial water and carbon cycles.

3.5 References

Ahlström, A., Raupach, M.R., Schurgers, G., Smith, B., Arneth, A., Jung, M., Reichstein, M., Canadell, J.G., Friedlingstein, P., Jain, A.K., Kato, E., Poulter, B., Sitch, S., Stocker, B., Viovy, N., Wang, Y.P., Wiltshire, A., Zaehle, S., Zeng, N. 2015. The dominant role of semi-arid ecosystems in the trend and variability of the land CO_2 sink. Science. 348, 895–899.

Andrew, R. L., Guan, H.D., Batelaan, O. 2017. Large-scale vegetation responses to terrestrial moisture storage changes. Hydrology and Earth System Science. 21, 4469–4478.

Bheemanahalli, R., Sunoj, V.S.J., Saripalli, G., Prasad, P.V.V., Balyan, H.S., Gupta, P.K., Grant, N., Gill, K.S. and Jagadish, S.V.K. 2019. Quantifying the impact of heat stress on pollen germination, seed set and grain filling in spring wheat. Crop Science. 59, 684–696.

Bretherton, C.S., Widmann, M., Dymnikov, V.P., Wallace, J. M., Blade, I. 1999. The effective number of spatial degrees of freedom of a time-varying field. Journal of Climate. 12(7), 1990–2009.

Cai, W., van Rensch, P., Cowan, T., Hendon, H. H. 2011. Teleconnection Pathways of ENSO and the IOD and the Mechanisms for Impacts on Australian Rainfall. Journal of Climate. 24(15), 3910–3923.

Chen, A.J., Guan, H.D., Batelaan, O. 2021. Seesaw terrestrial wetting and drying between eastern and western Australia. Earths Future. 9, e2020EF001893.

Chen, Y., Velicogna, I., Famiglietti, J.S., Randerson, J.T. 2013. Satellite observations of terrestrial water storage provide early warning information about drought and fire season severity in the Amazon. Journal of Geophysical Research-Biogeosciences. 118, 495–504.

Cleverly, J., Eamus, D., Luo, Q.Y., Restrepo-Coupe, N., Kljun, N., Ma, X.L., Ewenz, C., Li, L.H., Yu, Q., Huete, A. 2016. The importance of interacting climate modes on Australia's contribution to global carbon cycle extremes. Scientific Report. 6, 23113.

Dirmeyer, P.A., Gao, X., Zhao, M., Guo, Z.C., Oki, T., Hanasaki, N. 2006. GSWP-2: multimodel analysis and implications for our perception of the land surface. Bulletin of the American Meteorological Society. 87,1381–1397.

Feng, X.M., Fu, B.J., Piao, S.L., Wang, S., Ciais, P., Zeng, Z.Z., Lü, Y.L., Zeng, Y., Li, Y., Jiang, X.H. 2016. Revegetation in China's loess plateau is approaching sustainable water resource limits. Nature Climate Change. 6, 1019.

Foley, J.A., Levis, S., Prentice, I.C., Pollard, D., Thompson, S.L. 1998. Coupling dynamic models of climate and vegetation. Global Change Biology. 4(5), 561–579.

Granger, C.W.J., 1969. Investigating causal relations by econometric models and crossspectral methods. Econometrica. 37(3), 424–438.

Haldimann, P. and Feller, U. 2004. Inhibition of photosynthesis by high temperature in oak (Quercus pubescens L.) leaves grown under natural conditions closely correlates with a reversible heat-dependent reduction of the activation state of ribulose-1,5-bisphosphate carboxylase/oxygenase. Plant, Cell & Environment. 27(9), 1169–1183.

Humphrey, V. Gudmundsson, L., Seneviratne, S.I. 2017. A global reconstruction of climate-driven sub-decadal water storage variability. Geophysical Research Letter. 44, 2300–2309.

Jiang, B., Liang, S.L., Yuan, W.P. 2015. Observational evidence for impacts of vegetation change on local surface climate over northern China using the Granger causality test. Journal of Geophysical Research-Biogeosciences. 120, 1–12.

Koirala, S., Jung, M., Reichstein, M., de Graaf, I.E.M., Camps-Valls, G., Ichii, K., Papale, D., Ráduly, B., Schwalm, C.R., Tramontana, G., Carvalhais, N. 2017. Global distribution of groundwater-vegetation spatial covariation: global groundwater-vegetation relations. Geophysical Research Letter. 44, 4134–4142.

Kong, D.X., Miao, C.Y., Duan, Q.Y., Lei, X.H., Li, H. 2018. Vegetation-climate interactions on the Loess Plateau: A nonlinear Granger causality analysis. Journal of Geophysical Research-Atmospheres. 123, 11,068–11,079.

Mazdiyasni, O. and AghaKouchak, A. 2015. Substantial increase in concurrent droughts and heatwaves in the United States. Proceedings of the National Academy of Sciences of the United States of America. 112 (37), 11484–11489.

Mohammad, A.G. and Adam, M.A. 2010. The impact of vegetative cover type on runoff and soil erosion under different land uses. Catena. 81(2), 97–103.

Nemani, R.R., Keeling, C.D., Hashimoto, H., Jolly, W.M., Piper, S.C., Tucker, C.J., Myneni, R.B., Running, S.W. 2003. Climate-driven increases in global terrestrial net primary production from 1982 to 1999. Science. 300, 1560–1563.

Papagiannopoulou, C., Miralles, D.G., Decubber, S., Demuzere, M., Verhoest, N.E.C., Dorigo, W.A., Waegeman, W. 2017. A nonlinear Granger-causality framework to investigate climate-vegetation dynamics. Geoscientific Model Development. 10(5), 1945–1960.

Pinzon, J.E. and Tucker, C.J. 2014. A Non-Stationary 1981-2012 AVHRR NDVI3g Time Series. Remote Sensing of Environment. 6, 6929–6960.

Poulter, B., Frank, D., Ciais, P., Myneni, R.B., Andela, N., Bi, J., Broquet, G., Canadell, J.G., Chevallier, F., Liu, Y.Y., Running, S.W., Sitch, S. van der Werf, G.R. 2014. Contribution of semi-arid ecosystems to interannual variability of the global carbon cycle. Nature. 509, 600–603.

Vara Prasad, P.V., Bheemanahalli, R., Krishna Jagadish, S.V. 2017. Field crops and the fear of heat stress-opportunities, challenges, and future directions. Field Crops Research. 200, 114–121.

Qiu, B., Ge, J., Guo, W.D., Pitman, A.J., Mu, M.Y. 2020. Responses of Australian dryland vegetation to the 2019 heatwave at a subdaily scale. Geophysical Research Letter. 47, e2019GL086569.

Robinson, D.A., Campbell, C.S., Hopmans, J.W., Hornbuckle, B.K., Jones, S.B., Knight, R., Ogden, F., Selker, J., Wendroth, O. 2008. Soil moisture measurements for ecological and hydrological watershed scale observatories: a review. Vadose Zone Journal. 7, 358–389.

Robock, A., Vinnikov, K.Y., Srinivasan, G., Entin, J.K., Hollinger, S.E., Speranskaya, N.A., Liu, S.X., Namkhai, A. 2000. The global soil moisture data bank. Bulletin of the American Meteorological Society. 81 (6), 1281–1299.

Rodell, M., Houser, P.R., Jambor, U., Gottschalck, J., Mitchell, K., Meng, C.J., Arsenault, K., Cosgrove, B., Radakovich, J., Bosilovich, M., Entin, J.K., Walker, J.P., Lohmann, D., Toll, D. 2004. The global land data assimilation system. Bulletin of the American Meteorological Society. 85 (3),381–394.

Seddon, A.W., Macias-Fauria, M., Long, P.R., Benz, D., Willis, K.J. 2016. Sensitivity of global terrestrial ecosystems to climate variability. Nature. 531, 229–232.

Seneviratne, S.I., Corti, T., Davin, E.L., Hirschi, M., Jaeger, E.B., Lehner, I., Orlowsky, B. and Teuling, A.J. 2010. Investigating soil moisture-climate interactions in a changing climate: A review, Earth Science Review. 99, 125–161.

Schneider, U., Becker, A., Finger, P., Meyer-Christoffer, A., Rudolf, B., Ziese, M. 2015. GPCC full data monthly product version 7.0 at 1.0°: Monthly land-surface precipitation from rain-gauges built on GTS-based and historic data. doi.10.5676/DWD_GPCC/FD_M_V7_100

McVicar, T.R., Roderick, M.L., Donohue, R.J., Li, L.T., Van Niel, T.G., Thomas, A., Grieser, J., Jhajharia, D., Himri, Y., Mahowald, N.M., Mescherskaya, A.V., Kruger, A.C., Rehman, S., Dinpashoh, Y. 2012. Global review and synthesis of trends in observed terrestrial near-surface wind speeds: Implications for evaporation, Journal of Hydrology. 416-417, 182–205.

Tucker, C.J., Pinzon, J.E., Brown, M.E., Slayback, D.A., Pak, E.W., Mahoney, R., Vermote, E.F., Saleous, N.E. 2005. An extended AVHRR-8km NDVI dataset compatible with MODIS and SPOT vegetation NDVI data. International Journal of Remote Sensing. 26, 4485–4498.

Watkins, M.M., Wiese, D.N., Yuan, D.N., Boening, C. Landerer, F.W. 2015. Improved methods for observing Earth's time variable mass distribution with GRACE using spherical cap mascons. Journal of Geophysical Research-Solid Earth. 120, 2648–2671.

Wei, X.H., Li, Q., Zhang, M.F., Giles-Hansen, K., Liu, W.F., Fan, H.B., Wang, Y., Zhou, G.Y., Piao, S.L., Liu, S.R. 2018. Vegetation cover-another dominant factor in determining global water resources in forested regions. Global Change Biology. 24, 786–795.

Wiese, D.N., Landerer, F.W. Watkins, M.M. 2016. Quantifying and reducing leakage errors in the JPL RL05M GRACE mascon solution. Water Resources Research. 52, 7490–7502.

Xie, X.M., He, B., Guo, L.L., Miao, C.Y., Zhang, Y.F. 2019. Detecting hotspots of interactions between vegetation greenness and terrestrial water storage using satellite observations. Remote Sensing of Environment. 231, 111259.

Yang, Y.J., Wang, S.J., Bai, X.Y., Tan, Q., Li, Q., Wu, L.H., Tian, S.Q., Hu, Z.Y., Li, C.J., Deng, Y.H. 2019. Factors affecting long-term trends in global NDVI. Forests. 10 (5), 372.

Yang, Y.T., Long, D., Guan, H.D., Scanlon, B.R., Simmons, C.T., Jiang, L., Xu, X. 2014. GRACE satellite observed hydrological controls on interannual and seasonal variability in surface greenness over mainland Australia. Journal of Geophysical Research-Biogeosciences. 119, 2245–2260.

Zeng, N., 2002. Nonlinear dynamics in a coupled vegetation–atmosphere system and implications for desert–forest gradient. Journal of Climate. 15(23), 3474–3487.

Zeng, Z.Z., Piao, S.L., Li, L.Z., Wang, T., Ciais, P., Lian, X., Yang, Y.T., Mao, J.F., Shi, X.Y., Myneni, R.B. 2018. Impact of earth greening on the terrestrial water cycle. Journal of Climate. 31, 2633–2650.

4 GLOBAL SOIL MOISTURE-AIR TEMPERATURE COUPLING BASED ON GRACE-DERIVED TERRESTRIAL WATER STORAGE

4.1 Introduction

Soil moisture impacts the partitioning of available energy between sensible and latent heat fluxes and consequently influences temperature of land surface and the lower atmosphere. The effect of soil moisture on air temperature is commonly referred to as soil moisture-air temperature (θ-Ta) coupling (Seneviratne et al., 2010). Understanding and quantifying the θ-Ta coupling contributes to climate research and reduces uncertainties in projections of future climate (Cubasch et al., 2001).

The unprecedented 2003 heat wave event in Europe has drawn extensive attention from researchers (e.g., Black and Sutton, 2006; Fischer et al., 2007; Alexander, 2011), and the consequently improved understanding of physical processes behind heatwaves further highlights the important role of θ-Ta coupling in climate systems. Most previous studies on the θ-Ta coupling at both global (see Table 4.1) and regional scales (e.g., Seneviratne et al., 2006; Lorenz et al., 2010; Vogel et al., 2016) focused on hot seasons' air temperature or heat wave events. From them, global sensitive regions of θ-Ta coupling have been identified, such as the North American Great Plains, Australia, and the southern tip of Africa. In addition to those sensitive regions, India shows significant correlation between terrestrial water storage and temperature anomaly (Humphrey et al., 2016).

Study	Aim of study	Estimation of θ	Estimation of Ta	Method
Koster et al., 2006	Thoroughly describe and contrast the inherent coupling strengths of 12 participating models; Provides a full set of instructions for performing the experiments.	Model-derived θ (GLACE)	Summer temperature	Multimodel
Miralles et al., 2012	Fill the gap between climatological and event studies of soil moisture-temperature coupling.	Model-derived θ (GLEAM)	Summer temperature	Coupling metrics
Mueller and Seneviratne, 2012	Assess whether the relationship between hot days and precipitation deficits holds at the global scale.	SPI	Number of hot days	Correlation analysis,

				quantile regression analysis
Seneviratne et al., 2013.	Firstly present the results of a new multimodel experiment quantifying the impact of soil moisture-climate coupling in CMIP5 simulations.	Model-derived θ (GLACE CMIP5)	Extreme temperature; mean temperature	Simulations, Linear regression
Hirschi et al., 2014	Investigate the relation between the number of hot days and preceding soil moisture deficits.	RS-based θ (ESA CCI), Model-derived θ (GLDAS), In-situ θ;	Number of hot days	Correlation analysis, Linear regression
Berg et al., 2014	Perform a complete assessment of the impact of soil moisture dynamics on the distribution of daily surface temperature.	Model-derived θ (GLACE CMIP5)	Summer temperature	Probability distribution function
Lorenz et al., 2015	Investigate the coupling strength of ACCESS1.3b by examining different land–atmosphere coupling measures obtained from GLACE-1 and GLACE-CMIP5 experiments.	Model-derived θ (GLACE 1 & GLACE CMIP5)	Mean temperature, maximum temperature, minimum temperature	Model experiment, Correlation analysis, Quantile regression analysis
Schwingshackl et al., 2017	Analyse spatial and temporal variations of land-atmosphere coupling and its effect on near-surface air temperature by a simple framework for the dependence of evaporative fraction on soil moisture	Model-derived θ, (ERA-Interim/Land (0-100 cm))	Maximum temperature	Coupling analysis
Gevaert et al., 2017	Apply two different metrics of soil moisture-temperature coupling to a set of five land surface models and compare the results to observational data.	Model-derived θ, (EartH2Observe Project)	Temperature in warm season	Metrics
This study	Assess the skill of GRACE TWS in examining global θ-T_a coupling	Decomposed GRACE TWS, Model-derived θ (GLDAS)	Temperature anomaly	Stepwise regression analysis, Wavelet method

Table 4.1 A Summary of Studies on Examining θ-Ta Coupling at Global Scale. (GLACE = Global Land-Atmosphere Coupling Experiment; GRACE = Gravity Recovery and Climate Experiment; TWS = terrestrial water storage; GLEAM = Global Land Evaporation Amsterdam Model; CMIP5 = Coupled Model Intercomparison Project Phase 5; ESA CCI = European Space Agency Climate Change Initiative; GLDAS = Global Land Data Assimilation System.)

Most previous studies used soil moisture products including observed θ (Durre et al., 2000), model-derived θ (e.g., Jaeger and Seneviratne, 2011; Whan et al., 2015), and microwave remote sensing surface soil moisture (Hirschi et al., 2014). These soil moisture data sets have drawbacks in examining global θ-Ta coupling. The observed θ data sets lack large spatial coverage. In the case of modelled soil moisture, temperature is often an input variable in the land surface model that produces soil moisture estimation (Rodell et al., 2004). Correlation between this modelled soil moisture and air temperature for reflecting θ-Ta coupling is hence not very convincing. Given these limitations, precipitation derived indices have been commonly used as a proxy for soil moisture deficit (e.g., Hirschi et al., 2011; Mueller and Seneviratne, 2012; Perkins et al., 2015).

The Gravity Recovery and Climate Experiment-derived terrestrial water storage (GRACE TWS) has shown great success in quantifying water/moisture deficit (e.g., Thomas et al., 2014; Getirana, 2016; Sinha et al., 2017). Yang et al. (2014) suggested that GRACE TWS poses a more direct influence on surface greenness and ecosystem performance than precipitation. Andersen et al. (2005) reported that the 2003 excess GRACE TWS depletion could be related to the record-breaking heat wave that occurred in central Europe. As TWS directly reflects water storage, it seems to hold higher skill than precipitation-based indices in examining θ-Ta coupling. However, the potential of GRACE TWS for investigating this coupling has not been well explored. This is probably due to the fact that GRACE TWS reflects total water storage including ice, snow, surface water, soil moisture, and ground water (Ramillien et al., 2008). Hence, a large part of the GRACE TWS is not directly accessible for latent heat processes (evaporation and transpiration), which influence land surface energy balance. Recently, Andrew et al. (2017a) proposed to partition GRACE TWS into shallow and deep components by using a discrete wavelet decomposition.

Physically, the θ-Ta coupling reflects the effect of soil moisture on land surface energy partitioning. As shown in Figure 4.1, significant θ-Ta coupling is hypothesized to be attributed to both strong θ-Ts (land surface temperature) coupling and Ts-Ta correlation. In addition to the primary control from net radiation, Ts represents a lumped average of soil surface temperature and vegetation canopy temperature, which are driven by soil evaporation and plant transpiration,

respectively. It has been reported that low soil moisture availability reduces evaporative cooling and increases atmospheric heating from sensible heat flux (Seneviratne et al., 2010; Alexander, 2011). Besides, in regions with a moisture-limited regime, precipitation influences the θ-Ta coupling through replenishing root-zone soil moisture, which impacts land surface temperature and consequently air temperature. Meanwhile, precipitation and air temperature can be associated with each other via weather systems. Here, we propose the first use of wavelet decomposed GRACE TWS to study θ-Ta coupling at global scale. The three main objectives of this study are (1) to identify sensitive regions of θ-Ta coupling based on monthly air temperature anomalies at global scale; (2) to assess the skill of GRACE TWS data in examining θ-Ta coupling; and (3) to explore favourable factors for developing significant θ-Ta coupling.

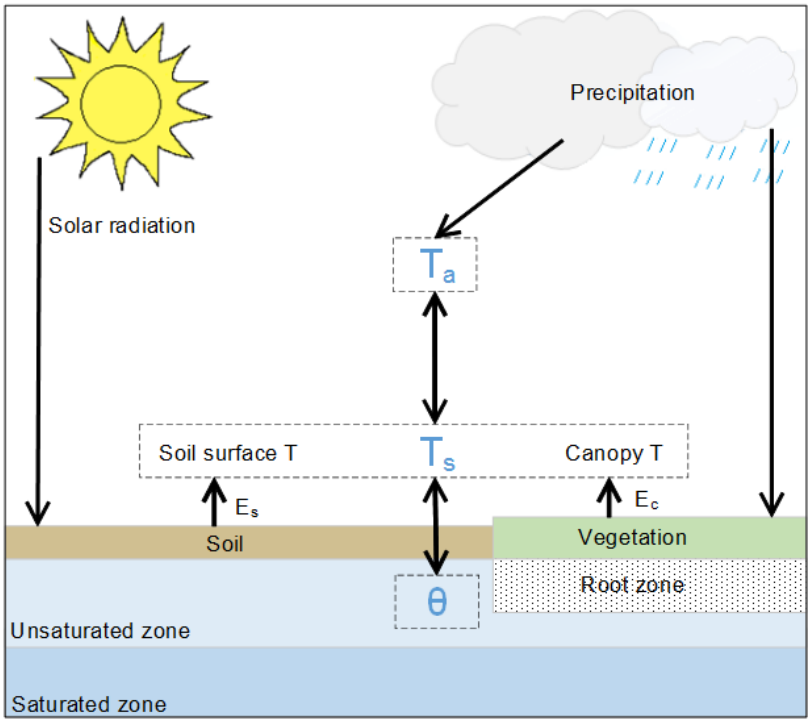

Figure 4.1 Schematic of soil moisture-air temperature (θ-Ta) coupling. Ts is land surface temperature, Es is soil evaporation, and Ec is plant transpiration.

4.2 Methodology

4.2.1 Data selection and calculation of anomalies

In this study, the global θ-Ta coupling is investigated using ERA-Interim 2-mair temperature (Ta, Dee et al., 2011) available from http://apps.ecmwf.int/datasets/data/interim-full-moda/levtype=sfc/, MOD11C3 Version 6 land surface temperature (Ts, Wan et al., 2015) available from https://neo.sci.gsfc.nasa.gov/view.php?datasetId=MOD_LSTAD_M, GPCC precipitation (P,

Schneider et al., 2015) available from https://www.esrl.noaa.gov/psd/thredds/catalog/Datasets/gpcc/full_v7/catalog.html, JPL GRACE TWS (Swenson et al., 2006; Swenson. 2012; Landerer and Swenson., 2012) available from ftp://podaac-ftp.jpl.nasa.gov/allData/tellus/L3/land_mass/RL05/netcdf/, ESA CCI remote sensing surface soil moisture of top–2 cm (θs, Dorigo et al., 2017; Liu et al., 2012; Gruber et al., 2017) available from http://www.esa-soilmoisture-cci.org/node/145, and GLDAS_NOAH model derived root-zone soil moisture of 0–100cm (θm, Rodell et al., 2004; Beaudoing and Rodell. 2016) available from https://disc.gsfc.nasa.gov/datasets/GLDAS_NOAH10_M_V2.1/summary?keywords=GLDAS. In addition, maximum rooting depth data (Fan et al., 2017) are also used in this study for investigating favourable factors for developing significant θ-Ta coupling, which were downloaded from https://wci.earth2observe.eu/thredds/catalog/usc/root-depth/catalog.html. All data are used at a 1° × 1° spatial resolution (original spatial resolution of the downloaded maximum rooting depth data is 1/120° × 1/120°, which has been averaged over each 1° × 1° grid cell). As the available GRACE TWS data are from April 2002 to January 2017, we set the study period as 2003–2016. Seventeen months of missing TWS data (June 2003, January 2011, June 2011, May 2012, October 2012, March 2013, August 2013, September 2013, February 2014, July 2014, December 2014, June 2015, October 2015, November 2015, April 2016, September 2016, and October 2016) are filled with linear interpolation using the months either side (Long et al., 2015; Andrew et al., 2017a; Andrew et al., 2017b). The temporal anomalies of all monthly variables are calculated and used in the analyses in this study, and the seasonal cycle has been removed from all these time series.

4.2.2 Wavelet decomposition

GRACE TWS reflects the monthly changes of total water storage, including surface water, soil moisture, groundwater, and snow and ice. Andrew et al. (2017a) developed an approach to “split” GRACE TWS into shallow and deep subsurface storage components by using a discrete wavelet decomposition. Following this approach, GRACE TWS data in this study are decomposed into “approximation” and “detail” components by using the “wavdec” function in MATLAB. The Meyer wavelet is applied here, because it has a scaling function for the numerical implementation of the multi-resolution analysis and can assure the smoothness of the reconstructed signal (Martínez and Gilabert, 2009; He and Guan, 2013). The resulting time series are labelled as A1, A2, A3, A4, and D1, D2, D3, D4 for approximation and detail components, respectively. The sum of an approximate series and corresponding detail components recovers the raw signal (e.g., D1 + D2 + D3 + D4 + A4 = raw signal; D1 + D2 + A2 = raw signal). Each decomposed component represents a certain time scale:

D1 (2-month scale), D2 (4-month scale), D3 (8-month scale), and A4 and D4 (⩾ 16-month scale) (see Figure 4.2). The decomposed TWS components reflect dynamics of terrestrial water storage components. Deep soil moisture and groundwater, as well as groundwater-connected large lakes and snowpack in cold climates, respond more slowly to the climate system and have much longer residence time than shallow soil moisture.

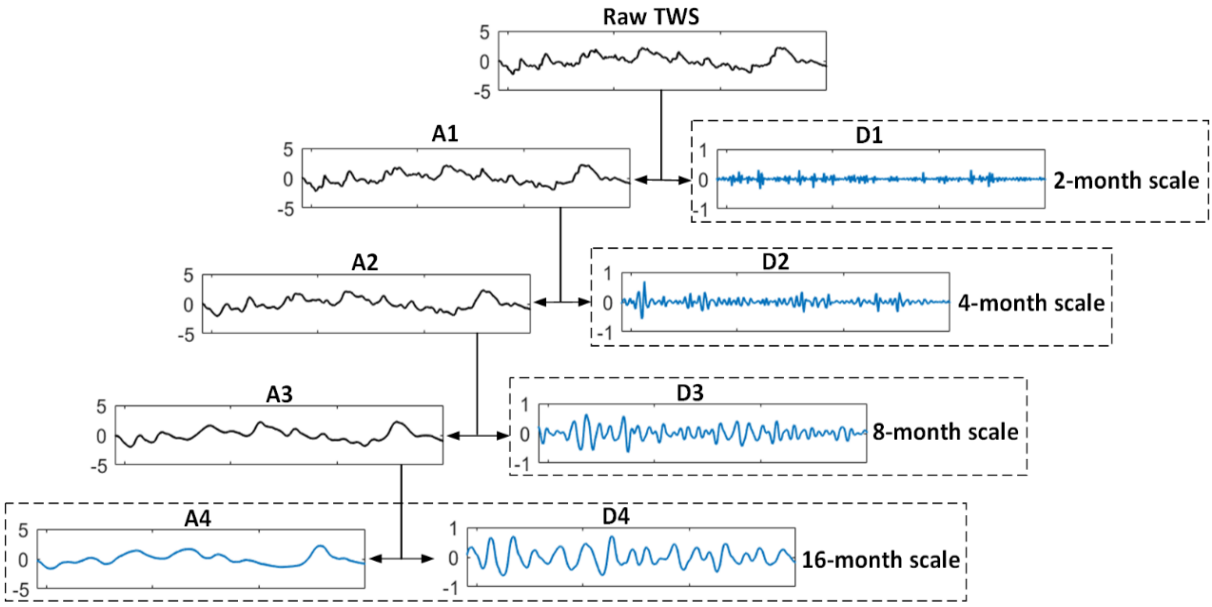

Figure 4.2 The structure of a discrete wavelet decomposition (an example from a grid cell in Australia (30.5 S, 130.5 E)).

4.2.3 Statistical analysis and significance test

Linear correlation is applied to examine relationships between air temperature and any a potential influencing (predictor) variable. Stepwise multiple linear regression is applied to determine the relative importance of different predictor variables in explaining the dependent variable (Draper and Smith, 1998; Clow, 2010), where the bidirectional elimination combining forward selection and backward elimination is adopted to determine the final regression model (Wang et al., 2016). The statistical significance of the regression model is assessed by an F test. The percentage of contribution of the final chosen variables to the change of air temperature can be revealed through the coefficient of determination (R^2). In addition, the adjusted $R^2$is also applied in this study to test whether the correlation between air temperature and terrestrial water storage improves by using decomposed TWS signals. The adjusted R^2considers and corrects for additional degrees of freedom, which are introduced by adding extra variables to a statistical model.

The *t* test statistic is applied in this study to judge the statistical significance of the correlation coefficient *r* between different time series, which is determined by:

$$t = \frac{r}{\sqrt{(1-r^2)/(N_{eff}-2)}}, \quad (4\text{-}1)$$

where N_{eff} is the effective sample size considering the autocorrelation of the time series. The effective sample size N_{eff} is estimated by Bretherton et al., (1999):

$$N_{eff} = N\frac{1-r_1 r_2}{1+r_1 r_2}, \quad (4\text{-}2)$$

where *N* is the sample size and r_1 and r_2 are the 1-month lag autocorrelations of the two involved time series. The thresholds for significant *p* values are adjusted to control the False Discovery Rate, which is applied to correct the effects of simultaneous multiple test results. α_{FDR} is the chosen control level for the False Discovery Rate. Wilks (2016) suggested that the usual strong spatial correlation encountered in gridded atmospheric data could choose $\alpha_{FDR} = 2\alpha_{global}$ (α_{global} = 0.05, the global test level). $\alpha_{FDR} = 2\alpha_{global}$=0.1 is applied in this study.

4.3 Results and Discussion

4.3.1 Sensitive regions of θ-Ta coupling based on monthly temperature anomaly

The correlation coefficients between monthly Ta and P, θs, θm, TWS anomalies are compared in Figures 4.3 (a–d). Among all soil moisture proxies, P shows significant negative correlation with Ta over the largest land area (37.8% of the grid cells). It is superior to other variables in North America and Eurasia (Figure 4.3 (a)). θs exhibits very weak correlation with Ta (Figure 4.3 (b)) at monthly scale, because the effect of a wetting event on surface 2-cm soil does not last beyond a few days, leaving little trace in monthly temperature. θm (Figure 4.3 (c)) and GRACE TWS (Figure 4.3 (d)) show significant negative correlation with Ta for 28.8% and 20.5% grid cells, respectively. The spatial distributions of θ-Ta coupling revealed by θm and TWS roughly match each other. These two soil moisture proxies show more significant negative correlation with Ta than P in the southern tip of Africa, and the northern area of Australia. In these regions, root-zone soil moisture is likely the dominant contributing factor for the θ-Ta coupling rather than precipitation or moisture in the surface soil layer.

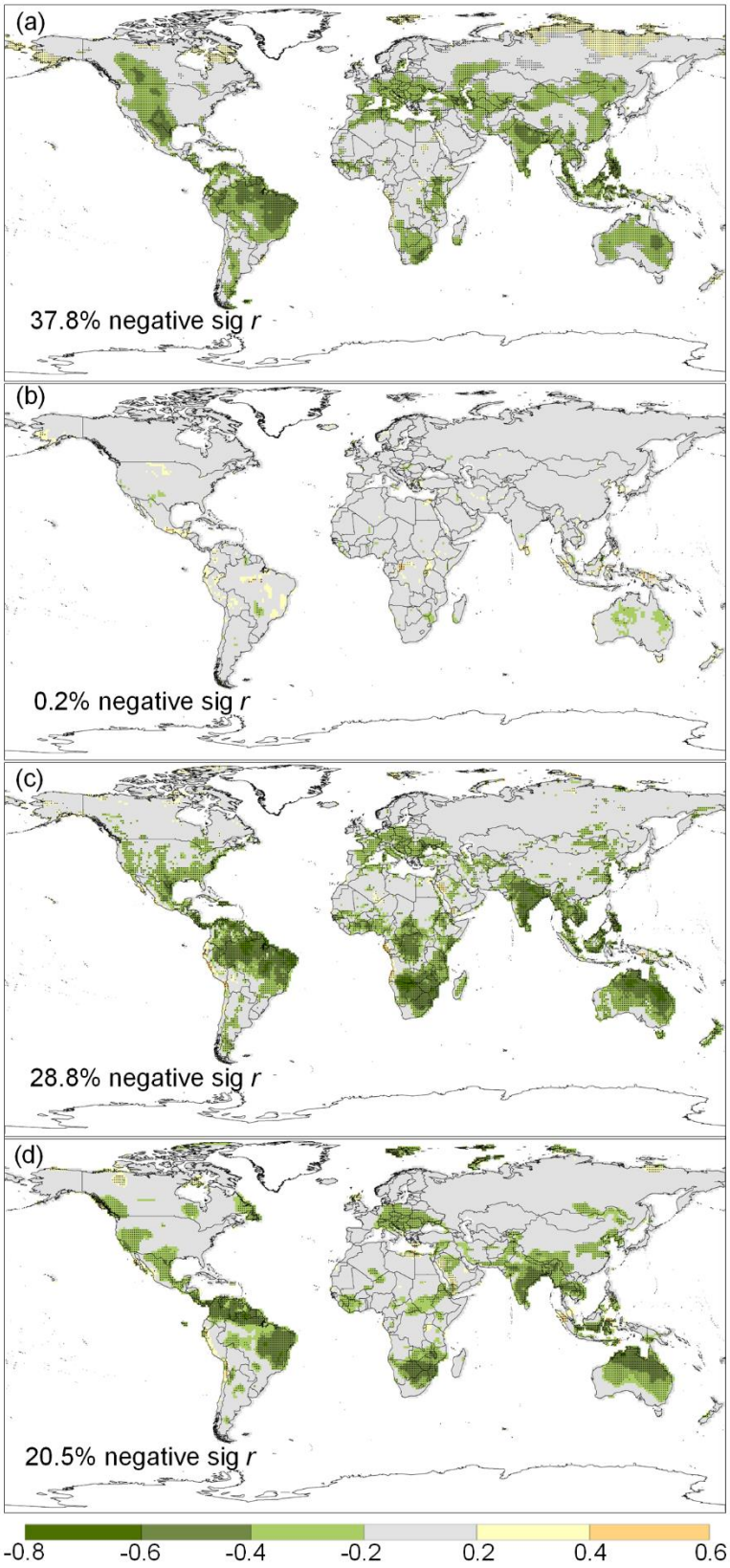

Figure 4.3 Correlation coefficients (*r*) between Ta and (a) P; (b) θs; (c) θm; and (d) TWS anomalies. Dots indicate that the corresponding *r* has passed the significance test (the threshold for significant *p* values has been adjusted to control the False Discovery Rate following Wilks, 2016). White land masses indicate areas where data are not available.

Sensitive regions of θ-Ta coupling based on monthly temperature anomaly and GRACE TWS identified in this study include the western region of North America, the northern and eastern regions of South America, the southern area of Europe, the southern tip of Africa, South Asia, the northwestern and central areas of Southeast Asia and north of the Tropic of Capricorn in Australia (Figure 4.3 (d)). Although these sensitive regions broadly match with what has been previously reported, differences exist among sensitive regions of θ-Ta coupling under average versus extreme hot conditions. For example, in the southern area of South America soil moisture interacts more intensely with hot extremes (Mueller and Seneviratne, 2012; Hirschi et al., 2014), but in South Asia it shows a stronger impact on monthly temperature anomaly (Figure 4.3 (d)).

Why does significant θ-Ta coupling occur in those sensitive regions shown in Figure 4.3, but not elsewhere? Conceptually, land surface temperature bridges the coupling between soil moisture and air temperature (Figure 4.1). Examination of θ-Ts and Ts-Ta relationships may tell the story. Figure 4.4 shows the correlation between Ts and Ta, θs, θm, and TWS anomalies. Globally, Ts and Ta are well correlated, except for some tropical areas (Figure 4.4 (a)). The weak correlation between Ts and θs explains the low coupling of surface soil moisture and monthly air temperature (Figure 4.3 (b)). Ts and TWS correlation spatially matches that of Ts and θm (Figure 4.4 (d) vs. Figure 4.4 (c)). Comparing Figures 4.3 and 4.4 we see that the significant θ-Ta coupling only occurs when both θ-Ts and Ts-Ta relationships are strong. Given the general strong Ts-Ta correlation globally (Figure 4.4 (a)), it is clear that the sensitive θ-Ta coupling at the monthly scale is primarily constrained by the connection between root zone moisture and land surface temperature.

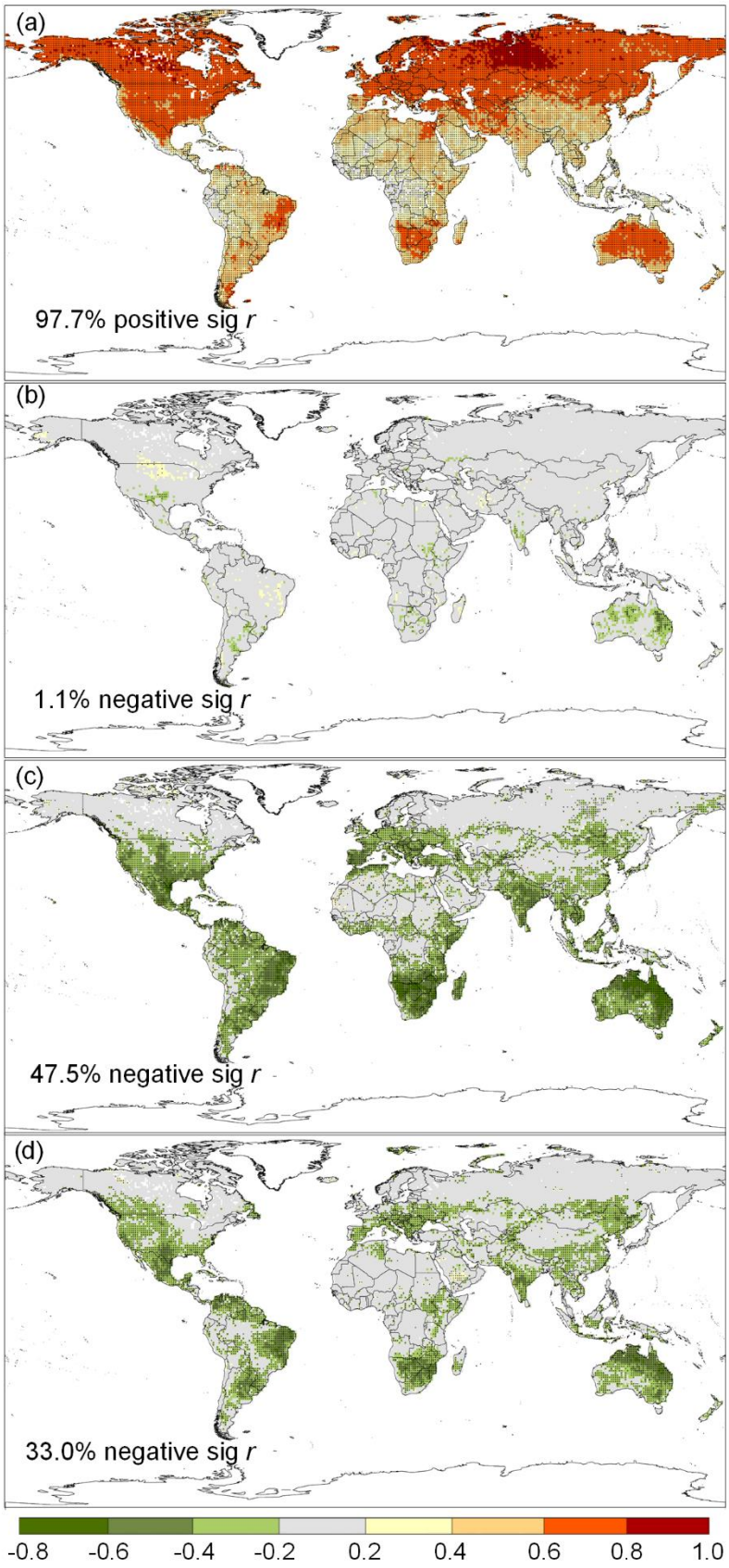

Figure 4.4 As in Figure 4.3 but for correlation coefficients (*r*) between Ts and (a) Ta; (b) θs; (c) θm; and (d) TWS anomalies.

4.3.2 Skill of GRACE TWS data in examining θ-Ta coupling

After being decomposed by wavelet method, the skill of GRACE TWS in examining the variability of monthly Ta increased for 89.5% of the grid cells showing significant TWS-Ta correlation (Figure 4.3 (d)), which is tested by the adjusted R^2. Areas with significant negative *r* between Ta and decomposed TWS components are shown in Figure 4.5. Among all time scales, the identified sensitive regions of θ-Ta coupling are mostly consistent with spatial patterns of D4 and A4, which implies that the moisture content at deeper soil depths plays an important role in θ-Ta coupling through plant transpiration, such as in the tropics where soil moisture contributes more than surface water to monthly and seasonal variations of total water storage (Güntner et al., 2007). In the central region of Africa and some regions located around China, seasonal variability (D1–D3) seems to be more important than interannual variability (D4 and A4). Strong correlation between air temperature and lowest frequency of TWS variability also implies the need of future investigation on the relationship between groundwater dependent ecosystems and air temperature for further information of land surface atmosphere coupling.

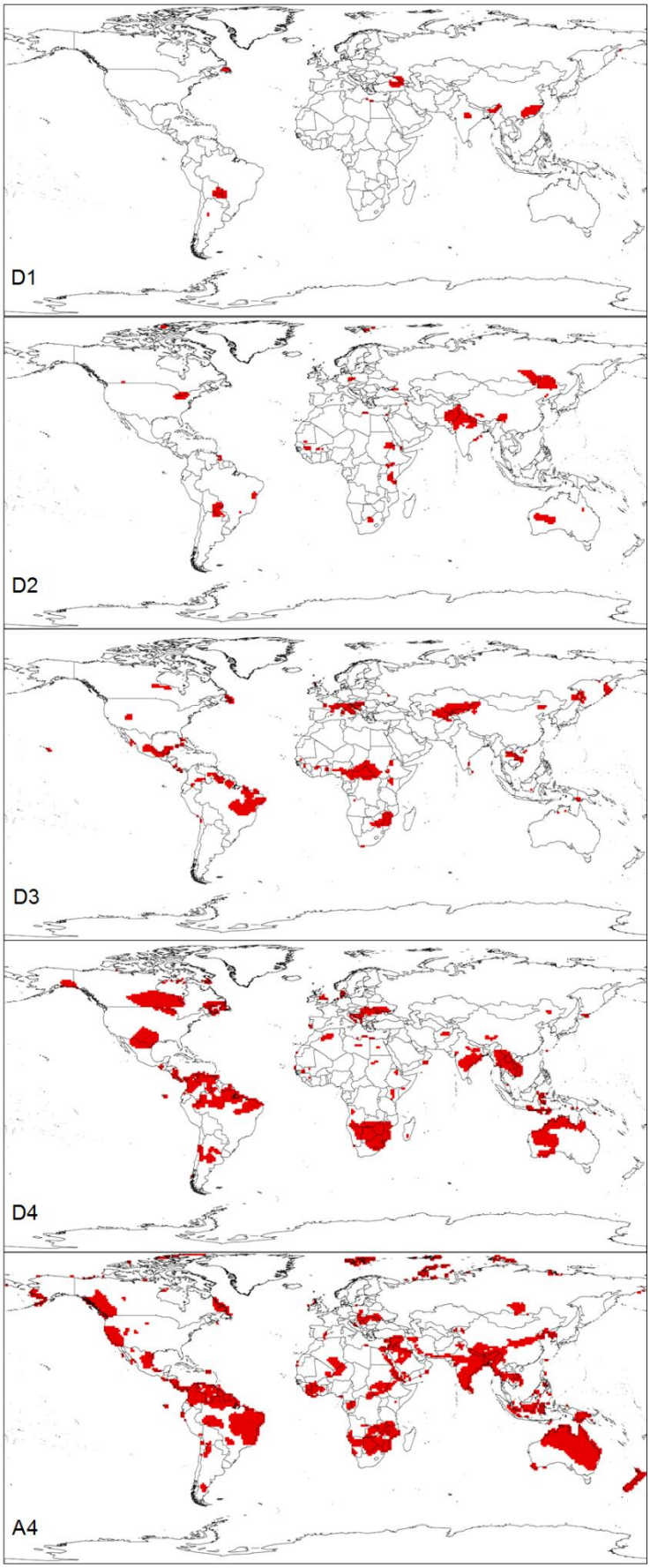

Figure 4.5 Areas where significant negative r exists between Ta and wavelet decomposition level D1, D2, D3, D4, and A4 of TWS.

From Figures 4.3 (a) and (d) we can see that P performs better in North America, while TWS performs better in Australia and the southern tip of Africa. As these two variables may complement each other in explaining the temporal variability of Ta, the total explanatory power of P and TWS is worth being investigated. As the explanatory power of raw TWS is underestimated, decomposed TWS components are used here to be considered together with P as candidate predictor variables in the stepwise regression analysis to identify the dominant explanatory factors for Ta in each grid cell.

Figure 4.6 (a) shows how much variability of Ta can be explained by P, and Figure 4.6 (b) exhibits the total contribution of the dominant influencing factors selected among P and decomposed TWS, expressed by the R^2. The global average R^2 of combined P and TWS is more than twice that of the individual P, indicating the remarkably improved explanatory power, especially in some sensitive regions including the northern and eastern regions of South America, southern tip of Africa, South Asia, Southeast Asia, and north of the Tropic of Capricorn in Australia. The decomposed TWS variables kept in the final regression model are shown in Figure 4.7 where the spatial patterns generally match with that of significant negative correlations between Ta and decomposed TWS components shown in Figure 4.5. The explanatory power of selected variables (P, raw TWS, decomposed TWS, and the combination of them) over the globe is assessed in Figure 4.8. Where the coupling is stronger (as indicated by the increased R^2), the role of GRACE TWS and its decompositions become more important. For areas with a regression R2larger than 25%, the explanatory power follows an order as P < TWS < Decomposed TWS < Combination of P and decomposed TWS. The combination of P and decomposed TWS performs better than any separate one of them in examining the θ-Ta coupling.

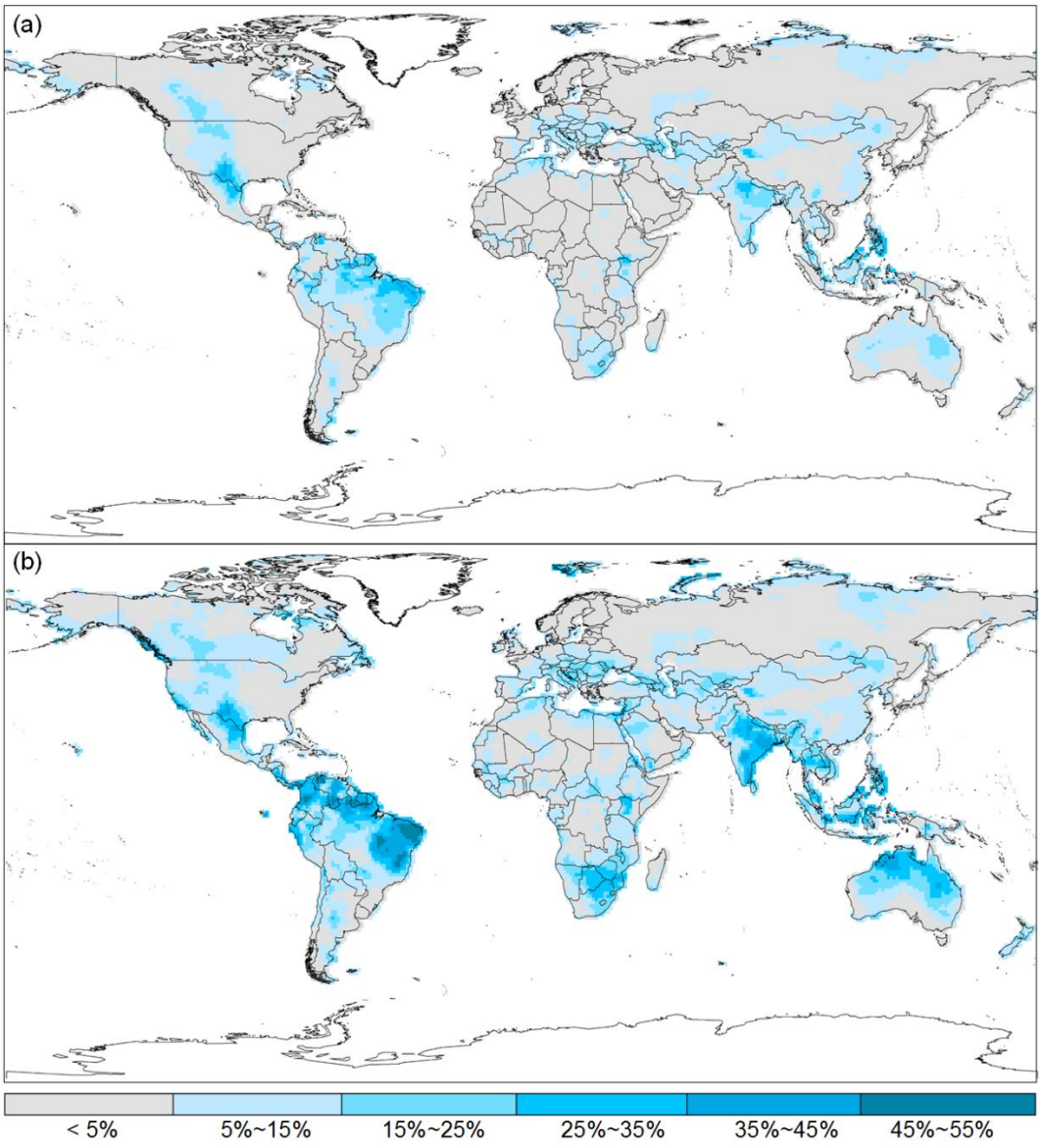

Figure 4.6 Percentage of Ta variability (inferred from regression R^2) explained (a) by P; and (b) by a combination of P and decomposed TWS.

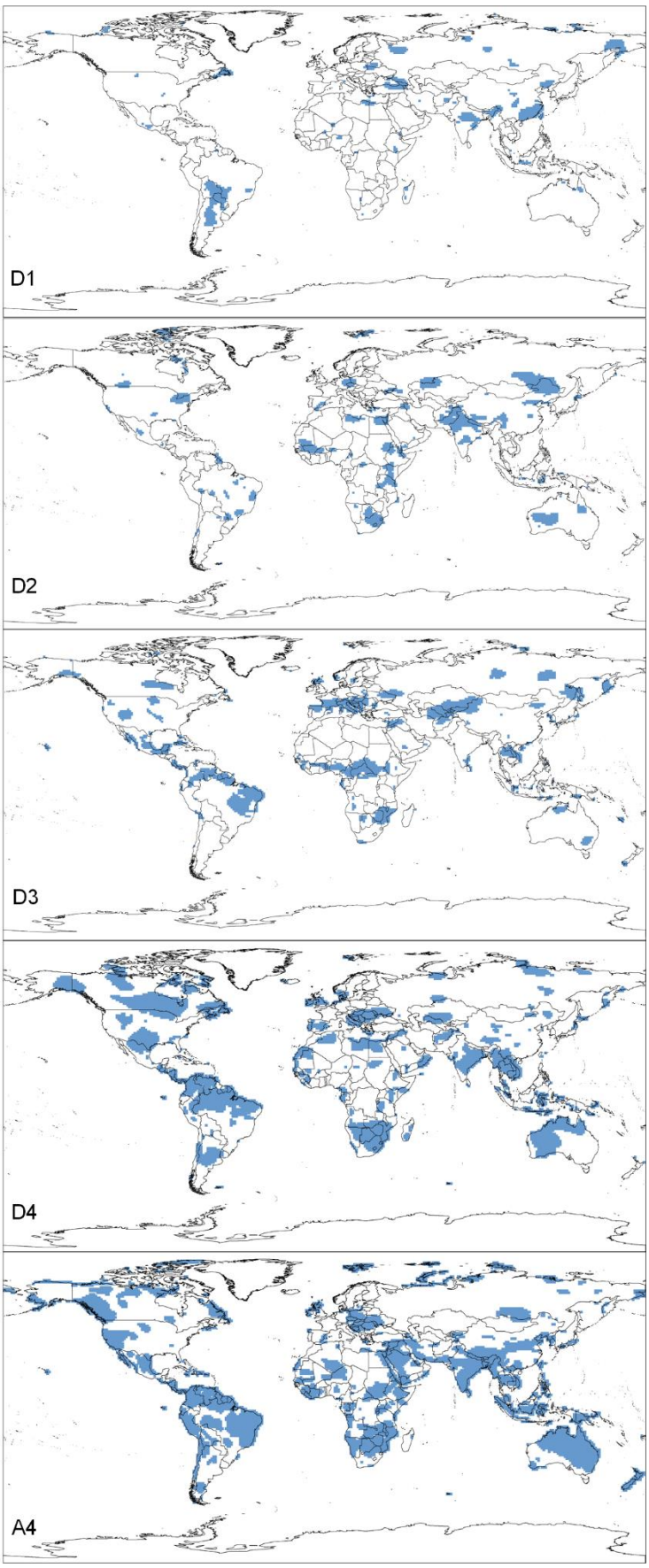

Figure 4.7 Areas where decomposed TWS components (D1–A4) are kept in the final regression model for explaining Ta variability by combined precipitation and decomposed TWS.

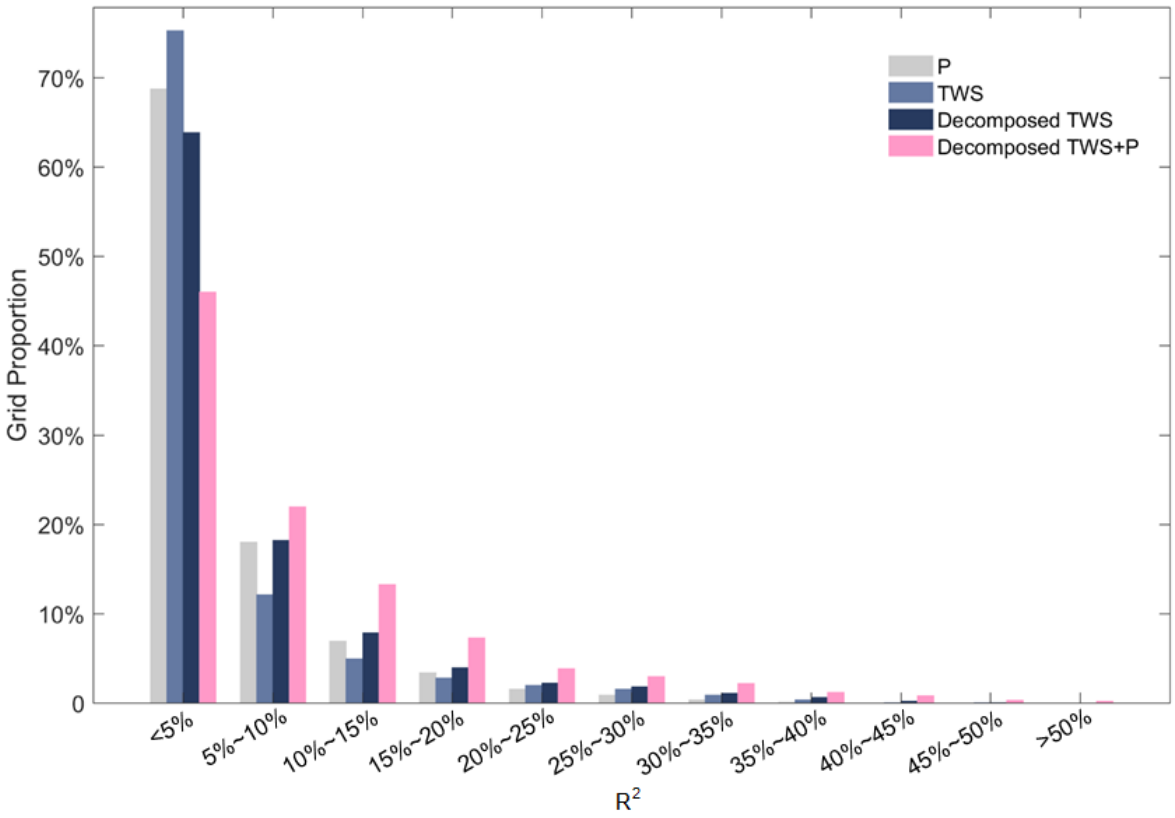

Figure 4.8 Explanatory power (represented by regression R^2) for Ta variability by using precipitation (P), terrestrial water storage (TWS), TWS decomposed signals (Decomposed TWS), and the combination of precipitation and decomposed TWS.

4.3.3 Favourable factors for developing significant monthly θ-Ta coupling

From the global spatial distribution of maximum rooting depth (Figure 4.9 (a)) we can see that almost all identified sensitive regions have a deep - rooting system. In addition, significant areas of D3, D4, and A4 (Figure 4.5), representing larger time scales, generally have deeper rooting systems. This is consistent with the notion in Andrew et al. (2017a) that deep soil moisture tends to have more contribution from low-frequency components of TWS wavelet decompositions. In addition to root-zone soil moisture, a climate with clear dry and wet season alternation may be another determining factor for θ-Ta coupling. For example, precipitation in the Indian subcontinent (Rana et al., 2015) and water storage in Amazon floodplain (Alsdorf et al., 2000) are revealed to have obvious seasonality, where significant θ-Ta coupling occurs (Figure 4.6 (b)).

The spatial patterns of Figures 4.6 (b) and Figure 4.9 exhibit that most identified sensitive regions show relatively deeper rooting system and larger precipitation seasonality index. Such relationship is examined again in Figure 4.10, where maximum rooting depth and precipitation

seasonality index are categorized by the total explanatory power of P combined with decomposed TWS. Both maximum rooting depth and precipitation seasonality index show positive correlation with the regression R^2. But this relationship does not hold when precipitation seasonality index is smaller than 0.2 (likely too wet), or larger than 0.8 (too dry). In these cases, the regression R^2 is very low. For example, the grid cells with precipitation seasonality index larger than 0.8 mostly distributed in the Sahara Desert, where little vegetation occurs (Figure 4.9). Deep-rooting systems together with strong precipitation seasonality usually lead to high-regression R^2 indicating that both of them are favourable for developing significant monthly θ-Ta coupling.

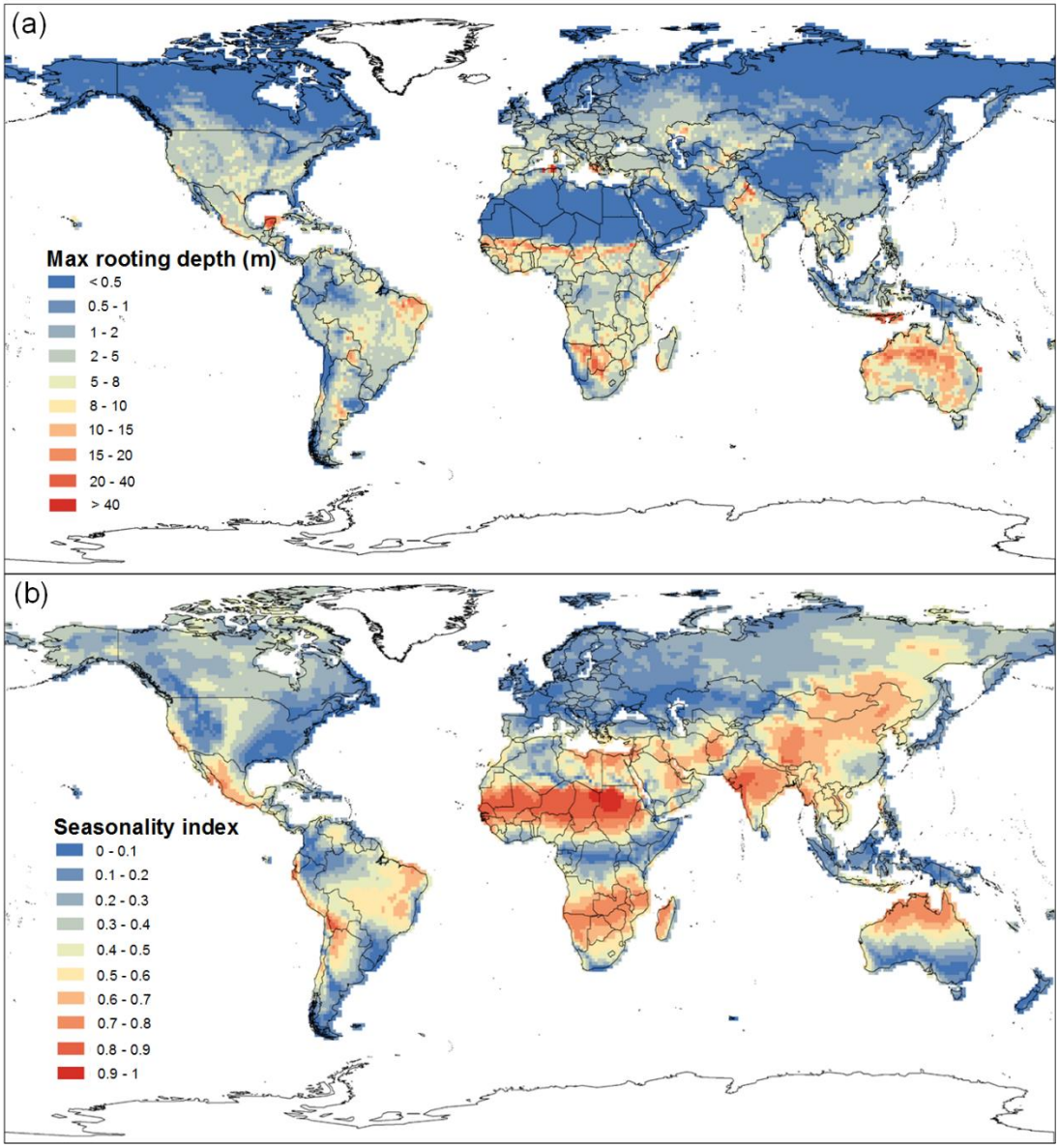

Figure 4.9 Global distributions of (a) maximum rooting depth (Fan et al. 2017); (b) precipitation seasonality (calculated based on the equation provided in Dingman, S. L. Physical hydrology-2nd ed, 2002, 143-145).

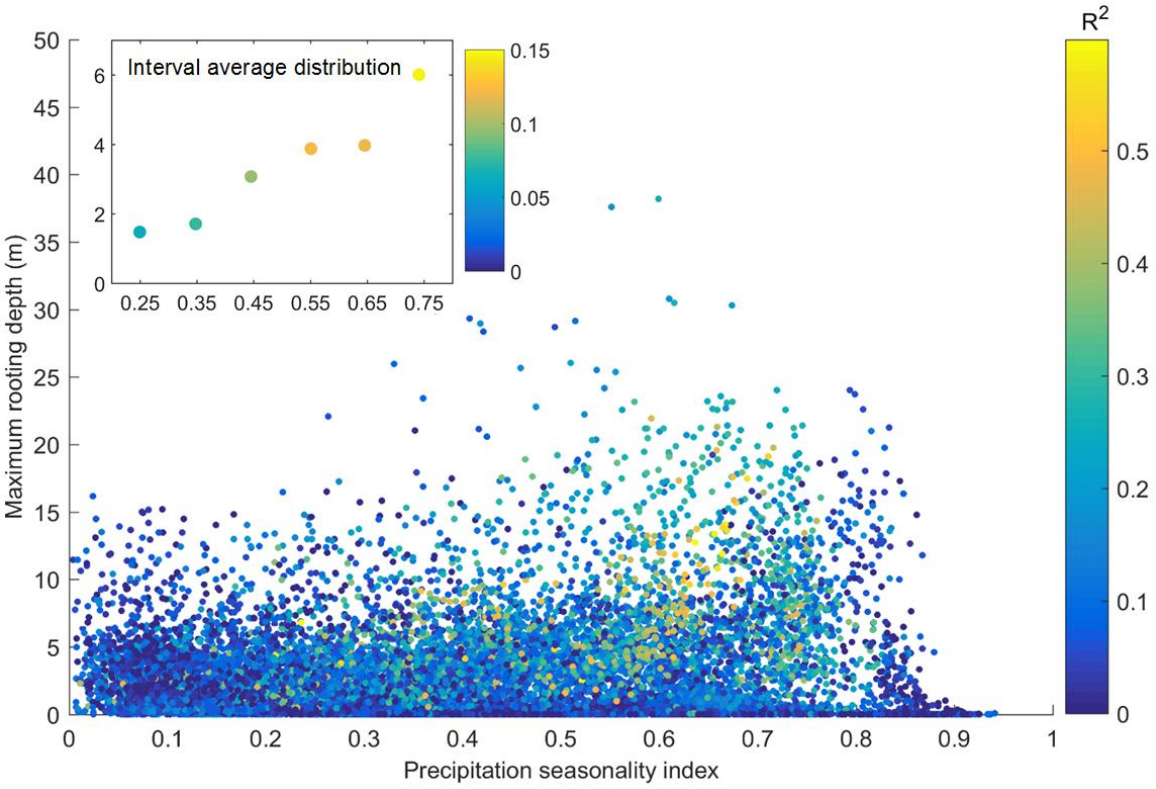

Figure 4.10 Scatter of maximum rooting depth and precipitation seasonality index categorized by regression R^2 (shown in Figure 4.6 (b)). The corresponding interval average distribution is shown in the upper left. The *x* axis is the interval average precipitation seasonality index, the *y* axis and colorbar indicate the average maximum rooting depth and average R^2 of those grid cells within each interval of precipitation seasonality index.

4.4 Conclusions

Understanding global θ-Ta coupling is needed to improve the representation of land-atmosphere interactions in Earth system models. In this study, global θ-Ta coupling is examined based on monthly air temperature anomalies and soil moisture proxies (i.e., P, θs, θm, and TWS). Compared with precipitation, remote sensing surface soil moisture and land-surface model derived soil moisture, GRACE TWS data are shown to be skillful in examining global θ-Ta coupling. After wavelet decomposition, the skill of TWS for explaining monthly Ta variability further improves. Furthermore, combining decomposed TWS and precipitation data yields higher correlation with air temperature than each of the two variables separately, probably because they respectively represent the hydrological and meteorological part of land-atmosphere coupling. The θ-Ta coupling in the areas with deeper rooting systems, such as the southern tip of Africa and north of the Tropic of Capricorn in Australia, are more likely to be revealed by GRACE TWS, where the skill of

precipitation is weaker. The identified sensitive areas for θ-Ta coupling are mainly constrained by the connection of root zone soil moisture and land surface temperature. It is suggested that the areas with both deep-rooting plants and clear dry-wet seasonality are more likely to develop significant monthly θ-Ta coupling.

4.5 References

Alexander, L. 2011. Climate science: Extreme heat rooted in dry soils. Nature Geoscience. 4(1), 12–13.

Alsdorf, D. E., Melack, J. M., Dunne, T., Mertes, L. A. K., Hess, L. L., Smith, L. C. 2000. Interferometric radar measurements of water level changes on the Amazon flood plain. Nature, 404(6774), 174–177.

Andersen, O. B., Seneviratne, S. I., Hinderer, J., Viterbo, P. 2005. GRACE‐derived terrestrial water storage depletion associated with the 2003 European heat wave. Geophysical Research Letters. 32, L18405.

Andrew, R. A., Guan, H., Batelaan, O. 2017a. Estimation of GRACE water storage components by temporal decomposition. Journal of Hydrology, 552, 341–350.

Andrew, R. A., Guan, H., Batelaan, O. 2017b. Large-scale vegetation responses to terrestrial moisture storage changes. Hydrology and Earth System Sciences. 21, 4469–4478.

Beaudoing, H. and Rodell, M. NASA/GSFC/HSL. 2016. GLDAS Noah land surface model L4 3 hourly 1.0 × 1.0 degree, V2.1, Greenbelt, Maryland, USA, Goddard Earth Sciences Data and Information Services Center (GES DISC). https://doi.org/10.5067/IIG8FHR17DA9.

Berg, A., Lintner, B. R., Findell, K. L., Malyshev, S., Loikith, P. C., Gentine, P. 2014. Impact of soil moisture-Atmosphere interactions on surface temperature distribution. Journal of Climate. 27, 7976–7993.

Black, E. and Sutton, R. 2006. The influence of oceanic conditions on the hot European summer of 2003. Climate Dynamics. 28, 53–66.

Bretherton, C. S., Widmann,M., Dymnikov, V. P., Wallace, J. M., Blade, I. 1999. The effective number of spatial degrees of freedom of a time-varying field. Journal of Climate. 12(7), 1990–2009.

Clow, D. W. 2010. Changes in the timing of snowmelt and streamflow in Colorado: A response to recent warming. Journal of Climate. 23(9), 2293–2306.

Cubasch, U., Meehl, G. A., Boer, G. J., Stouffer, R. J., Dix, M. R., Noda, A., et al. 2001. Projections of future climate changes. In Climate Change 2001: The Scientific Basis. Contribution of Working Group I to the Third Assessment Report of the Intergovernmental Panel on Climate Change, (pp. 525–582). Cambridge: Cambridge University Press.

Dee, D. P., Uppala, S. M., Simmons, A. J., Berrisford, P., Poli, P., Kobayashi, S., et al. 2011. The ERA‐Interim reanalysis: Configuration and performance of the data assimilation system. Quarterly Journal of The Royal Meteorological Society, 137(656), 553–597.

Dorigo, W. A., Wagner, W., Albergel, C., Albrecht, F., Balsamo, G., Brocca, L., et al. 2017. ESA CCI Soil Moisture for improved Earth system understanding: State-of-the art and future directions. Remote Sensing of Environment. 203, ISSN 0034-4257, 185–215.

Draper, N. R. and Smith, H. 1998. Applied regression analysis. Hoboken, N. J: Wiley Interscience.

Durre, I., Wallace, J. M., Lettenmaier, D. P. 2000. Dependence of extreme daily maximum temperatures on antecedent soil moisture in the contiguous United States during summer. Journal of Climate. 13, 2641–2651.

Fan, Y., Miguez-Macho, G., Jobbágy, E. G., Jackson, R. B., Otero‐Casal, C. 2017. Hydrologic regulation of plant rooting depth. Proceedings of the National Academy of Sciences. 201712381.

Fischer, E. M., Seneviratne, S. I., Vidale, P. L., Lüthi, D., Schär, C. 2007. Soil moisture-atmosphere interactions during the 2003 European summer heatwave. Journal of Climate. 20, 5081–5099.

Getirana, A. 2016. Extreme water deficit in Brazil detected from space. Journal of Hydrometeorology. 17, 591–599.

Gevaert, A. I., Miralles, D. G., de Jeu, R. A. M., Schellekens, J., Dolman, A. J. 2017. Soil moisture-temperature coupling in a set of land surface models. Journal of Geophysical Research-Atmospheres. 123, 1481–1498.

Gruber, A., Dorigo, W. A., Crow, W., Wagner, W. 2017. Triple collocation‐based merging of satellite soil moisture retrievals. IEEE Transactions on Geoscience and Remote Sensing. 1–13.

Güntner, A., Stuck, J., Werth, S., Döll, P., Verzano, K., Merz, B. 2007. A global analysis of temporal and spatial variations in continental water storage. Water Resources Research. 43, W05416.

He, X. and Guan, H. 2013. Multiresolution analysis of precipitation teleconnections with large‐scale climate signals: A case study in South Australia. Water Resources Research. 49, 6995–7008.

Hirschi, M., Mueller, B., Dorigo, W., Seneviratne, S. I. 2014. Using remotely sensed soil moisture for land-atmosphere coupling diagnostics: The role of surface vs. root-zone soil moisture variability. Remote Sensing of Environment. 154, 246–252.

Hirschi, M., Seneviratne, S. I., Alexandrov, V., Boberg, F., Boroneant, C., Christensen, O. B., et al. 2011. Observational evidence for soilmoisture impact on hot extremes in southeastern Europe. Nature Geoscience. 4(1), 17–21.

Humphrey, V., Gudmundsson, L., Seneviratne, S. I. 2016. Assessing global water storage variability from GRACE: Trends, seasonal cycle, subseasonal anomalies and extremes. Surveys in Geophysics. 37, 357–395.

Jaeger, E. and Seneviratne, S. 2011. Impact of soil moisture‐atmosphere coupling on European climate extremes and trends in a regional climate model. Climate Dynamics, 36(9), 1919–1939.

Koster, R. D., Sud, Y. C., Guo, Z. C., Dirmeyer, P. A., Bonan, G., Oleson, K. W., et al. 2006. GLACE: The Global Land-Atmosphere Coupling Experiment. Part I: Overview. Journal of Hydrometeorology, 7(4), 590–610.

Landerer, F. W. and Swenson, S. C. 2012. Accuracy of scaled GRACE terrestrial water storage estimates. Water Resources Research. 48, W04531.

Liu, Y. Y., Dorigo, W. A., Parinussa, R. M., de Jeu, R. A. M., Wagner, W., McCabe, M. F., et al. 2012. Trend‐preserving blending of passive and active microwave soil moisture retrievals. Remote Sensing of Environment. 123, 280–297.

Long, D., Yang, Y., Wada, Y., Hong, Y., Liang, W., Chen, Y., Chen, L. 2015. Deriving scaling factors using a global hydrological model to restore GRACE signals. Remote Sensing of Environment. 168, 177–193.

Lorenz, R., Jaeger, E. B., Seneviratne, S. I. 2010. Persistence of heat waves and its link to soil moisture memory. Geophysical Research Letters. 37, L09703.

Lorenz, R., Pitman, A. J., Hirsch, A. L. 2015. Intraseasonal versus interannual measures of land-atmosphere coupling strength in a global climate model: GLACE-1 versus GLACE-CMIP5 experiments in ACCESS1.3b. Journal of Hydrometeorology. 16, 2276–2295.

Miralles, D., van den Berg, M., Teuling, A., de Jeu, R. 2012. Soil moisture‐temperature coupling: A multiscale observational analysis. Geophysical Research Letters. 39, L21707.

Martínez, B. and Gilabert, M. A. 2009. Vegetation dynamics from NDVI time series analysis using the wavelet transform. Remote Sensing of Environment. 113, 1823–1842.

Mueller, B. and Seneviratne, S. I. 2012. Hot days induced by precipitation deficits at the global scale. Proceedings of the National Academy of Sciences. 109(31), 12,398–12,403.

Perkins, S. E., Argüeso, D., White, C. J. 2015. Relationships between climate variability, soil moisture, and Australian heatwaves. Journal of Geophysical Research-Atmospheres. 120, 8144–8164.

Ramillien, G., Famiglietti, J. S., Wahr, J. 2008. Detection of continental hydrology and glaciology signals from GRACE: A review. Surveys in Geophysics. 29(4–5), 361–374.

Rana, S., McGregor, J., Renwick, J. 2015. Precipitation seasonality over the Indian subcontinent: An evaluation of gauge, reanalyses, and satellite retrievals. Journal of Hydrometeorology. 16, 631–651.

Rodell, M., Houser, P. R., Jambor, U., Gottschalck, J., Mitchell, K., Meng, C., et al. 2004. The global land data assimilation system. Bulletin of the American Meteorological Society. 85(3), 381–394.

Schneider, U., Becker, A., Finger, P., Meyer‐Christoffer, A., Rudolf, B., Ziese, M. 2015. GPCC full data monthly product version 7.0 at 1.0°: Monthly land‐surface precipitation from rain‐gauges built on GTS-based and historic data. https://doi.org/10.5676/DWD_GPCC/FD_M_V7_100.

Schwingshackl, C., Hirschi, M., Seneviratne, S. I. 2017. Quantifying spatiotemporal variations of soil moisture control on surface energy balance and near-surface air temperature. Journal of Climate. 30(18), 7105–7124.

Seneviratne, S. I., Corti, T., Davin, E. L., Hirschi, M., Jaeger, E. B., Lehner, I., et al. 2010. Investigating soil moisture - climate interactions in a changing climate: A review. Earth-Science Reviews, 99, 125–161.

Seneviratne, S. I., Koster, R. D., Guo, Z., Dirmeyer, P. A., Kowalczyk, E., Lawrence, D., et al. 2006. Soil moisture memory in AGCM simulations: Analysis of Global Land-Atmosphere Coupling Experiment (GLACE) data. Journal of Hydrometeorology. 7(5), 1090–1112.

Seneviratne, S. I., Wilhelm, M., Stanelle, T., Hurk, B., Hagemann, S., Berg, A., et al. 2013. Impact of soil moisture-climate feedbacks on CMIP5 projections: First results from the GLACE-CMIP5 experiment. Geophysical Research Letters. 40, 5212–5217.

Sinha, D., Syed, T. H., Famiglietti, J. S., Reager, J. T., Thomas, R. C. 2017. Characterizing drought in India using GRACE observations of terrestrial water storage deficit. Journal of Hydrometeorology. 18, 381–396.

Swenson, S.C. 2012. GRACE monthly land water mass grids NETCDF RELEASE 5.0. Ver. 5.0. PO.DAAC, CA, USA. Dataset accessed at https://doi.org/10.5067/TELND - NC005.

Swenson, S. C. and Wahr, J. 2006. Post-processing removal of correlated errors in GRACE data. Geophysical Research Letters. 33, L08402.

Thomas, A. C., Reager, J. T., Famiglietti, J. S., Rodell, M. 2014. A GRACE - based water storage deficit approach for hydrological drought characterization. Geophysical Research Letters. 41, 1537–1545.

Vogel, M. M., Orth, R., Cheruy, F., Hagemann, S., Lorenz, R., Hurk, B., Seneviratne, S. I. 2016. Regional amplification of projected changes in extreme temperatures strongly controlled by soil moisture-temperature feedbacks. Geophysical Research Letters. 44,1511–1519.

Wan, Z., Hook, S. and Hulley, G. 2015. MOD11C3 MODIS/Terra Land surface temperature/emissivity monthly L3 global 0.05deg CMG V006 [Data set]. NASA EOSDIS LP DAAC. https://doi.org/10.5067/MODIS/MOD11C3.006.

Wang, M., Wright, J., Brownlee, A., Buswell, R. 2016. A comparison of approaches to stepwise regression on variables sensitivities in building simulation and analysis. Energy and Buildings. 127, 313–326.

Whan, K., Zscheischler, J., Orth, R., Shongwe, M., Rahimi, M., Asare, E. O., Seneviratnec, S. I. 2015. Impact of soil moisture on extreme maximum temperatures in Europe. Weather and Climate Extremes. 9, 57–67.

Wilks, D. S. 2016. “The Stippling Shows Statistically Significant Grid Points”: How research results are routinely overstated and overinterpreted, and what to do about it. Bulletin of the American Meteorological Society. 97, 2263–2273.

Yang, Y., Long, D., Guan, H., Scanlon, B. R., Simmons, C. T., Jaing, L., Xu, X. 2014. GRACE satellite observed hydrological controls on interannual and seasonal variability in surface greenness over mainland Australia. Journal of Geophysical Research-Biogeosciences. 119, 2245–2260.

5 SPATIALLY DIFFERENTIATED EFFECTS OF LOCAL MOISTURE DEFICIT ON HOT EXTREMES IN COMPARISON TO GLOBAL TEMPERATURE CHANGE

5.1 Introduction

Hot extremes have become more frequent and intense across most land regions since the 1950s, which is in direct relation to global warming (IPCC, 2021). Antecedent surface moisture deficit exacerbates hot extremes as it can reduce evaporative cooling and increase atmospheric heating (Seneviratne, 2010; Alexander, 2011). Previous studies have investigated the effects of increasing global temperature (e.g., Rahmstorf and Coumoustudy, 2011; Perkins-Kirkpatrick and Gibson, 2017) and local soil moisture deficit (e.g., Herold et al. 2016; Vogel et al. 2017) on hot extremes separately, but the relative importance of the two influencing factors on hot extremes has not been compared. Such comparison study would contribute to developing practical advice to mitigating the negative impacts of hot extremes on the environment and society, given that human activities can modify global temperature change by reducing greenhouse gas emissions (the observed global warming is considered extremely likely associated with anthropogenic influences, particularly greenhouse gas emission (IPCC, 2013)) and address local moisture deficit by adaptive land management.

The standardised precipitation index (SPI) and modelling soil moisture products are commonly used in analysing the relationship between soil moisture and hot extremes in previous studies (e.g., Koster et al. 2006; Lorenz et al. 2010; Perkins et al. 2015). Mueller and Seneviratne (2012) were the first to assess the relationship between hot extremes and SPI (indicating precipitation deficit) at a global scale. Hirschi et al. (2014) used a merged active/passive microwave soil moisture product and model-derived soil moisture compared to SPI. They found that modelled soil moisture displayed a comparable coupling strength with hot extremes as the SPI-based analysis showed. The strength of the relationship appeared to be weaker when remotely sensed surface soil moisture was used.

The Gravity Recovery and Climate Experiment (GRACE) derived terrestrial water storage (TWS) provides data on water storage, including groundwater, soil moisture, surface water, snow, and ice. A discrete wavelet decomposition method is capable of partitioning the total water storage into shallow and deep components (Andrew et al. 2017a). Based on that approach, Andrew et al. (2017b) investigated large-scale vegetation responses to monthly moisture storage at different frequencies. They reported that grassland-dominated areas are more sensitive to higher

frequencies of moisture storage changes while plants with deeper rooting systems (e.g., forests) are more sensitive to moisture storage changes of longer time scales. In addition, Chen et al. (2019) reported that monthly air temperature anomalies show a stronger relationship with wavelet decomposed GRACE TWS than with raw TWS. Here, we compare decomposed GRACE TWS with SPI and model-derived soil moisture in examining the relationship between soil moisture and the number of hot days in the hottest month (θ-NHD relationship). As Mueller and Seneviratne (2012) suggested that NHD, as a percentile-based index, is more comparable than threshold-based indices across different climatic regions.

This study aims 1) to examine the θ-NHD relationship at a global scale using decomposed GRACE TWS, and based on the developed methodology; 2) to investigate the relative importance of global temperature change and local moisture deficit to the occurrence of hot extremes.

5.2 Methodology

5.2.1 NHD calculation and data sources

The number of hot days is defined as the number of days per specific time interval (e.g., month, season, year) with a surface air temperature at 2 m height above the 90th-percentile. In this study, the number of hot days in the hottest month (NHD) is examined based on the ECMWF reanalysis ERA-Interim daily maximum temperature data (Dee et al., 2011) from 1985 to 2015. A time window of five days centred on each day of the 31-year period is considered, so the 90th percentile is calculated from 155 daily values (Mueller and Seneviratne, 2012). The hottest month is determined for each grid cell based on the monthly average daily maximum temperature for the time series 1985–2015. Its geographical distribution is shown in Figure 5.1. Monthly latent heat flux and net radiation data used to calculate the evaporative fraction are also from ERA-Interim.

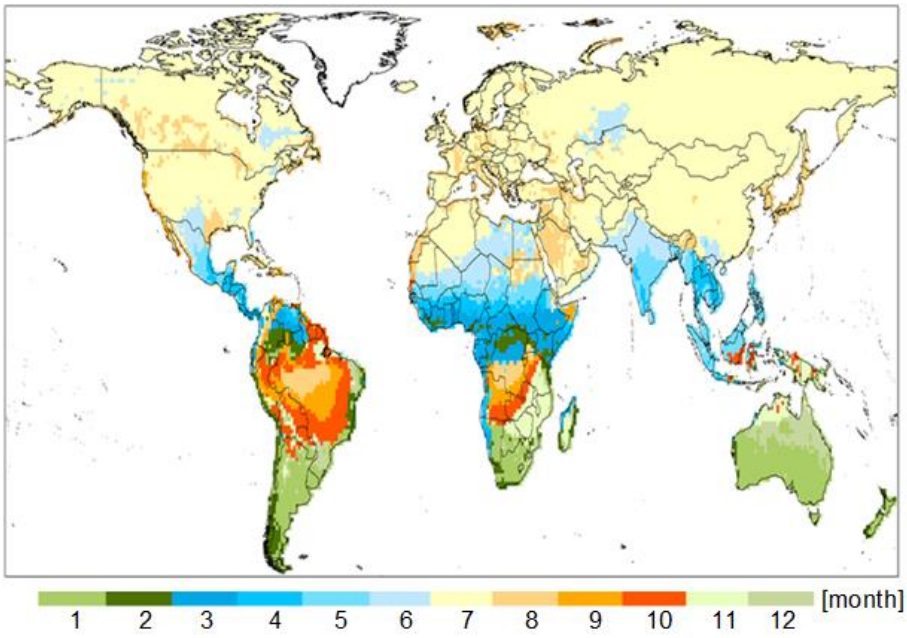

Figure 5.1 Geographical distribution of most frequently occurring hottest month for the period 1985–2015.

5.2.2 Global-mean temperature data

Annual global-mean land surface air temperature (Hansen et al., 2010) data are available from NASA Goddard Institute for Space Studies (GISS). It represents the global temperature change including both variability and trend of global-mean temperature.

5.2.3 Wavelet decomposed GRACE TWS data

A reconstructed GRACE TWS dataset (Humphrey et al. 2017) from 1985 to 2015 provided by the Institute for Atmospheric and Climate Science, Eidgenössische Technische Hochschule Zurich (IAC ETH) is applied in this study. GRACE TWS has been decomposed into “approximate” (A1, A2, A3, A4) and “detail” (D1, D2, D3, D4) components by a wavelet method following Andrew et al. (2017a). The structure of wavelet decomposition has been shown in Figure 4.2 of Chapter 4, taking a grid cell in Australia (30.5 S, 130.5 E) as an example. The sum of a series of approximate and the corresponding detail components equals to the raw signal (e.g., raw signal=D1+D2+A2=D1+D2+D3+A3). Each decomposition level represents a specific time scale: D1 (2-month), D2 (4-month), D3 (8-month), and A4 and D4 ($\geqslant$ 16-month). Those decomposed components of different temporal scales reflect temporal dynamics of moisture at different depths. This is based on the understanding that moisture at various soil depths has different response times to the climate system (Andrew et al. 2017a; Chen et al. 2019). Thus, it is possible that moisture storage with response timescales of several months could impact energy balance partitioning at the

land surface. The original GRACE TWS data from 2003 to 2016 (Watkins et al. 2015; Wiese et al. 2019) provided by the Jet Propulsion Laboratory (JPL) are also applied in this study. Although the data period is too short for reliable statistical analysis, it provides a comparison for the reconstructed GRACE TWS.

5.2.4 Soil moisture proxies

For relating the occurrence of hot extremes to soil moisture deficit, SPI (calculated from GPCC Reanalysis precipitation data, Schneider et al. 2015) and a land surface model derived soil moisture product (GLDAS_NOAH10_M.2.1, Rodell et al. 2004; Rui, 2011) are compared with GRACE TWS. GLDAS_NOAH θ and GRACE TWS are correlated with NHD in the concurrent month. The 3-month SPI characterizing precipitation deficits accumulated in the previous two months together with the hottest month itself (McKee et al. 1993) is applied, since soil moisture in the hottest month includes contributions from infiltration of precipitation in previous months. A 1°×1° spatial resolution is adopted for all datasets used in this study. Although the chosen resolution might be coarse for resolving detailed patterns of the θ-NHD relationship, it allows to investigate land surface and atmosphere coupling at synoptic scale, where water and heat exchanges between large air mass and land surface.

5.2.5 Correlation analysis

Relationships between NHD and soil moisture are examined by the Pearson linear correlation. The *t* test statistic is used to evaluate the statistical significance of the correlation coefficient (*r*). For testing the linear relationship between time-series grid datasets, erroneous rejection of null hypothesis inevitably happens at individual grid cells for several reasons, as described in Wilks (2016), leading to the false discovery of significant relationships. To address this problem, the threshold for significant p-values (typically 0.05) should be adjusted to control the False Discovery Rate (FDR). This adjustment is done based on the distribution of *p*-values of all grid cells and a prescribed parameter α_{FDR} which controls the level of the False Discovery Rate. An α_{FDR} of 0.1 (=$2\alpha_{global}$, where α_{global} =0.05) should be used for gridded atmospheric data, as it often has strong spatial correlation (Wilks, 2016). After this adjustment, the threshold values for testing significant linear relationships are 0.0241 for NHD-SPI, 0.0235 for NHD-GLDAS_NOAH θ, 0.0191 for NHD-TWS, and 0.0347 for TWS-evaporative fraction (EF).

5.2.6 Dominance analysis

Stepwise multiple linear regression (Draper and Smith, 1998; Clow, 2010) is used to determine the significant (5% significance level assessed by an F-test) predictor variable in explaining NHD temporal variability for each grid cell. Next, the dominance analysis approach (Azen and Budescu, 2003) is applied to compare the relative importance of those selected variables. The total variance among a set of predictors can be fully partitioned by dominance analysis even if the predictors are correlated (Vize et al. 2019). The collinearity among predictors is addressed by examining the unique variance accounted for by the predictor across all possible regression sub-models involving the predictor. Dominance analysis is completed through an exhaustive set of pairwise comparisons among the predictors. The comparisons can be examined by three types of dominance: complete dominance, conditional dominance, and general dominance (Nimon and Oswald, 2013). To be completely dominant, a predictor must account for a greater amount of outcome variance than another predictor for every sub-model comparison. The conditional dominance of different predictors is conditional on what sub-model level is being examined. We applied the general dominance in this study, which is determined by taking the average amount of variance accounted for by a predictor across all sub-models and comparing it to other predictors. General dominance weights can be calculated for each predictor in a set and represent the relative proportion of R^2 attributable to a predictor.

5.3 Results and Discussion

5.3.1 Global θ-NHD relationship based on decomposed TWS

Correlations between NHD versus SPI, GLDAS_NOAH θ, and TWS during 1985–2015 are compared in Figure 5.2 (a–c). Similar spatial patterns of global θ-NHD relationship are observed. Strong θ-NHD relationships occur in most of the Americas, Europe, Australia, South Africa, East Asia, and Southeast Asia, which cover almost all the areas with strong land-atmosphere coupling as identified in previous studies (e.g., Koster et al. 2006; Miralles et al. 2012; Schwingshackl et al. 2017; Donat et al. 2017, Chen et al. 2019). Significant negative correlations between NHD and SPI are observed for 25.5% of the land area, while NHD and GLDAS_NOAH θ are significantly correlated for 17.3% of the land area. This difference may be due to the fact that SPI, being used as a soil moisture proxy, reflects its influence on air temperature by soil-moisture dependent latent heat processes (evaporation and transpiration). In addition, it may reflect precipitation and air temperature coupling through weather systems (e.g., evaporation of rainwater draws heat out of the near surface air).

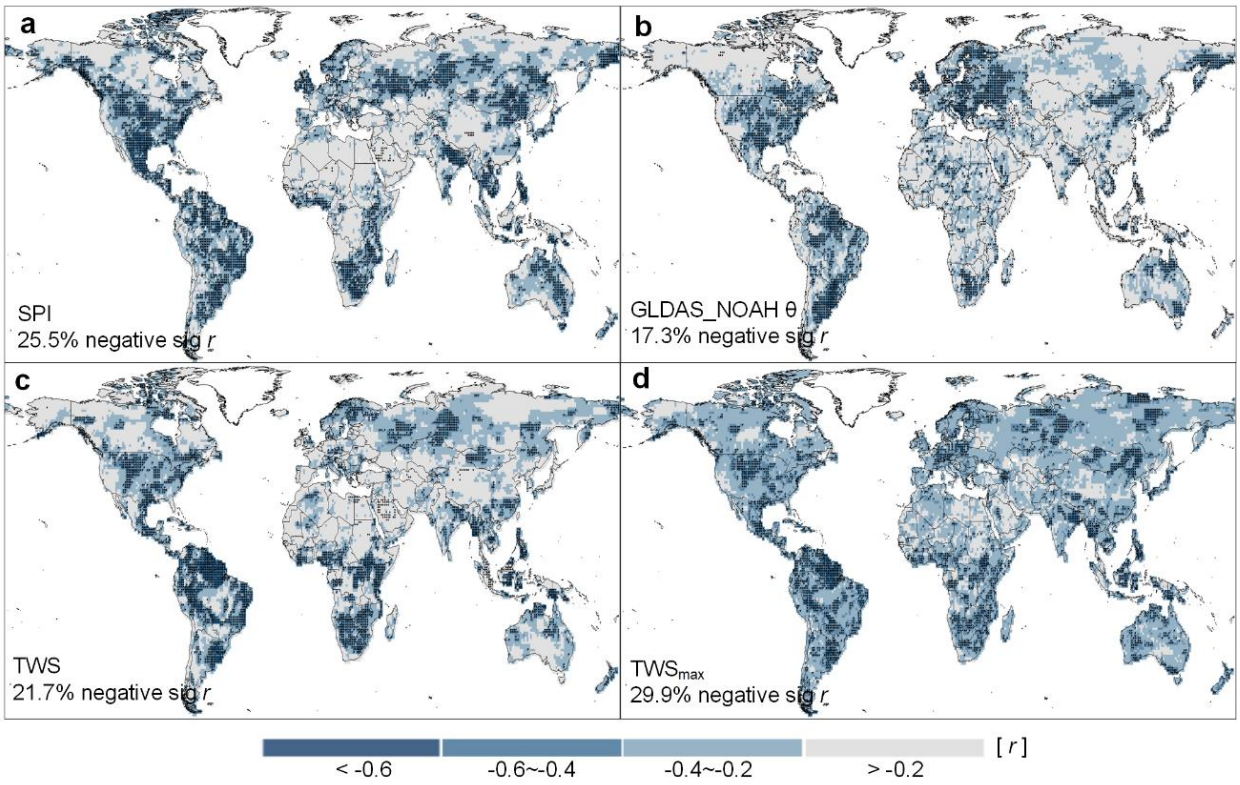

Figure 5.2 Correlations between NHD and (a) SPI; (b) GLDAS_NOAH θ; (c) raw TWS; and (d) the maximum r value of NHD versus any of the decomposed TWS components during 1985–2015 (based on reconstructed GRACE TWS data). Significant levels are denoted by black dots. No data is available for land area marked in white.

The total area of significant θ-NHD relationship increases, from 21.7% when the total terrestrial water storage is used, to 29.9% when the optimal decomposed TWS component at each grid cell is correlated to NHD (Figure 5.2 (c–d)). This is likely because that a part of the terrestrial water storage is not directly accessible for evapotranspiration. From all soil moisture proxies, the decomposed GRACE TWS covers the largest land area with significant negative correlation with NHD (Figure 5.2 (a–d)). It should be noted that only one TWS sub-component is used for Figure 5.2 (d) (which sub-component is used here can be seen in Figure 5.3). The sum of all decomposed TWS components is expected to have higher explanatory power for NHD temporal variability over a larger area.

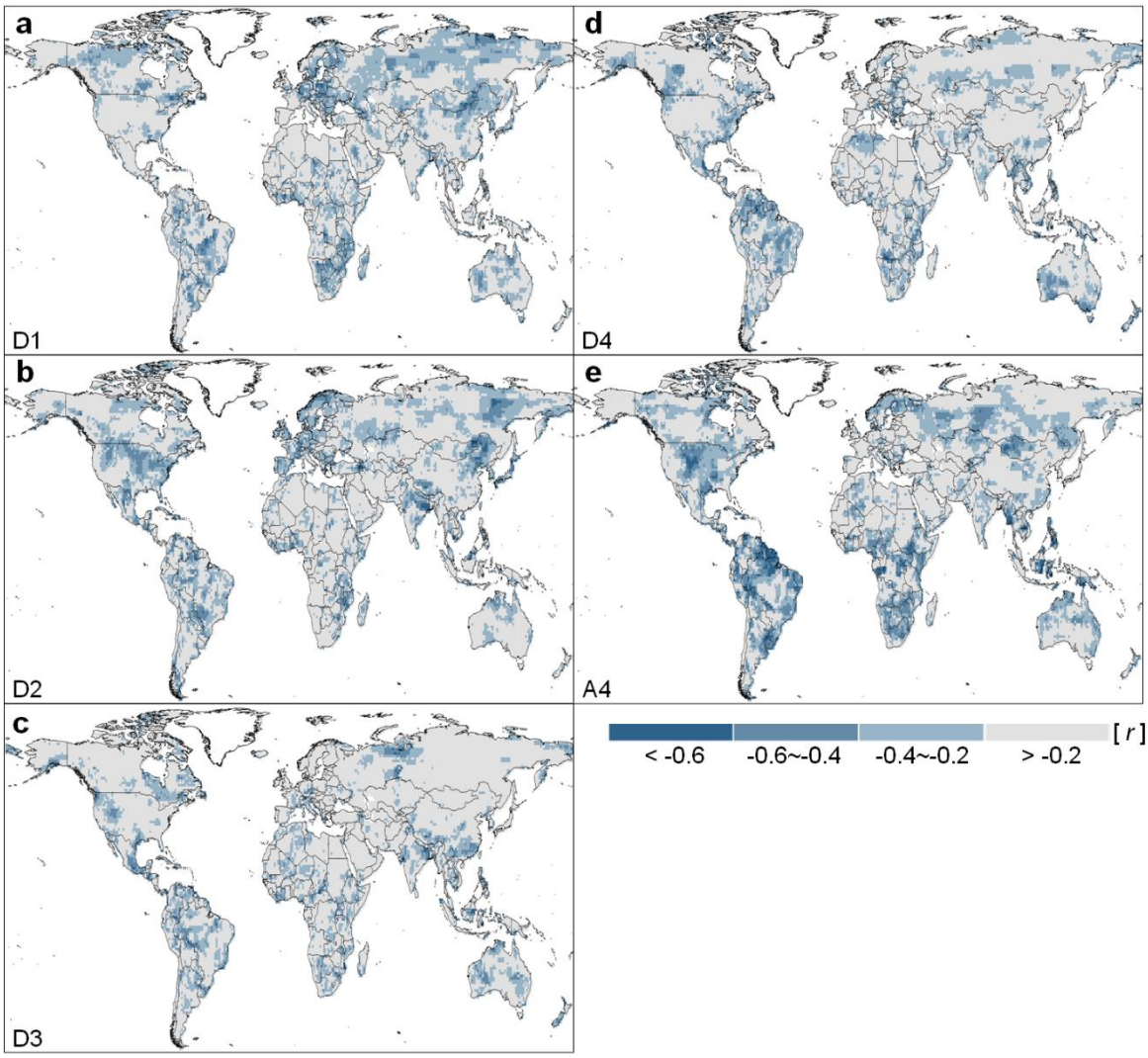

Figure 5.3 Correlation between NHD and wavelet decomposed TWS components (D1–D4, A4): (a) NHD-D1; (b) NHD-D2; (c) NHD-D3; (d) NHD-D4; (e) NHD-A4.

Results shown in Figure 5.2 are based on the reconstructed GRACE TWS dataset (1985–2015). We did the same analysis for the original GRACE TWS data from 2003 to 2016 for comparison, and the results are shown in Figure 5.4. Based on the 14-year data, strong θ-NHD relationships are also spatially distributed in most of the Americas, Europe, Australia, South Africa, East Asia, and Southeast Asia. In addition, the decomposed TWS (Figure 5.4 (d)) shows a significant correlation with NHD over a larger area than SPI (Figure 5.4 (a)) and GLDAS_NOAH θ (Figure 5.4 (b)). Although the period of available original GRACE TWS data is relatively short at present, its contribution to this and related research will increase with the accumulation of data and improved GRACE resolution in the future.

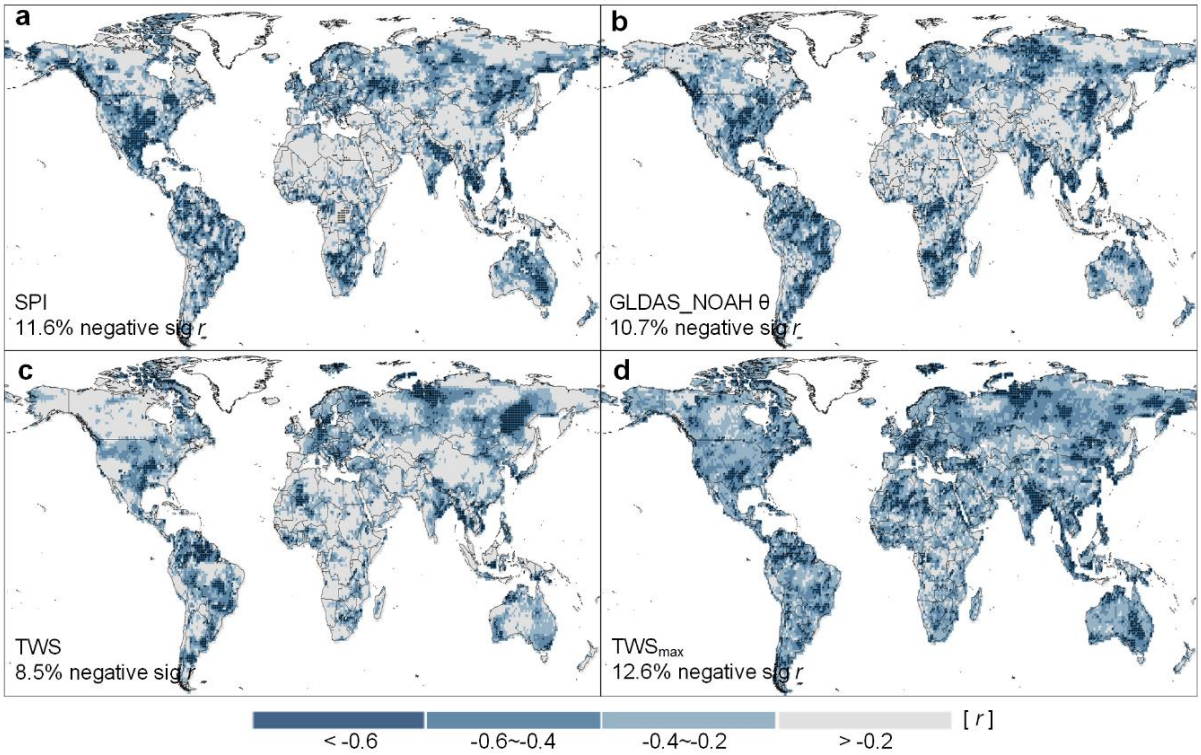

Figure 5.4 Correlations between NHD and (a) SPI; (b) GLDAS_NOAH θ; (c raw TWS; and (d) the maximum r value of NHD versus any of the decomposed TWS components during 2003–2016 (based on JPL GRACE TWS data). No data is available for land area marked in white.

A significant negative θ-NHD correlation can reflect a causal relationship between hot extremes and soil moisture deficit, either way. Since the θ-NHD relationship is examined in the hottest month, it is more likely to reflect the feedback of dry (primarily root-zone) soil to the atmosphere. On the one hand, high temperature is very likely to reduce transpiration in the hottest month due to stomatal responses to high vapour pressure deficit or temperature itself (Whitley et al. 2009; Wang et al. 2014; Wang et al. 2020). On the other hand, regions with strong negative θ-NHD correlation agree well with transitional climate regions (Koster et al. 2004; Seneviratne et al. 2010) where soil moisture strongly constrains evapotranspiration variability and thus results in feedbacks to the atmosphere. In addition, the correlation between TWS and the evaporative fraction (latent heat/net radiation) is relatively stronger in regions with significant negative θ-NHD correlation, such as parts of the Americas and Asia, South Africa, West Europe, and Australia (Figure 5.5). This implies that local moisture limitation in those regions results in a higher available energy partitioning towards sensible heat flux and consequently increases the occurrence of hot extremes. Indeed, it has already been suggested that hot extremes in Europe (Hirschi et al. 2011), Australia (Herold et al. 2016), and parts of the Americas and South Africa (Mueller and Seneviratne, 2012) are

amplified by moisture deficit. Furthermore, a similar spatial pattern of significant NHD-SPI correlation to those between NHD and other soil moisture indicators (Figure 5.2) supports that the observed negative NHD correlation reflects soil moisture deficit enhanced occurrence of hot extremes.

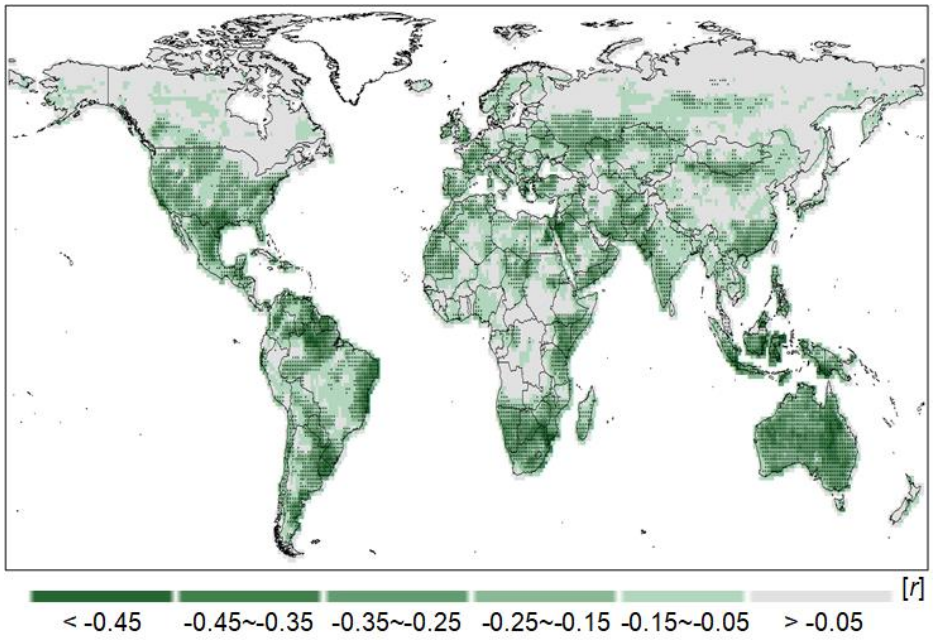

Figure 5.5 Correlation between TWS and the evaporative fraction (TWS-EF) during 1985–2015. Significant levels are denoted by black dots. No data is available for land area marked in white.

Figure 5.6 shows the explanatory power (reflected by the regression R^2) of different soil moisture proxies for NHD variability (1985–2015). The result is consistent with what is shown in Figure 5.2 that SPI has stronger explanatory power for NHD variability for a larger land area than GLDAS_NOAH θ. The decomposed TWS shows the highest R^2among all soil moisture proxies. For testing the improvement, the adjusted $R^2$is applied, which considers the total number of explanatory variables (up to 5 for the decomposed TWS vs. 1 for other proxies) by including a penalty for having additional variables in the regression analysis. The decomposed TWS shows a significant adjusted R^2 for 33.4% of the land area. For 72.0% of this area, the average adjusted R^2 increases to 0.24 compared to the raw TWS average adjusted R^2 (0.09). For 28.0% of this area, the raw TWS shows a slightly higher average adjusted R^2 (0.30) than that of the decomposed TWS (0.24). This result sheds light on the potential of decomposed GRACE TWS for hot extreme prediction.

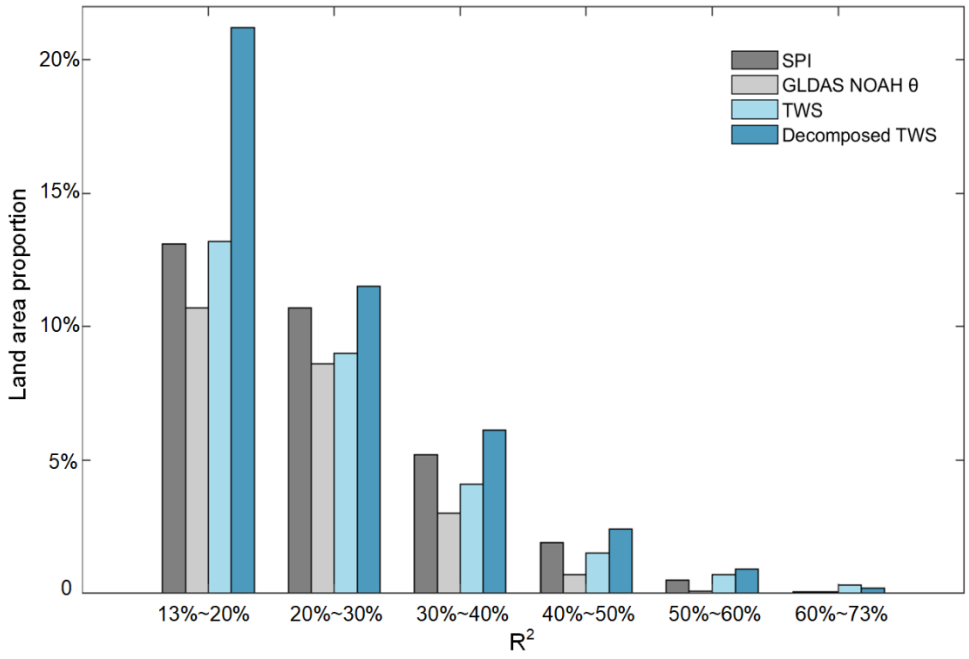

Figure 5.6 Histogram of the explanatory power (significant regression R^2) on NHD variability by using SPI, GLDAS_NOAH θ, raw TWS, and decomposed TWS during 1985–2015.

Areas having a significant negative correlation between NHD and decomposed TWS components during 1985-2015 are shown in Figure 5.7. Compared to D4+A4, D1–D3 shows a higher correlation with NHD in parts of Asia and Europe; those regions are reported to have relatively shallower plant rooting depth (Fan et al. 2017) where near-surface temperature has relatively shorter response time to soil moisture changes than that of regions with deeper plant rooting depth. The central part of North America, the northeastern part of South America and the northwestern part of Southeast Asia are reported to have deeper plant rooting depths (Fan et al. 2017), where interannual variability (D4 and A4) of TWS seems to be more important than its seasonal variability (D1–D3) in explaining NHD temporal variability. This implies that plant water uptake from deeper soil plays an essential role in θ-NHD coupling. However, D4+A4 also show a stronger correlation than D1+D2+D3 with NHD in areas without deep roots, including the northern and southeastern parts of South America and parts of Southeast Asia. This is because those regions have shallow groundwater table depth (Fan et al. 2013). It implies that in areas where groundwater is shallow, groundwater dependent ecosystems may contribute to heat mitigation, which is worthy of future investigation.

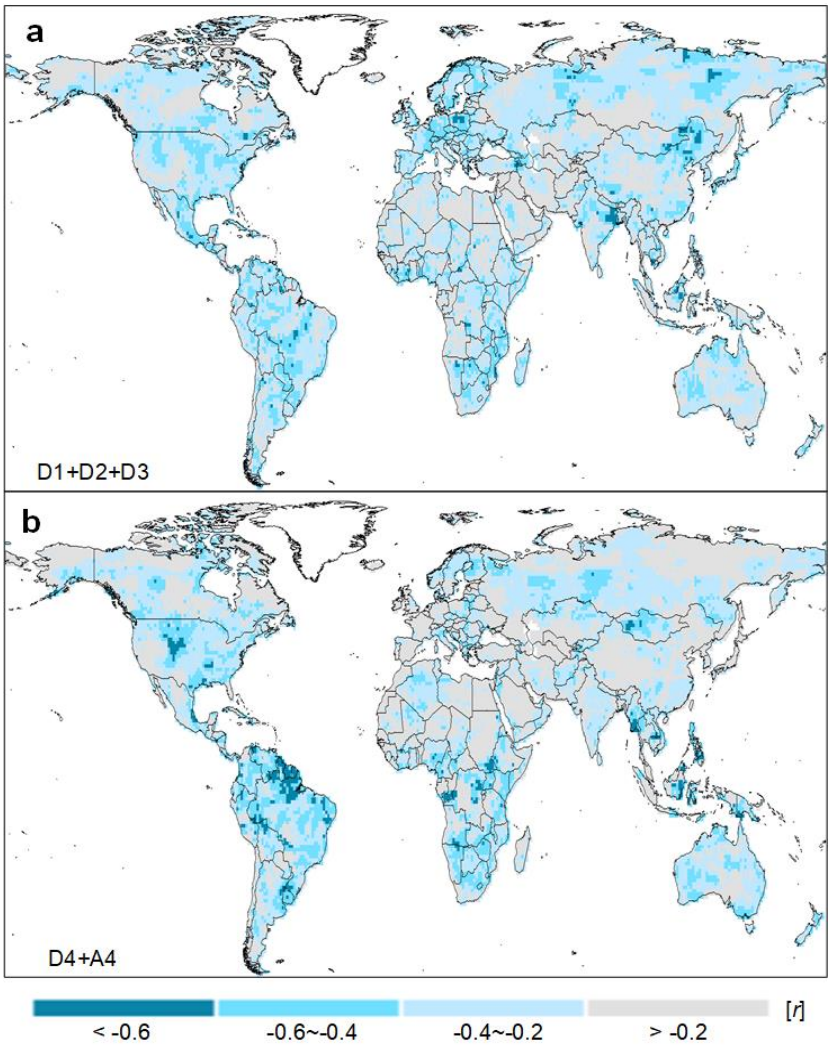

Figure 5.7 Correlation between NHD versus moisture at shallower soil depth (D1+D2+D3) (a) and deeper soil depth (D4+A4) (b) represented by wavelet decomposition levels of TWS (1985–2015).

5.3.2 Relative importance of global temperature change and local moisture deficit for hot extreme occurrence

The long-term underlying increasing trend in NHD seems to be a consequence of increasing global-mean temperature (Figure 5.8). Compared to the relationships between NHD versus different soil moisture proxies shown in Figure 5.2, significant correlations are observed in larger areas when the trends in NHD and soil moisture proxies have been removed (Figure 5.9). This implies that the trend and interannual variability in NHD might be respectively resulting from increasing global-mean temperature and natural variability in the climate system, i.e., interannual variability in soil moisture. Therefore, this study aims to reveal, which factor, global temperature change or local moisture deficit, is more important in influencing hot extreme occurrence during the study period 1985–2015. The decomposed TWS is adopted to represent soil moisture in the dominance analysis. The results are mapped in Figure 5.10, only the grid cells where the total explanatory power of global-mean

temperature and decomposed TWS is over 95% significance level are highlighted in colour. In areas with grey coloured grid cells, other factors than global temperature change or local moisture deficit, may have a stronger influence on hot extreme occurrence. These factors may include variables such as ocean-atmosphere dynamics (e.g., Lorenzo and Mantua, 2016) and land use changes (e.g., Luo and Lau, 2017).

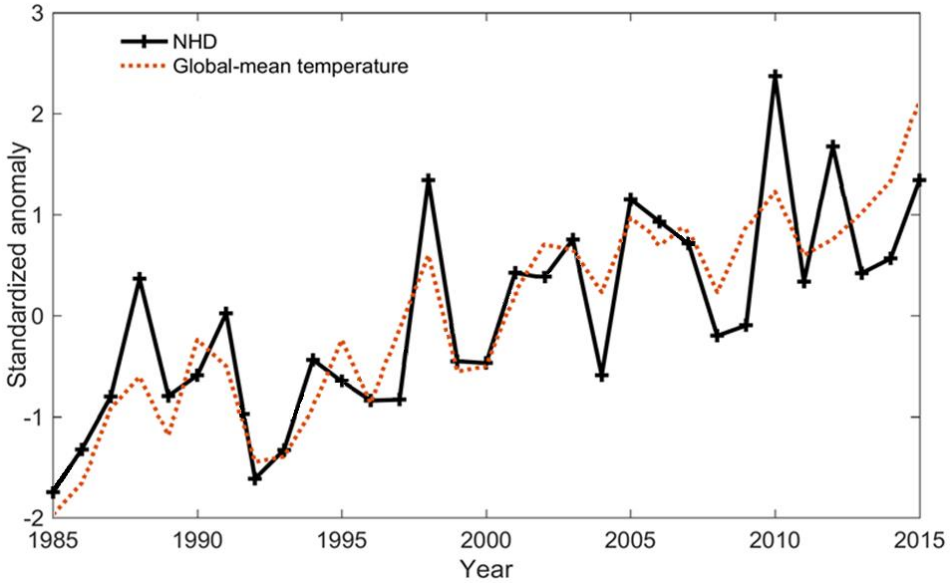

Figure 5.8 Standardized anomaly of global average NHD (land regions only) and global-mean temperature. The standardized anomalies are calculated with respect to the mean and standard deviation derived from the full period 1985–2015.

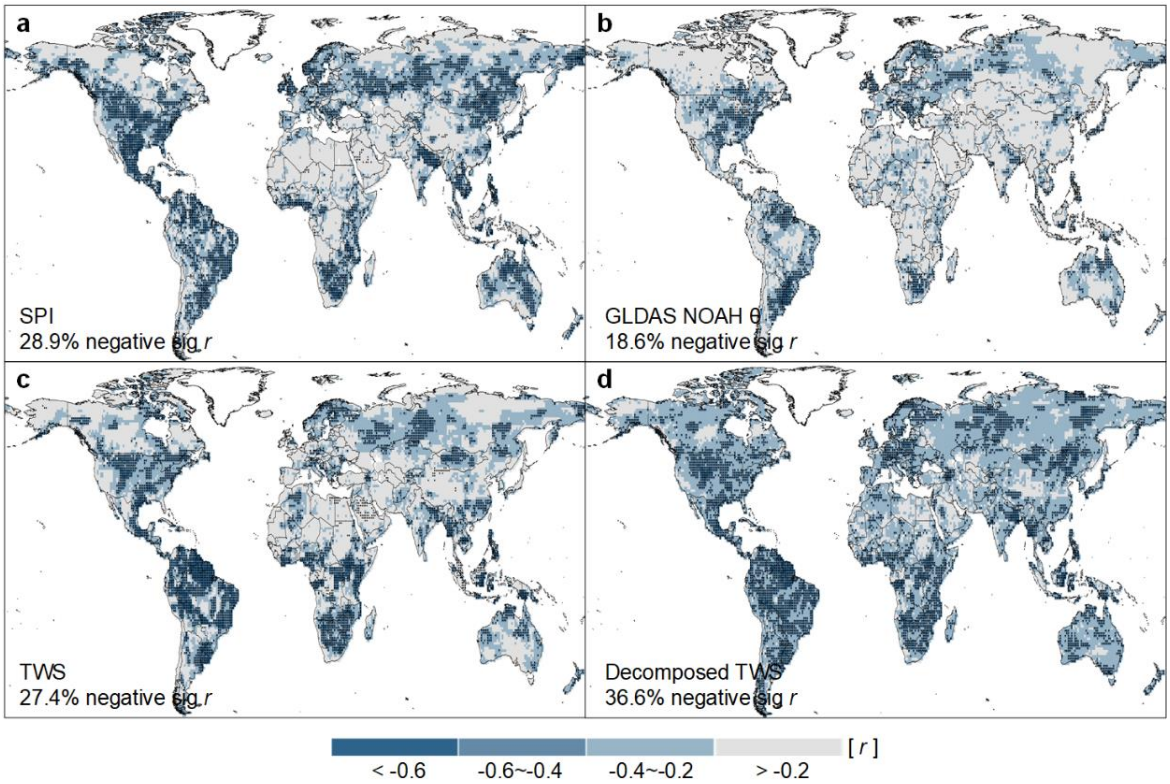

Figure 5.9 Correlations between detrended NHD and detrended soil moisture proxies: (a) SPI; (b) GLDAS_NOAH θ; (c) raw TWS; and (d) wavelet decomposed TWS (the maximum r value of detrended NHD versus any of the decomposed TWS components) during 1985–2015.

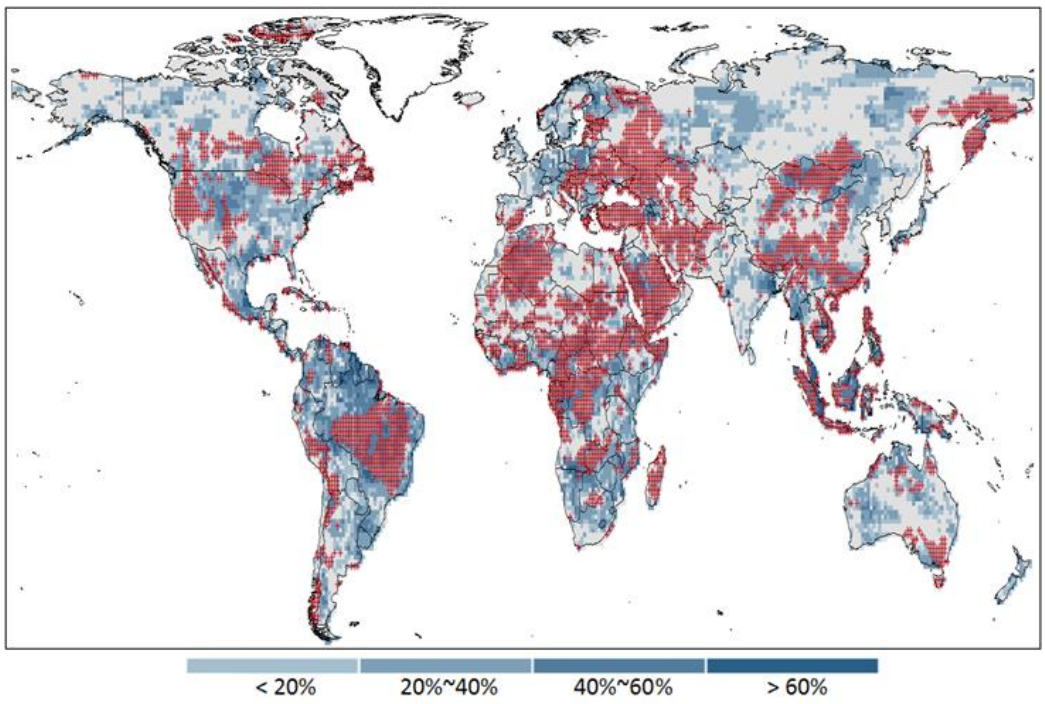

Figure 5.10 Spatial patterns of the total explanatory power of the joint influence of global-mean temperature and soil moisture on hot extreme occurrences. Global temperature change is more important in influencing the occurrence of hot extremes in areas marked by red cross symbols, while local moisture deficit is more important in areas with blue colours. Hot extreme occurrences in the grey areas are not significantly associated with either global-mean temperature or soil moisture during the study period 1985–2015.

During 1985–2015, for 23.8% of the land area with significant regression R^2, global temperature change plays a more important role than local moisture deficit in influencing the occurrence of hot extremes. Those areas are more likely located in extreme dry regions (e. g., the Sahara), mountain ranges (e. g., the Andes in South America), and plateaus (e. g., the Mongolian Plateau and the Tibet Plateau), where interannual variability of root zone moisture is likely small due to water deficiency, steep topography, and/or low temperature. In most previously identified regions with strong land moisture and air temperature coupling, including the northern areas of South America, the southern regions of North America, South Africa, West Europe, parts of East Asia and Australia, local moisture deficit shows very strong explanatory power for NHD temporal variability. It appears that local moisture deficit plays a more important role than global temperature change in influencing the hot extreme occurrences for 38.2% of the land area with significant regression R^2. Areas, where moisture deficit is more important than global temperature change the occurrence of hot extremes, tend to be flat with thick soils, such as the North American Great Plain,

the West Siberian plain and the North China Plain. Some areas where moisture deficit shows a more important role in hot extreme occurrences including India, Australia, South Africa, and the eastern tip of Brazil have one common characteristic: their interannual rainfall variability is high (Fatichi et al., 2012).

5.4 Conclusions

This study identifies which factor, global temperature change or local moisture deficit, is more important in influencing the temporal occurrence of hot extremes at a global scale during 1985–2015. In parts of the Americas, Africa, and Asia, the occurrence of hot extremes is more sensitive to global temperature change than in other areas. Most of those regions are mountain ranges (e.g., the Andes), plateaus (e.g., the Brazilian Plateau), and deserts (e.g., Sahara). Local moisture deficit plays a more important role in influencing hot extreme occurrences in regions with a total area 1.6 times as large as the area strongly influenced by the global temperature change during the 31-year period investigated here, which is an important new realisation. These regions, i.e., North America, West Europe, Australia, and South Africa are previously identified as having strong land-atmosphere coupling, influencing the moisture deficit-hot extreme links. Moisture deficit sensitive regions also share some common characteristics, such as relatively flat topographies, thick soils, and large inter-annual rainfall variabilities. In those regions, mitigation of some hot extremes might be possible by addressing the increasing moisture deficit, e.g., by adaptive land management. The noise from natural climate variability is an important factor in influencing the occurrence of NHD in larger areas than that of the signal from global-mean temperature within the 31-year period of the analysis. However, under a continuing increase of greenhouse gas forcing, increased temperature warming is expected to result in an increasing trend in the NHD. Furthermore, a continuous increase in global-mean temperature can also result in regional decreasing trends in soil moisture during the hottest month and consequently exerts indirect effects on NHD. Hence, global measures for reducing emissions are essential in combating the current and future expansion of hot extremes.

The dominance analysis approach is applied to quantify the relative importance of global temperature change and local moisture deficit to the occurrence of hot extremes during 1985–2015. For the first time, the application of decomposed GRACE TWS in estimating the global distribution of hot extremes is presented. It shows larger areas with significant θ-NHD relationships, and higher regression R^2 in examining the occurrence of hot extremes than the other commonly used soil

moisture proxies SPI, and a land surface model derived product. It suggests the potential of decomposed GRACE TWS as a useful soil moisture proxy in examining moisture-heatwave coupling.

5.5 References

Alexander, L. 2011. Extreme heat rooted in dry soils, Nature Geoscience. 4 (1), 12–13.

Andrew, R. A., Guan, H. and Batelaan O. 2017a. Estimation of GRACE water storage components by temporal decomposition, Journal of Hydrology. 552, 341–350.

Andrew, R. L., Guan, H., Batelaan, O. 2017b. Large-scale vegetation responses to terrestrial moisture storage changes. Hydrology and Earth System Science. 21, 4469–4478.

Azen, R. and Budescu, D. V. 2003. The dominance analysis approach for comparing predictors in multiple regression, Psychological Methods. 8 (2), 129–148.

Chen, A., Guan, H., Batelaan, O., Zhang, X. and He, X. 2019. Global soil moisture-air temperature coupling based on GRACE-derived terrestrial water storage, Journal of Geophysical Research-Atmospheres. 124.

Clow, D. W. 2010. Changes in the timing of snowmelt and streamflow in Colorado: a response to recent warming, Journal of Climate. 23 (9), 2293–2306.

Dee, D. P., Uppala, S. M., Simmons, A. J., Berrisford, P., Poli, P., Kobayashi, S., et al. 2011. The ERA-Interim reanalysis: Configuration and performance of the data assimilation system, Quarterly Journal of the Royal Meteorological Society. 137 (656), 553–597.

Donat, M. G., Pitman, A. J. and Seneviratne, S. I. 2017. Regional warming of hot extremes accelerated by surface energy fluxes, Geophysical Research Letter. 44, 7011–7019.

Draper, N. R. and Smith, H. 1998. Applied Regression Analysis, Wiley Interscience: Hoboken, N. J.

Fan, Y., Li, H. and Miguez-Macho, G. 2013. Global patterns of groundwater table depth, Science., 339, 940–943.

Fan, Y., Miguez-Macho, G., Jobbágy, E. G., Jackson, R. B. and Otero-Casal, C. 2017. Hydrologic regulation of plant rooting depth, Proceedings of the National Academy of Sciences. 114 (40), 10572–10577.

Fatichi, S., Ivanov, V. Y., Caporali, E. 2012. Investigating interannual variability of precipitation at the global scale: is there a connection with seasonality? Journal of Climate. 25, 55125523.

Hansen, J., Ruedy, R., Sato, M., Lo, K. 2010. Global surface temperature change, Review of Geophysics. 48, RG4004.

Herold, N., Kala, J. Alexander, L. V. 2016. The influence of soil moisture deficits on Australian heatwaves, Environmental Research Letters. 11, 064003.

Hirschi, M., Seneviratne, S. I., Alexandrov, V., Boberg, F., Boroneant, C., Christensen, O. B., et al. 2011. Observational evidence for soil-moisture impact on hot extremes in southeastern Europe, Nature Geoscience. 4 (1), 17–21.

Hirschi, M., Mueller, B., Dorigo, W., Seneviratne, S. I. 2014. Using remotely sensed soil moisture for land-atmosphere coupling diagnostics: the role of surface vs. root-zone soil moisture variability, Remote Sensing of Environment. 154, 246–252.

Humphrey, V., Gudmundsson, L., Seneviratne, S. I. 2017. A global reconstruction of climate-driven sub-decadal water storage variability, Geophysical Research Letter. 44.

IPCC, 2013. Stocker, T. F., Qin, D., Plattner, G. K., Tignor, M., Allen, S. K., Boschung, J., et al (Eds.), Summary for Policymakers. In: Climate Change 2013: The Physical Science Basis. Contribution of Working Group I to the Fifth Assessment Report of the Intergovernmental Panel on Climate Change Cambridge University Press, Cambridge, United Kingdom and New York, NY, USA.

IPCC, 2021. Masson-Delmotte, V., P. Zhai, A. Pirani, S. L. Connors, C. Péan, S. Berger, N. Caud, Y. Chen, L. Goldfarb, M. I. Gomis, M. Huang, K. Leitzell, E. Lonnoy, J.B.R. Matthews, T. K. Maycock, T. Waterfield, O. Yelekçi, R. Yu and B. Zhou (eds.). Summary for Policymakers. In: Climate Change 2021: The Physical Science Basis. Contribution of Working Group I to the Sixth Assessment Report of the Intergovernmental Panel on Climate Change Cambridge University Press. In Press.

Koster, R.D., Guo, Z.C., Dirmeyer, P. A., Bonan, G., Chan, E., Cox, P., et al. 2006. GLACE: The Global Land-Atmosphere Coupling Experiment. Part I: overview, Journal of Hydrometeorology. 7, 590–610.

Lorenz, R., Jaeger, E. B., Seneviratne, S. I. 2010. Persistence of heat waves and its link to soil moisture memory, Geophysical Research Letter. 37, L09703.

Lorenzo, D. E. and Mantua N. 2016. Multi-year persistence of the 2014/15 North Pacific marine heatwave, Nature Climate Change. 6, 1042–1047.

Luo, M. and Lau, N. C. 2017. Heat waves in southern China: Synoptic behaviour, long-term change, and urbanization effects, Journal of Climate. 30, 703–720.

McKee, T., Doesken, N., Kleist, J. 1993. The relationship of drought frequency and duration to time scales, 8th Conference on Applied Climatology, pp 179–184.

Miralles, D., van den Berg, M., Teuling, A., de Jeu, R. 2012. Soil moisture-temperature coupling: A multiscale observational analysis, Geophysical Research Letter. 39, L21707.

Mueller, B. and Seneviratne, S. I. 2012. Hot days induced by precipitation deficits at the global scale, Proceedings of the National Academy of Sciences. 109 (31), 12398–12403.

Nimon, K. F. and Oswald, F. L. 2013. Understanding the results of multiple linear regression beyond standardized regression coefficients, Organizational Research Methods. 16, 650–674.

Perkins, S. E., Argüeso, D., White, C. J. 2015.Relationships between climate variability, soil moisture, and Australian heatwaves, Journal of Geophysical Research-Atmospheres. 120, 8144–8164.

Perkins-Kirkpatrick, S. E. and Gibson, P. B. 2017. Changes in regional heatwave characteristics as a function of increasing global temperature. Scientific Report. 7, 12256.

Rodell, M., Houser, P.R., Jambor, U., Gottschalck, J., Mitchell, K., Meng, C., et al. 2004. The Global Land Data Assimilation System, B Bulletin of the American Meteorological Society. 85, 381–394.

Rui, H. 2011. Readme document for global land data assimilation system version 2 (GLDAS-2) products, Tech. rep. GES DISC.

Schneider, U., Becker, A., Finger, P., Meyer-Christoffer, A., Rudolf, B. and Ziese, M. 2015. GPCC Full Data Monthly Product Version 7.0 at 1.0°: Monthly Land-Surface Precipitation from Rain-Gauges built on GTS-based and Historic Data, doi: 10.5676/DWD_GPCC/FD_M_V7_100.

Schwingshackl, C., Hirschi, M., Seneviratne. S. I. 2017. Quantifying spatiotemporal variations of soil moisture control on surface energy balance and near-surface air temperature, Journal of Climate. 30 (18), 7105–7124.

Seneviratne, S. I., Corti, T., Davin, E. L., Hirschi, M., Jaeger, E. B., Lehner, I., Orlowsky, B., Teuling, A. J. 2010. Investigating soil moisture-climate interactions in a changing climate: A review, Earth Science Review. 99, 125–161.

Vize, C. E., Collison, K. L., Crowe, M. L., Campbell, W. K., Miller, J. D., Lynam, D. R. 2019. Using dominance analysis to decompose narcissism and its relation to aggression and externalizing outcomes, Assessment. 26, 260–270.

Vogel, M. M., Orth, R., Cheruy, F., Hagemann, S., Lorenz, R., van den Hurk, B. J. J. M., et al. 2017. Regional amplification of projected changes in extreme temperatures strongly controlled by soil moisture-temperature feedbacks, Geophysical Research Letter. 44, 1511–1519.

Wang, H., Guan, H., Deng, Z., Simmons, C. 2014. Optimization of canopy conductance models from concurrent measurements of sap flow and stem water potential on Drooping Sheoak in South Australia, Water Resources Research. 50 (7) pp. 6154–6167.

Wang, H., Guan, H., Liu, N., Soulsby, C., Tetzlaff, D., Zhang, X. 2020. Improving the Jarvis-type model with modified temperature and radiation functions for sap flow simulations, Journal of Hydrology. 587.

Watkins, M. M., Wiese, D. N., Yuan, D.-N., Boening, C. and Landerer, F. W. 2015. Improved methods for observing Earth's time variable mass distribution with GRACE, Journal of Geophysical Research-Solid Earth. 120, 2648–2671.

Whitley, R., Medlyn, B., Zeppel, M., Macinnis-Ng, C., Eamus, D. 2009. Comparing the Penman-Monteith equation and a modified JarvisStewart model with an artificial neural network to estimate stand-scale transpiration and canopy conductance, Journal of Hydrology. 373 (1–2), 256–266.

Wiese, D. N., Yuan, D.-N., Boening, C., Landerer, F. W., Watkins, M. M. 2019. JPL GRACE and GRACE-FO Mascon Ocean, Ice, and Hydrology Equivalent Water Height JPL Release 06 Version 02. Ver. 2. PO. DAAC, CA, USA.

Wilks, D.S. 2016. “The stippling shows statistically significant grid points”: how research results are routinely overstated and overinterpreted, and what to do about it, Bulletin of the American Meteorological Society. 2263–2273.

6 CONCLUSIONS AND FUTURE RESEARCH INTERESTS

6.1 Conclusions

The studies in this thesis aim to improve our understanding of land-atmosphere interactions at continental and global scales based on the application of GRACE TWS. The key findings of each chapter are as follows:

(1) Chapter 2 reported a new large-scale terrestrial water storage variation pattern in Australia: a seesaw wetting/drying pattern between the eastern and western Australia. This seesaw phenomenon is characterized by eastern Australia gaining water, while western Australia is losing water, and vice versa. The seesaw pattern is resulted from a combination of effects from large-scale climate modes (e.g., La Niña, IOD, IPO) and dynamic vegetation and soil moisture interactions. This study improved our understanding of the variation patterns of land surface conditions and their responses to climate variability. The newfound seesaw phenomenon could provide society with valuable reference for managing forest, water, and disaster risks in Australia.

(2) Chapter 3 reported that non-linear interaction between vegetation and terrestrial water condition was detected in more than half (58.4%) of the total area of Australia. Precipitation can indicate the water condition that vegetation relies on, but a comparison study suggested that GRACE TWS performed better than precipitation in examining the interactions between surface vegetation and land water conditions. The unidirectional and bidirectional causality relationships between vegetation (NDVI) and water (precipitation or TWS) were identified by using the non-linear Granger causality method. Although the Granger causality test does not confirm a direct physical mechanism between two variables, it provides implications of possible causality links from a statistical perspective. Temperature showing stronger Granger casual effects than water and energy on surface vegetation condition over 19.1% area of Australia was firstly reported here, implying the adverse effects of high temperature on vegetation's photosynthesis and growth rate. Results of Chapter 3 highlighted the feedback of vegetation on hydrological processes and implied the important role of vegetation in terrestrial water and carbon cycles and land-atmosphere interactions in the context of climate change.

(3) Chapter 4 suggested that wavelet decomposed GRACE TWS is applicable as a soil moisture proxy in examining soil moisture-air temperature coupling. Among the commonly used soil moisture proxies, precipitation performs better than GLDAS modelled soil moisture (0–1m) and

microwave remote sensing soil moisture (0–2 cm) in examining their relationships with air temperature. Combination of the decomposed TWS and precipitation further improved their explanation power for monthly air temperature variability particularly in places where vegetation tends to have a deeper rooting system. It is because that TWS can provide information of deeper soil moisture. Deeper rooting systems and clear wet and dry season alternation are favourable to the development of the soil moisture-air temperature coupling. This study improved our understanding of global soil moisture-air temperature coupling and suggested a useful soil moisture proxy, i.e., GRACE TWS, which could improve the representation of land-atmosphere interactions in Earth system models.

(4) Chapter 5 compared the relative importance of global temperature change and regional land-atmosphere coupling in influencing hot extremes. Results suggested that during the study period 1985–2015, local moisture deficit played a more important role in influencing hot extreme occurrences in regions with a total area 1.6 times as large as the area strongly influenced by the global mean temperature change. Here the local moisture deficit was represented by the wavelet decomposed GRACE TWS as it performed better than precipitation-related indices and soil moisture products derived from land surface model and microwave remote sensing technology in examining the relationship between soil moisture and the occurrences of hot extremes. Results of this study have significant implications for the development of adaptation strategies for increasing hot extremes. For example, mitigating hot extremes in areas with strong land-atmosphere coupling might be possible by improving adaptive land management, while areas that are sensitive to global temperature change are more likely to rely on global measures on reducing emissions.

Overall, the results of this PhD study improved the knowledge of land-atmosphere interactions at continental and global scales and suggested a useful soil moisture proxy, i.e., the wavelet decomposed GRACE TWS, that can also be applied in other relevant studies. Such knowledge might make contribution to reducing uncertainties in future-climate scenarios in the context of global climate change.

Since the satellite observation provided by GRACE are less than 20 years, reconstructed TWS data are applied in all the main chapters in this thesis as data of longer length can make the statistical analysis more convincing. The quality of reconstructed data is a main concern. However, as the GRACE mission continues, longer data sets will become available, and the corresponding

outcomes will be more precise. In addition, other ways for applying GRACE data in hydroclimatological studies are worthy of exploration.

6.2 Future research interests

Several suggestions for future work that expands on the research in this thesis are given below:

(1) Previous studies have already revealed some spatial coherent variation patterns of TWS in Australia (e.g., Xie et al., 2016; Xie et al., 2019), but investigations on how those patterns vary with time were limited by the scarcity of long-term TWS data. The constructed GRACE TWS data of 114-year length available recently (Humphrey and Gudmundsson, 2019) provided the opportunity to explore a predictable large-scale wetting/drying pattern in Australia. The analysis method in Chapter 2 and the reconstructed TWS data could be applied for other continents in the future, based on which new predictable large-scale wetting/drying patterns may be found in other regions of the world.

(2) Chapter 3 revisited the spatial patterns of water limitation on vegetation growth in comparison to temperature and radiation. The results confirmed that vegetation growth in Australia is still mostly water limited. But compared to the results for last century shown in previous studies (Nemani et al., 2003; McVicar et al., 2012), temperature- and radiation-dominant regions become larger in recent years. This possible trend may be related to the climate warming and the corresponding change of vegetation feedback, which is worthy of further investigation in the future.

(3) Previous study (Andrew et al., 2017) used the wavelet decomposition method to reveal the moisture dependence of vegetation at different temporal frequencies, Chapter 4 in this thesis investigated the coupling between air temperature and moisture at different soil depths, similar studies could be carried out with other water dependent variables, such as terrestrial carbon content, in the future.

(4) Results in Chapter 5 were based on data of 1985–2015, however, under a continuing increase of greenhouse gas forcing, the relative importance of global temperature change and local land-atmosphere coupling in influencing hot extremes might be very different. Therefore, further study based on model outputs of different Representative Concentration Pathway (RCP) in the future could provide more reference information for the society to take measures on climate change adaptation and mitigation.

6.3 References

Andrew, R., Guan, H., Batelaan, O. 2017. Large-scale vegetation responses to terrestrial moisture storage changes. Hydrology and Earth System Science., 21, 4469–4478.

Humphrey, V. and Gudmundsson, L. 2019. GRACE-REC: a reconstruction of climate-driven water storage changes over the last century. Earth System Science Data, 11(3), 1153–1170.

Nemani, R.R., Keeling, C.D., Hashimoto, H., Jolly, W.M., Piper, S.C., Tucker, C.J., Myneni, R.B., Running, S.W. 2003. Climate-driven increases in global terrestrial net primary production from 1982 to 1999. Science. 300, 1560–1563.

McVicar, T.R., Roderick, M.L., Donohue, R.J., Li, L.T., Van Niel, T.G., Thomas, A., Grieser, J., Jhajharia, D., Himri, Y., Mahowald, N.M., Mescherskaya, A.V., Kruger, A.C., Rehman, S., Dinpashoh, Y. 2012. Global review and synthesis of trends in observed terrestrial near-surface wind speeds: Implications for evaporation, Journal of Hydrology. 416–417, 182–205.

Xie, Z., Huete, A., Restrepo-Coupe, N., Ma, X., Devadas, R., Caprarelli, G. 2016. Spatial partitioning and temporal evolution of Australia's total water storage under extreme hydroclimatic impacts. Remote Sensing of Environment, 183, 43–52.

Xie, Z., Huete, A., Cleverly, J., Phinn, S., McDonald-Madden, E., Cao, Y., Qin, F. 2019. Multi-climate mode interactions drive hydrological and vegetation responses to hydroclimatic extremes in Australia. Remote Sensing of Environment, 231, 111270.

APPENDIX

A1 An initial analysis on the 2009 Black Saturday bushfire occurred in Victoria, Australia

According to the possible mechanism of the TWS seesaw pattern described in Chapter 2 that strong La Niña puts large amount of water into Australia and can lead to continent-wide wetting period. If a region has better than normal vegetation cover (positive NDVI anomaly), it has higher water capacity during the La Niña induced wetting periods but has larger water consumption over the subsequent relatively dry years. When fire events occur, this region is expected to have higher fire risk. Based on this knowledge, woody vegetation coverage immediately after big wet is expected to determine fire risk in the subsequent dry years.

Here the relationship between vegetation cover (leaf area index, LAI) and bushfire risk (Flammability index, provided by Australian National University) during a 6-year dry interval (2003–2008) before the 2009 Black Saturday fire occurred in Victoria, Australia is analysed. The study period is set during Jan 2003–Dec 2008 because a moderate La Niña event ended in 2001, and MODIS LAI data is available from July 2002, and the Black Saturday fires started on 7 February 2009. As shown in Figure A1. 1 the study area is mostly covered by forest. Maps of the linear trends of LAI and Flammability during 2003-2008 are compared in Figure A1. 2. LAI trend and Flammability trend has significant negative correlation (Figure A1. 3, r=-0.21, p<0.01). This result indicates that decreasing woody vegetation cover corresponds to increasing fire risk, which is in line with expectation. Next, it will be tested in future's study that whether a higher LAI immediately after a La Niña induced wetting corresponds to a higher flammability immediately before a major bushfire event. If yes, this study will contribute to developing proactive woody plant management at an optimal time window to reduce bushfire risks, for example, thinning of woody cover immediately following the wet year.

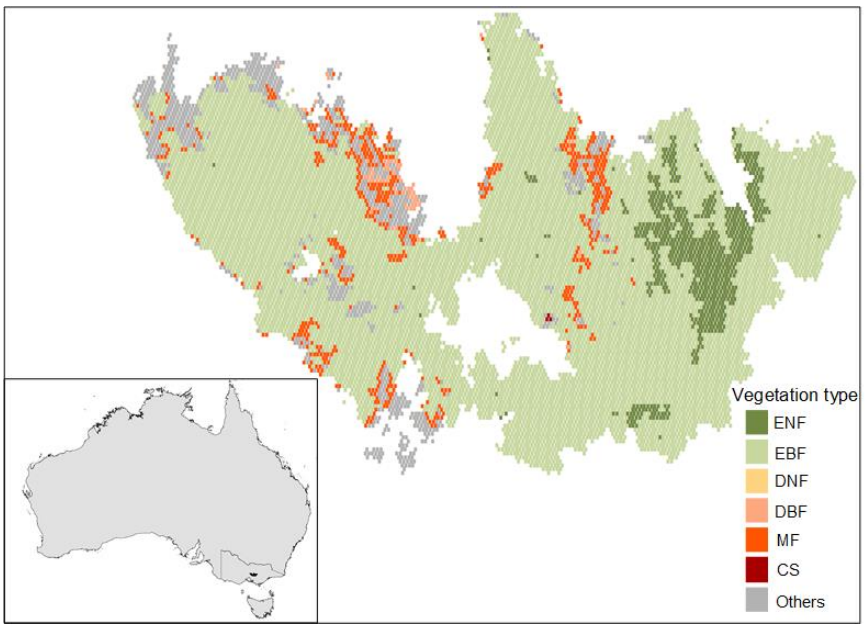

Figure A1.1 Vegetation types in the 2009 fire zone. (ENF: evergreen needleleaf forests; EBF: evergreen broadleaf forests; DNF: deciduous needleleaf forests; DBF: deciduous broadleaf forests; MF: mixed forests; CS: closed shrublands).

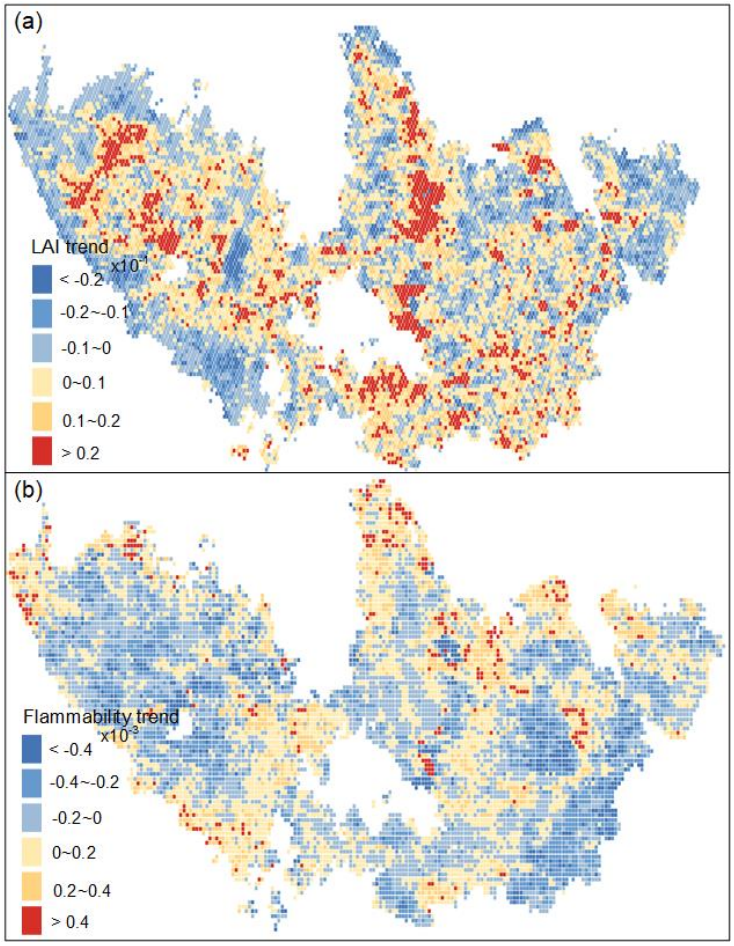

Figure A1.2 Linear trend of LAI (a) vs. Flammability (b) during Jan 2003–Dec 2008.

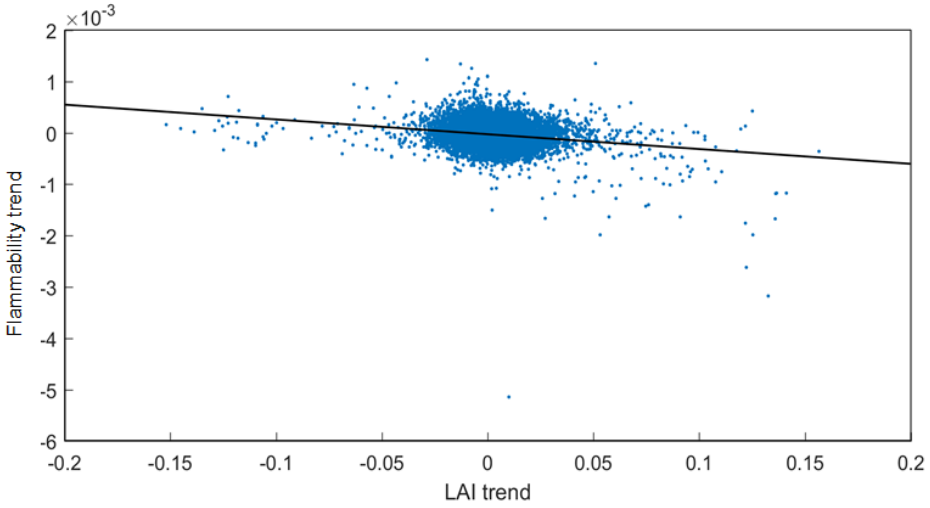

Figure A1.3 Scatter plot of linear trends of LAI and Flammability during Jan 2003–Dec 2008 (correlation coefficient r=-0.21, p<0.01).